ADVANCES IN ULTRA-HIGH FIELD 7 TESLA (T) HUMAN MRI: DESIGN AND METHODOLOGY OF TRANSMIT (TX) AND RECEIVE (RX) RADIO FREQUENCY (RF) COILS

by

Junghwan Kim

Bachelor of Science, Korea University, 2007

Submitted to the Graduate Faculty of

the Swanson School of Engineering in partial fulfillment

of the requirements for the degree of

Doctor of Philosophy

University of Pittsburgh

2018

UNIVERSITY OF PITTSBURGH

SWANSON SCHOOL OF ENGINEERING

This dissertation was presented

by

Junghwan Kim

It was defended on

July 13, 2018

and approved by

George D, Stetten, M.D, PhD, Professor

Department of Bioengineering

Kyungtae T, Bae, M.D, PhD, Professor

Department of Radiology

Patrick Loughlin, PhD, Professor

Department of Bioengineering

Dissertation Director: Tamer S, Ibrahim, PhD, Associate Professor

Department of Bioengineering

ADVANCES IN ULTRA-HIGH FIELD 7 TESLA (T) HUMAN MRI: DESIGN AND METHODOLOGY OF TRANSMIT (TX) AND RECEIVE (RX) RADIO FREQUENCY (RF) COILS

Junghwan Kim, PhD

University of Pittsburgh, 2018

Magnetic Resonance Imaging (MRI) is known as non-invasive imaging modality that provides superb anatomical soft tissue details. Over a decade, studies in ultrahigh field (UHF) MRI have been widely carried out in order to further improve the technology as well as understand the diseases. RF coil design and performance studies have been widely conducted to fully utilize the advantages that are given by UHF MRI. The aim of the design is typically producing uniform electromagnetic (EM) field distribution within the volume of interest while lowering the specific absorption rate (SAR) for Tx array and preserving/enhancing high signal to noise ratio (SNR) with Rx array.

Clinically available MRI such as 1.5 Tesla (T) and 3T, uses a whole body RF coil that is embedded in the scanner as the field exciter/transmitter, and separate receivers for different parts of the body. This body coil is not available in UHF MRI due to shorter wavelength resulting in inhomogeneous EM field distributions and the large size of the body coil challenges to tune and match the coil at resonant frequency of the UHF MRI, ~300MHz as well as the size of the UHF MRI market is too small that the vendors are not actively investing in the body coil development. Due to the inexistence of the body coil at UHF MRI, it is critical to develop a RF transmit coil systems that produce a uniform B_1^+ field (clockwise rotating circularly polarized transverse magnetic field that is responsible for excitation) and low specific absorption rate (SAR).

Aim of this thesis is to develop and evaluate new design of transmit (Tx) arrays and receive (Rx) arrays for breast and extremity (knee and ankle/foot) MR imaging at 7T. This thesis consists of several articles associated with breast and extremity MR imaging, namely:

1) Experimental and numerical analysis of B_1^+ field and SAR with a new transmit array design for 7T breast MRI *(published as a first author)*,

2) Development of a 7T RF coil system for breast imaging *(published as a first author)*,

3) Two way - split RF array development for knee MRI at 7T *(under preparation as a main author)*,

4) A new RF Transmit Coil for Foot and Ankle Imaging at 7T MRI *(published as a second author)*, and

Overall, the work of this thesis contributes toward the understanding RF coil design and evaluation for UHF MRI human imaging.

TABLE OF CONTENTS

LIST OF TABLES

LIST OF FIGURES

1.0 INTRODUCTION

1.1 ULTRAHIGH-FIELD MAGNETIC RESONANCE IMAGING (MRI): HISTORY AND APPLICATIONS

MRI is a powerful medical technology that provides superb soft tissue contrast, high spatial/temporal resolution, and signal-to-noise ratio (SNR)/contrast-to-noise ratio (CNR) [1-9]. It also enables tracing of morphological/physiological changes in the various parts of the body [1-9]. MRI is a relatively new medical imaging technology, with its history beginning in 1946 with two scientists, Felix Bloch, who proposed the Bloch equations, and Edward Mills Purcell, who discovered magnetic resonance in hydrogen (^{1}H) compounds [10-12]. They were awarded the Nobel Prize for physics in 1952 for their work in [12].

The first in-vivo MR imaging came along with the development of superconductors capable of producing high static magnetic fields [13]. In 1973-4, Paul Christian Lauterbur published an article showing the first cross-sectional image of an in-vivo mouse [14]. In the late 1970s, Peter Mansfield developed an imaging technique to significantly reduce scan time and still produce higher SNR when compared to existing techniques [15, 16]. They were both awarded a Nobel Prize for physiology or medicine in 2003 [17].

Since early 1980, research on superconducting magnets, RF coils, and imaging techniques has been widely conducted in order to produce higher field strength magnets. MRI at

high fields can potentially produce better signal detection, shortened scan time and increased SNR [8, 18-22]. 1.5T and 3T are Food and Drug Administration (FDA)-approved diagnostic tools and are currently widely used in hospitals and clinical facilities.

When the UHF human MRI was introduced in early 2000, it was not FDA approved for clinical purposes [2-4, 7, 8, 19, 23-41]; however, in 2017 Oct., the FDA finally cleared 7T human MRI for clinical use **(**https://www.fda.gov/NewsEvents/Newsroom/PressAnnouncements/ucm580154.htm).

The most significant advantages of the use of UHF human MRI are increased SNR and susceptibility induced contrast, which is very useful for imaging techniques that require high SNR and CNR, such as Functional MRI (fMRI), MR Spectroscopy (MRS), Blood Oxygenation Level Dependent (BOLD) MR imaging, high spatial anatomy MR imaging, 3-dimensional (3D) volume imaging, etc.

1.2 CHALLENGES OF ULTRAHIGH-FIELD MRI: TRANSMIT FIELD (B_1^+) INHOMOGENEITY AND SPECIFIC ABSORPTION RATE (SAR)

Along with the number of benefits at UHF MRI come several challenges, which are actively being studied by many scientists [1-3, 6, 8, 9, 18, 20, 22-26, 29-31, 34, 36, 39-62]. The challenges at UHF field strength (≥300 MHz (7T)) include: 1) an inhomogeneous transmitted (B_1^+) RF field within the region of interest (ROI), and 2) high RF power deposition or SAR in living tissue. Inhomogeneous B_1^+ field distribution and high RF power deposition are present due

to shorter in-tissue EM wavelength as the resonant frequency increases at UHF MRI. A B_1^+ field is circularly polarized EM field that is generated by the RF coil (details are explained in chapter 2.2).

These abovementioned challenges need to be closely investigated in order to provide for the safety of the subjects being imaged as well as the reliability of the imaging techniques for UHF human MRI. To alleviate the B_1^+ inhomogeneity issue at UHF MRI, an RF-shimming technique has been developed and is being widely studied for use for many different parts of the body [3, 54, 57, 63]. RF-shimming involves modulating the RF amplitude and phase at each of the excitation sources associated with the RF coil to provide homogenous B_1^+ field distribution [6, 23, 25, 31, 39, 40, 46, 47, 52, 56, 57, 61, 63-70].

B_1^+ inhomogeneities are pronounced when the size of the object being imaged becomes similar to or larger than the wavelength of the Lamor frequency of the MRI system, that is ~12-14 cm at 7T. Therefore, RF-shimming has been studied widely for use with the brain and torso. Breasts and extremities (knee, ankle, wrist, etc…) are relatively smaller electrically and have not been severely affected by the B_1^+ inhomogeneities issue; as a result, not many studies have incorporated RF-shimming in those regions [35, 37, 53, 57].

To accurately predict the RF power deposition in the living tissue and to prevent the potential of excessive heating in a localized area, finite-difference time-domain (FDTD) numerical modeling on human tissue models has been widely used [23, 46, 47, 52, 66, 71-76].

1.3 DISSERTATION OBJECTIVE

The main goal of this dissertation is to develop and implement new Tx and Rx RF array designs for UHF human MRI while minimizing the challenges identified in Section 1.2 and maximizing the advantages provided by higher magnetic field strength. Two different types of Tx RF array will be developed for this dissertation. These are:

1) Tic-Tac-Toe (TTT) array – BREAST AND ANKLE IMAGING

The loading insensitive TTT Design concept was first introduced by Ibrahim et. al. in early 2009, and prototypes have been built to investigate the magnetic field behavior and RF power deposition in living tissue [77]. In this work, we develop an eight channel and a four channel TTT TX RF array for breast and ankle imaging at 7T. Also, an eight-channel close fitting Rx-only array was developed for breast MR imaging at 7T. The developed Tx-only and Rx-only arrays are experimentally and numerically evaluated.

2) Transverse Electromagnetic (TEM) array – KNEE IMAGING

The TEM design is widely used for high field MRI. However, to the best of our knowledge, this design has been mostly used for Tx/Rx arrays. In this work, we develop a TX-only array using the TEM design and an eight channel RX-only array for knee MR imaging at

7T. We compare the SNR and CNR to those at 3T knee imaging. The magnetic field distribution for these arrays is also numerically calculated and compared to the in-vivo knee imaging. Evaluation details can be found in Section 1.4.

Through the successful development and evaluation of the RF array for breast/knee/ankle MR imaging at 7T, we expect to expand the technical boundaries for RF array design at UHF MRI. The proposed designs and implementations could be applied to various parts of the body. In addition, providing accurate prediction of the electromagnetic field behavior using our numerical models allows us to expand the understanding of RF behavior in the complex human body as well as RF safety for the subjects to be imaged.

1.4 DISSERTATION OUTLINE

The text below describes the chapter contents and outline the study.

Chapter 1 presents a general background of superconducting magnet history, the advantages and disadvantages at ultrahigh field MRI, and the dissertation objectives.

Chapter 2 reviews MR physics, RF coil technology, and the FDTD method to prepare for the discussion of our work.

Chapter 3 evaluates the developed Tx-only RF arrays for breast imaging at 7T. First, the process of the Tx array construction is described in detail. Second, the FDTD simulations of the

magnetic field distributions and SARs for the four different breast models are presented to demonstrate the robustness of the loading sensitivity and RF power absorption of the TTT design.

Chapter 4 evaluates the combination of Tx-only and Rx-only array for breast imaging at 7T. Circuit diagrams and detailed descriptions of the construction are presented. The noise matrix is measured for the developed Rx array and in-vivo breast MR imaging acquired at 7T and is compared to that acquired at 3T to demonstrate the SNR and CNR benefits at UHF MRI.

Chapter 5 and 6, Part1 and Part 2, evaluate the RF array developed for two extremities, knee and ankle, at 7T.

Chapter 5, Part 1 presents an evaluation of the TEM Tx-only array combined with an eight channel Rx-only array for knee imaging at 7T MRI. A computational knee model was created and used for B_1^+ map and SAR calculations. The calculated B_1^+ map was then compared to experimental measurements. The SNR, and CNR measured in the knee was compared to those acquired at 3T.

Chapter 6, Part 2 explores the RF array developed for ankle imaging at 7T MRI. The primary focus of this part of the chapter is to provide a description of the RF array construction and of a feasibility test of its use for ankle MR imaging. Experimental measurements of the scattering parameters and a B_1^+ map with the cylindrical phantom is demonstrated.

Chapter 7, as a conclusion, summarizes the findings/understanding and the significance of the work done in this dissertation. In addition, future work related to the dissertation is also discussed.

2.0 BACKGROUND

This chapter provides necessary background information on general MR physics, RF signal behavior, RF coil design and construction, and the methodologies discussed in subsequent chapters. Specifically, Section 2.1 reviews the nuclear spin system and its behavior under the presence of an external magnet field; Section 2.2 discusses RF excitation; Section 2.3 reviews important aspects of RF coils; and Section 2.4 gives a detailed overview of the finite difference modeling used in this dissertation. Finally, section 2.5 and 2.6 provide a brief summary the breast and extremity (knee and ankle) MR imaging, respectively.

2.1 PRINCIPAL PHYSICS OF MAGNETIC RESONANCE IMAGING

2.1.1 Spin Angular Momentum and Magnetic Field Interaction

Magnetic resonance is observed in nuclei with odd mass numbers, which possess spin angular momentum (**S**) and magnetic dipole momentum ($\boldsymbol{\mu}$). The relationship between these two quantities can be expressed as:

$$\boldsymbol{\mu} = \gamma \boldsymbol{S} \tag{2-1}$$

Where γ is the gyromagnetic ratio. In the absence of an external static magnetic field (B_0), magnetic diploe moment orientation is random, resulting in zero net magnetic dipole moment in the system; however, when B_0 is present, magnetic dipole moment ($\boldsymbol{\mu}$) experiences torque that is equal to the rate of change of spin angular momentum (**S**);

$$\frac{d\boldsymbol{S}}{dt} = \boldsymbol{\mu} \times \boldsymbol{B_0} \tag{2-2}$$

It is common to notate B_0 in the Z-direction, and the equation can be rewritten as:

$$\frac{d\boldsymbol{S}}{dt} = \boldsymbol{\mu} \times B_0\hat{z} \quad , \quad \boldsymbol{\mu} = \gamma \boldsymbol{S} \tag{2-3}$$

$$\frac{d\boldsymbol{\mu}}{dt} = \gamma(\boldsymbol{\mu} \times B_0\hat{z}) \tag{2-4}$$

Equation (2-4) can then be separated as below:

$$\frac{d\mu_x}{dt} = \gamma B_0 \mu_y \quad , \quad \frac{d\mu_y}{dt} = -\gamma B_0 \mu_x \quad , \quad \frac{d\mu_z}{dt} = 0 \tag{2-5}$$

With an initial condition of magnetic moment at t = 0:

$$\boldsymbol{\mu_0} = (\mu_{x0} + \mu_{y0} + \mu_{z0}) \cdot (\hat{x} + \hat{y} + \hat{z}) \tag{2-6}$$

Solving the differential equation using eq. (2-5) and (2-6) gives:

$$\boldsymbol{\mu} = \big(\mu_{x0}\cos(\omega t) + \mu_{y0}\sin(\omega t)\big)\hat{x} + \big(\mu_{y0}\cos(\omega t) - \mu_{x0}\sin(\omega t)\big)\hat{y} + \mu_{z0}\hat{z} \tag{2-7}$$

Mathematical expression describes the axis of rotation of the magnetic diploe moment, μ, aligning with the direction of external static magnetic field, B_0, in the Z-direction. In nature, nuclei with an odd mass number have a different energy level governed by quantum physics. For

example, an ^{1}H nucleus has a spin state number, n, of ½ that of the observable spin state level is 2 which can be calculated using the equation below:

$$\#\text{ of observable spin state level} = 2n + 1$$

These spin states equal the quantized energy level, and they are commonly referred to as "spin-up" and "spin-down" states. A spin-up state is at a lower-energy level and the direction of magnetic moment is pointing up, the same direction as B_0, and the spin-down state is at a higher-energy level, pointing opposite to B_0. Net magnetic moment (Magnetization (M)), total spin under the presence of B_0, is determined by the difference of these aligned spins (low-energy nuclei are always greater than high-energy nuclei, $M = \sum \mu = \mu_{low-energy} - \mu_{high-energy}$). Among the many odd number integer nuclei, ^{1}H is widely used in MR imaging due to its abundance in living tissue; ^{23}Na is also actively used in MRI studies since it is second-most abundant in living tissue.

2.1.2 Magnetization and the Bloch Equation

Magnetization (M) is the sum of the magnetic moment that contributes to MR signal generation, $M = \sum \mu$, and the behavior of the magnetization can be described in the same fashion as eq. (2-2).

$$\frac{dM}{dt} = \gamma(M \times B_0\hat{z}) \tag{2-8}$$

Where M_x, M_y, and M_z can be expressed as:

$$\frac{dM_x}{dt} = \gamma B_0 M_y \quad , \quad \frac{dM_y}{dt} = -\gamma B_0 M_x \quad , \quad \frac{dM_z}{dt} = 0 \tag{2-9}$$

To simplify the derivation, let's assume that the equation for magnetization at t = 0 is:

$$\boldsymbol{M_0} = M_{x0}\hat{x} + M_{z0}\hat{z} \tag{2-10}$$

Solving a differential equation using eq. (2-9) and (2-10) gives:

$$\boldsymbol{M} = M_{x0}\left(\cos(\omega t)\hat{x} - \sin(\omega t)\hat{y}\right) + M_{z0}\hat{z} \tag{2-11}$$

Where the angular frequency (the Larmor frequency) of precession of magnetization and the direction of the rotation is clockwise:

$$\omega_{Larmor} = -\gamma B_0 \tag{2-12}$$

In the presence of B_0, Magnetization (M) revolves at a unique angular frequency depending on strength of the B_0 and the gyromagnetic ratio for the nuclei that are being imaged. Due to the quantized energy level observed in the system, the Plank-Einstein relation can explain the atomic level energy transfer associated with wave frequency, f:

$$E = hf \ or \ \hbar\omega, \text{ where } \hbar = h/2\pi \tag{2-13}$$

Where the energy carried by the wave or the field can be transferred to the magnetization only if the frequency of the wave is the same as the natural frequency of the spin, $\gamma B_0/2\pi$. This

condition is called resonance. For example, the ^{1}H gyromagnetic ratio divided by 2π is 42.58 MHz Resonant frequency (MHz) can be calculated based on the equation below:

$$f_{resonance} = \frac{\gamma}{2\pi} B_0 \tag{2-14}$$

At 7T MRI, the resonant frequency of the ^{1}H is 297MHz. When an additional time varying magnetic field, B(t), is applied while B_0 is present, magnetization behaves in a fashion that can be illustrated by the Bloch equation. The Bloch equation is a macroscopic equation that describes the motion of nuclear magnetization as a function of time, incorporating the intrinsic time constants T1 and T2 of the nuclei. The Bloch eq. in the X, Y, Z-direction reads:

$$\frac{\partial M_x(t)}{\partial t} = \gamma\big(\boldsymbol{M}(t)\times\boldsymbol{B}(t)\big)\hat{x} - \frac{M_x(t)}{T2} \tag{2-15}$$

$$\frac{\partial M_y(t)}{\partial t} = \gamma\big(\boldsymbol{M}(t)\times\boldsymbol{B}(t)\big)\hat{y} - \frac{M_y(t)}{T2} \tag{2-16}$$

$$\frac{\partial M_z(t)}{\partial t} = \gamma\big(\boldsymbol{M}(t)\times\boldsymbol{B}(t)\big)\hat{z} - \frac{M_z(t)-M_0}{T1} \tag{2-17}$$

Where $M_{x,y,z}(t)$ are time dependent magnetizations and B(t) is the magnetic field composed of three different magnetic fields: B_0, B_1 and a Gradient field (**G**). T1 is called the spin-lattice relaxation time for the given nuclei and T2 is called the spin-spin relaxation time. $\hat{x}$, $\hat{y}$, and $\hat{z}$ are directional unit vectors in the X, Y, Z-directions in Cartesian coordinates. M_0 is the magnitude of magnetization under the presence of B_0 only. In vector notation, the Bloch equation reads:

$$\frac{\partial \boldsymbol{M}}{\partial t} = \gamma(\boldsymbol{M}\times\boldsymbol{B}) - \frac{M_x\hat{x}+M_y\hat{y}}{T1} - \frac{(M_z-M_0)\hat{z}}{T1} \quad (2\text{-}18)$$

2.2 RF EXCITATION CONCEPTS

In an MRI system, an externally applied EM field using an RF antenna is generated by an RF pulse because the operating frequency is in the range of radiofrequency. The behavior of the magnetization and applied RF pulse is governed by the Bloch equation. An applied RF pulse in the XY plane (transverse direction) can be expressed as a linear EM wave with amplitude of I_0 [A], phase (φ) and Larmor frequency (ω):

$$\boldsymbol{B_1}(t) = A_{0x} I_0 \cos(\omega t + \varphi)\hat{x} \quad (2\text{-}19)$$

Where A_{0x} is a position- and frequency- dependent attenuation factor. This RF pulse can be expressed mathematically with two circularly polarized (CP) fields:

$$\boldsymbol{B_1}(t) = \frac{A_{0x}I_0}{2}(cos(\omega t+\varphi)\hat{x} - sin(\omega t+\varphi)\hat{y}) + \frac{A_{0x}I_0}{2}(cos(\omega t+\varphi)\hat{x} + sin(\omega t+\varphi)\hat{y}) \quad (2\text{-}20)$$

In complex notation, the above equation can be expressed as:

$$\boldsymbol{B_1}(t) = \frac{A_{0x}I_0}{2} e^{-i(\omega t+\varphi)} + \frac{A_{0x}I_0}{2} e^{i(\omega t+\varphi)} \quad (2\text{-}21)$$

Where the first term on the right-hand side is 1), clockwise rotating, and the second term is 2), counter-clockwise rotating; 1) is called the transmit field (B_1^+), and 2) is called the receive field (B_1^-). Many studies have shown that B_1^- has a negligible effect on net magnetization; thus,

an applied linearly polarized RF pulse can be now considered as clockwise rotating field having half of the initial amplitude. Eq. (2-20) can be simplified to better illustrate the field component in complex notation such that:

$$\boldsymbol{B_1(t)} = \frac{B_{1x} + iB_{1y}}{\sqrt{2}} + \frac{B_{1x} - iB_{1y}}{\sqrt{2}} \tag{2-22}$$

Where $B_{1x} = \frac{A_{0x} I_0}{2} (cos(-\omega t + \varphi)\hat{\boldsymbol{x}})$ and $B_{1y} = \frac{A_{0x} I_0}{2} (cos(-\omega t + \varphi)\hat{\boldsymbol{x}})$ and the clockwise rotating transmit field can be represented as:

$$B_1^+ = \frac{B_{1x} + iB_{1y}}{\sqrt{2}} \tag{2-23}$$

And the receive field as:

$$B_1^- = \frac{B_{1x} - iB_{1y}}{\sqrt{2}} \tag{2-24}$$

During the RF transmission, magnetization that is initially aligned in the Z-direction, M_0, is tipped toward the XY-plane by the RF field, resulting in an M_0 decrease, and the motion of the magnetization can be explained by Bloch equation. During the reception, the RF field is no longer applied and tipped magnetization reverts to its initial condition, M_0; during this process, voltage is induced in an RF coil according to Faraday's law.

2.3 RF COILS

The RF coil is the antenna that is transmitting/receiving the RF field at the Larmor frequency of the nuclei of interest in the MRI system [78, 79]. It is often also referred to as an RF probe or RF resonator. RF coils take various names according to their function and their shape. An RF coil that is responsible for generating the RF field to excite the nuclei is called a transmit coil, or Tx, while an RF coil that is responsible for detecting the emitted RF signal is called a receive coil, or Rx. Also, if a coil is responsible for both the transmission and reception, it is called a transceiver coil, or T/Rx [6, 21, 22, 34, 44, 70, 73, 74, 79-85]. With regards to shape, an RF coil that surrounds the volume of interest and generates or receives an RF field within the entire volume is called a volume coil whereas an RF coil that is usually composed of a single-loop or multi-loop coil to generate RF fields that are more localized than a volume coil is called a surface coil [45, 86-91].

RF coils are important resonator modules that determine the quality of the MR image, including SNR and B1 homogeneity. A homogeneous B_1^+ field is usually achieved with a volume transmit coil and a high SNR is achieved through multiple arrays of surface coils located near the region of the interest [78, 79]. There are many types of RF coils on the market; however, RF coil are generally designed and built in labs for conducting UHF MRI. Since early 2000, when UHF human MRI was introduced, many research sites have designed and developed RF coils for specific research purposes [3, 18, 21, 24, 39, 40, 52, 60, 63, 84, 87, 91]. For UHF MRI

studies, RF coils are typically designed as a Tx-only array combined with an Rx-only array. It is designed in a such way that the Tx-only array can be used to manipulate the RF pulse to produce a homogeneous B_1^+ field; meanwhile the Rx-only array can be used to maximize the SNR [3, 18, 24, 39, 63, 78, 79, 92, 93]. As stated earlier in this chapter, the RF coil must generate the RF field with the same angular frequency as the nuclei precession, that is, the at Larmor frequency of the nuclei. As an example of laboratories that are actively conducting RF researches, Vaughan et al. have published many articles on UHF MRI RF coil research, especially using transverse electromagnetic (TEM) RF coil [22, 40, 79, 83, 89, 94-96]. Wald et al. have studied and published articles for UHF MRI RF coil design, mainly related to brain MR applications utilizing Rx-only array [97-100].

To understand the resonance in an electrical circuit, we consider a simple RLC model with current, $= I_0 e^{i\omega t}$. Kirchhoff's circuit law explains the total voltage in the circuit is equal to the sum of the voltage across the R, L, and C:

$$V = IR + L\frac{dI}{dt} + \frac{q}{C} \tag{2-25}$$

Where R is resistance (Ohms), L is inductance (Henry), and C is capacitance (Farad), q is total charge that:

$$V_R = I_0 e^{i\omega t} R \ , \ V_L = L\frac{d}{dt}\left(I_0 e^{i\omega t}\right) \ , \ V_C = \frac{1}{C}\int (I_0 e^{i\omega t})dt \tag{2-26}$$

Equation (2-25) now reads;

$$V = IR + i\omega LI - \frac{iI}{\omega C} \ , \ I = I_0 e^{i\omega t} \tag{2-27}$$

$$V = I[R + i\left(\omega L - \frac{1}{\omega C}\right)] \tag{2-28}$$

Where ω is the angular frequency, $i = \sqrt{-1}$, and maximum current I is achieved when the imaginary term is zero such that:

$$\omega = 1/\sqrt{LC} \tag{2-29}$$

This condition is called resonant frequency of the circuit, and the RF coil needs to match it to the Larmor frequency of the nuclei, that is, $\frac{1}{\sqrt{LC}} = \gamma B_0$. It is important to note that, since the magnetic field produced by the RF coil is directly proportional to the magnitude of the applied current, an RF coil that operates at $\omega = 1/\sqrt{LC}$ will produce a maximum magnetic field with a given input voltage. L and C are dependent on the number of copper wires and capacitors used in the RF coil and the resonant frequency of the coil can be measured using a network analyzer. For UHF-MRI at strengths like 7T, challenges arise because the coil's dimensions must be kept similar to those used in 3T because the size of the object or subject does not change, which implies that the inductance of the coil should remain similar. However, resonant frequency at 7T, 300Mhz, is more than x2 times higher than the 125Mhz at 3T. This means that the capacitance in the RLC circuit must be lowered to increase the resonant frequency. On the other hand, if the coil is constructed to be smaller, total inductance is low and requires a higher capacitance, which is limited by coil space.

2.3.1 RF Coil Development in an Ultrahigh-Field MRI System

In the 1990's, the majority of the MRI scanners used at the clinical sites were 1.5T. The past decade has seen a rapid deployment of 3T systems in the clinical sites and 4T/ 7T systems in the academic research institutions. Birdcage RF coils are widely used in the 1.5T and 3T MRI systems because they provide homogeneous MR images within the volume of interest with acceptable SNR [101-105]. For ultrahigh field MRI systems, such as 7T MRI, due to the small market size and the challenges with B_1^+ inhomogeneity and SAR, it is very difficult to purchase an RF coil. These challenges have motivated many research sites to develop an RF coil that can be customized to meet research needs [3, 19, 21, 24, 35, 38-40, 51, 52, 60, 66, 68, 76, 84, 87, 91, 99, 100].

When the size of the object that is being imaged is shorter than the wavelength of the RF pulse that is used for RF excitation (~13.5cm for ^{1}H at 7T MRI), the RF coil is typically designed as a volume Tx-only coil combined with an Rx-only array. For example, knee, ankle and wrist MR imaging typically use a birdcage or TEM volume Tx-only coil combined with a 4-8 channel Rx-only array coil because 1) from the RF transmission point of view, the B_1^+ inhomogeneity is less pronounced in a small object than it is in a larger object (such as torso or brain) and, 2) from the RF reception point of view, a multiple surface Rx array can maximize the SNR which can be used to increase the spatial resolution to image the microscopic structures [1, 3, 4, 19, 36-38, 45, 54, 63, 80, 106, 107]. A T/Rx coil can also be used for extremity MR imaging [60, 80, 83, 85, 98, 108-110]. For torso, abdominal, pelvis, and brain MR imaging, where the object is larger than the wavelength of the RF, the RF coil is generally designed as a T/Rx array because the RF

shimming technique is required to produce homogeneous B_1^+ distribution in the ROI, and a high SNR is needed to increase the spatial resolution [23, 38-40, 52, 57, 61, 67, 99, 105, 109, 111].

2.4 FINITE DIFFERENCE TIME DOMAIN (FDTD) METHOD IN MRI APPLICATION

The concept of FDTD, known as Yee's algorithm, was suggested in 1966 by Kane Yee [72]. This method is used to calculate and predict EM wave behavior – material interaction in the time and space domain using time-dependent Maxwell's equation in differential form. In the computational domain, the magnetic field and electric field from Maxwell's eq. are discretized and expressed in second-order central-difference approximation and each of the field vectors are solved. In MRI research, the FDTD method has been widely used to predict the EM wave behavior (produced by the RF coil) for waves that interact with complex biological living tissue, such as that in the human body [23, 39, 46, 51, 61, 66, 72, 76, 112].

Maxwell's equation in differential form can be written as below:

$$\nabla \times \bar{E} = -\frac{\partial \bar{B}}{\partial t} - \bar{M} \ (Maxwell - \ Faraday \ equation) \tag{2-30}$$

$$\nabla \times \bar{H} = \frac{\partial \bar{D}}{\partial t} + \bar{J} \ (Ampere - Maxwell \ circuital \ law) \tag{2-31}$$

$$\nabla \bullet \bar{D} = \rho_e \ (Gauss's \ law) \tag{2-32}$$

$$\nabla \bullet \bar{B} = \rho_m \ (Gauss's \ law \ of \ magnetism) \tag{2-33}$$

Where

$\bar{E} \rightarrow Electric \ field \ [volt/meter]$

$$\bar{B} = \mu\bar{H} \rightarrow Magnetic\ flux\ density\ [weber/meter^2] \quad (2\text{-}34)$$

$$\bar{M} = \bar{M}_{source} + \sigma_{loss}\bar{H} \rightarrow Equivalent\ magnetic\ current\ density\ [volt/meter^2] \quad (2\text{-}35)$$

$$\bar{H} \rightarrow Magnetic\ field\ [ampere/meter]$$

$$\bar{D} = \varepsilon\bar{E} \rightarrow Electric\ flux\ density\ [coulomb/meter^2] \quad (2\text{-}36)$$

$$\bar{J} = \bar{J}_{source} + \sigma\bar{E} \rightarrow Electric\ current\ density\ [ampere/meter^2] \quad (2\text{-}37)$$

$$t \rightarrow time\ [second]$$

$$\rho_e \rightarrow Electric\ charge\ density\ [coulomb/meter^3]$$

$$\rho_m \rightarrow Magnetic\ charge\ density\ [weber/meter^3]$$

$$\mu \rightarrow Magnetic\ permeability\ [henry/meter]$$

$$\sigma_{loss} \rightarrow Equivalent\ magnet\ loss\ [ohm/meter]$$

$$\varepsilon \rightarrow Electrical\ permittivity\ [farad/meter]$$

In linear, isotropic, non-dispersive, and lossy material, substituting eq. (2-34) and (2-35) in (30), eq. (30) can be re-written as:

$$\nabla \times \bar{E} = -\frac{\partial \mu H}{\partial t} - \bar{M}_{source} + \sigma_{loss}\bar{H} \quad (2\text{-}38)$$

$$\frac{\partial H}{\partial t} = -\frac{1}{\mu}[(\nabla \times \bar{E}) + (\bar{M}_{source} + \sigma_{loss}\bar{H})] \quad (2\text{-}39)$$

Eq. (31) can be re-written substituting eq. (2-36) and (2-37):

$$\frac{\partial \bar{E}}{\partial t} = \frac{1}{\varepsilon}[(\nabla \times \bar{H}) - (J_{source} + \sigma \bar{E})] \tag{2-40}$$

Equation (2-39) and (2-40) form the basis of the FDTD calculation, which explores electromagnetic wave behavior. Eq. (2-39) expresses the time-dependent magnetic field behavior with respect to the spatial variation of the electric field whereas eq. (2-40) describes the time-dependent electric field behavior with respect to the spatial variation of the magnet field. These vector forms can be expanded to a 3-dimensional expression in three different coordinate systems if needed. Maxwell – Faraday's equation (eq. 2-39) and the Ampere – Maxwell law (eq. 2-40) are used for FDTD EM wave analysis.

To discretize the continuous equation (eq. 2-39 and 2-40), Yee's algorithm has introduced which rectangular lattice can be expressed as:

$$(i, j, k) = (i\Delta x, j\Delta y, k\Delta z) \tag{2-41}$$

Where $\Delta x, \Delta y, and\ \Delta z$ are space increments in three axis directions and $i, j, and\ k$ are arbitrary integers at a given time increment, Δt. Incorporating the time (t) into eq. (41), any given function, f, in a discrete space and time can be written as:

$$f(i\Delta x, j\Delta y, k\Delta z, n\Delta t) = f^{n}_{i,j,k} \tag{2-42}$$

Where n is an arbitrary integer. Yee then used central-difference approximation for the spatial variation and the time variation for the function, *f*, which is shown below:

$$\frac{\partial f(i\Delta x,j\Delta y,k\Delta z,n\Delta t)}{\partial x} = \frac{f^n\left(i+\frac{1}{2}j,k\right)-f^n(i-\frac{1}{2}j,k)}{\Delta x} + \sout{error(\Delta x^2)} \quad (2\text{-}43)$$

$$\frac{\partial f(i\Delta x,j\Delta y,k\Delta z,n\Delta t)}{\partial t} = \frac{f^{n+1/2}(i,j,k)-f^{n-1/2}(i,j,k)}{\Delta t} + \sout{error(\Delta t^2)} \quad (2\text{-}44)$$

Using eq. (2-43) and (2-44), ignoring the error term, eq. (2-39) and (2-40) can be expressed in scalar form in a Cartesian coordinate system, for example, at $(i, j, k+\frac{1}{2}, n)$:

$$\frac{\partial H_x}{\partial t} = -\frac{1}{\mu}\left[\left(\frac{\partial E_z}{\partial y}-\frac{\partial E_y}{\partial z}\right)+\left(M_{source,x}+\sigma_{loss}H_x\right)\right] \quad (2\text{-}45)$$

And $\frac{\partial H_x}{\partial t}$, the left side of eq. (2-45), can be expanded by substituting eq. (2-44):

$$\frac{\partial H_x}{\partial t} = \frac{H_{x(i,j,k+\frac{1}{2},n+1/2)}-H_{x(i,j,k+\frac{1}{2},n-1/2)}}{\Delta t} \quad (2\text{-}46)$$

The right side of eq. (2-45) can be expanded similarly:

$$-\frac{1}{\mu_{i,j,k+1/2}}\left[\left(\frac{E_{z(i,j+1/2,k+1/2,n)}-E_{z(i,j-1/2,k+1/2,n)}}{\Delta y}-\frac{E_{y(i,j,k+1,n)}-E_{y(i,j,k,n)}}{\Delta z}\right)+\left(M_{source,x(i,j,k+1/2,n)}+\sigma_{loss,x(i,j,k+1/2,n)}H_{x(i,j,k+1/2,n)}\right)\right] \quad (2\text{-}47)$$

and $H_{x(i,j,k+1/2,n)}$ can be the approximate average between time point at n-1/2 and n+1/2:

$$H_{x(i,j,k+1/2,n)} = \frac{H_{x\left(i,j,k+\frac{1}{2},n+\frac{1}{2}\right)}+H_{x(i,j,k+\frac{1}{2},n-\frac{1}{2})}}{2} \quad (2\text{-}48)$$

Eq. (2-45) in central-difference approximation form is:

$$\frac{H_{x(i,j,k+\frac{1}{2},n+1/2)}-H_{x(i,j,k+\frac{1}{2},n-1/2)}}{\Delta t}=-\frac{1}{\mu_{i,j,k+\frac{1}{2},n}}\left[\left(\frac{E_{z\left(i,j+\frac{1}{2},k+\frac{1}{2},n\right)}-E_{z\left(i,j-\frac{1}{2},k+\frac{1}{2},n\right)}}{\Delta y}-\frac{E_{y(i,j,k+1,n)}-E_{y(i,j,k,n)}}{\Delta z}\right)+\left(M_{source,x\left(i,j,k+\frac{1}{2},n\right)}+\sigma_{loss,x\left(i,j,k+\frac{1}{2},n\right)}\left(\frac{H_{x\left(i,j,k+\frac{1}{2},n+\frac{1}{2}\right)}+H_{x\left(i,j,k+\frac{1}{2},n-\frac{1}{2}\right)}}{2}\right)\right)\right]$$

(2-49)

When eq. (2-49) is re-arranged by leaving $H_{x\left(i,j,k+\frac{1}{2},n+\frac{1}{2}\right)}$ on the left side, we get:

$$H_{x\left(i,j,k+\frac{1}{2},n+\frac{1}{2}\right)}=\left(\frac{1-\frac{\Delta t\sigma_{loss,x\left(i,j,k+\frac{1}{2},n\right)}}{2\mu_{i,j,k+\frac{1}{2},n}}}{1+\frac{\Delta t\sigma_{loss,x\left(i,j,k+\frac{1}{2},n\right)}}{2\mu_{i,j,k+\frac{1}{2},n}}}\right)H_{x\left(i,j,k+\frac{1}{2},n-\frac{1}{2}\right)}+\left(\frac{\frac{\Delta t}{\mu_{i,j,k+\frac{1}{2},n}}}{1+\frac{\Delta t\sigma_{loss,x\left(i,j,k+\frac{1}{2},n\right)}}{2\mu_{i,j,k+\frac{1}{2},n}}}\right)\left(\frac{E_{y(i,j,k+1,n)}-E_{y(i,j,k,n)}}{\Delta z}-\frac{E_{z\left(i,j+\frac{1}{2},k+\frac{1}{2},n\right)}-E_{z\left(i,j-\frac{1}{2},k+\frac{1}{2},n\right)}}{\Delta y}-M_{source,x\left(i,j,k+\frac{1}{2},n\right)}\right)$$

(2-50)

A similar approach can be used with the X-component of the electric field in eq. (2-40):

$$\frac{\partial E_x}{\partial t}=\frac{1}{\varepsilon}\left[\left(\frac{\partial H_y}{\partial z}-\frac{\partial H_z}{\partial y}\right)-\left(J_{source,x}+\sigma E_x\right)\right] \quad (2\text{-}51)$$

$$E_{x\left(i,j,k+\frac{1}{2},n+\frac{1}{2}\right)}=\left(\frac{1-\frac{\Delta t\sigma_{x\left(i,j,k+\frac{1}{2},n\right)}}{2\varepsilon_{i,j,k+\frac{1}{2},n}}}{1+\frac{\Delta t\sigma_{x\left(i,j,k+\frac{1}{2},n\right)}}{2\varepsilon_{i,j,k+\frac{1}{2},n}}}\right)E_{x\left(i,j,k+\frac{1}{2},n-\frac{1}{2}\right)}+\left(\frac{\frac{\Delta t}{\varepsilon_{i,j,k+\frac{1}{2},n}}}{1+\frac{\Delta t\sigma_{x\left(i,j,k+\frac{1}{2},n\right)}}{2\varepsilon_{i,j,k+\frac{1}{2},n}}}\right)\left(\frac{H_{z(i,j,k+1,n)}-H_{z(i,j,k,n)}}{\Delta y}-\frac{H_{y\left(i,j+\frac{1}{2},k+\frac{1}{2},n\right)}-H_{y\left(i,j-\frac{1}{2},k+\frac{1}{2},n\right)}}{\Delta z}-J_{source,x\left(i,j,k+\frac{1}{2},n\right)}\right)$$

(2-52)

In a 3D cubic voxel, the Yee algorithm can be shown as an E field surrounded by an H field and vice versa (Figure 2-1).

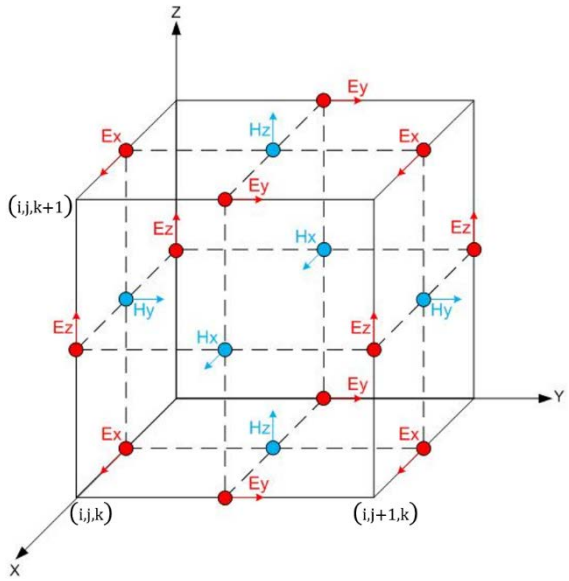

Figure 2-1 Electric and Magnetic field position with Yee's grid matrix at the i,j,k position.

Yee's algorithm for FDTD is used for direct approximation of EM wave propagation within the media [72, 113-115]. FDTD has been implemented for RF behavior analysis in different breast tissues using a specially developed RF antenna design that will be described in chapter 3 and 4 [51, 66, 68, 71, 76, 116, 117].

2.5 BREAST MRI

Breast MRI can increase the chance of early detection of breast cancer when the examination is accompanied by regular mammograms [118-120]. In a clinical breast MR examination, a gadolinium contrast enhancement technique is commonly used to detect abnormalities of the signal wash-in/-out pattern in the tissue [118, 121, 122]. Homogeneous B_1^+ excitation is required as the technique is based on spatial changes in the signal intensity over the entire breast. High-resolution imaging is also needed for accurate assessment and diagnosis of breast disease.

For example, detection of a tumor before its diameter reaches 10 mm is one of the most important factors affecting treatment type and survival rate [123, 124]. T1-weighted fat-suppressed MRI is commonly acquired to differentiate the fibroglandular (FG) tissues from surrounding fat tissues in order to categorize the breast type, that is defined by the American College of Radiology [122, 125, 126] as patients with dense FG breast tissues result in significant diagnostic challenges using a mammogram. In such cases, both high-resolution and homogeneous fat-suppression MRI are required. In addition, a fast MRI is preferable as depiction of fine morphologic details of lesions can be observed only in the early post-contrast phase, 60-120 sec [118, 121-123]. Therefore, 7T imaging with its superiority in the areas of speed and/or resolution can provide significant advantages for breast applications [30, 38, 127].

2.6 EXTREMITY (KNEE AND ANKLE) MRI

MRI plays important role in knee and ankle imaging. 1.5T and 3T are commonly used to examine the health of the cartilage, ligaments, and tendons by measuring the cartilage thickness and shape of the ligaments and tendons [1, 2, 4, 5, 7, 19, 24, 27, 28, 32, 36, 37, 54, 107, 128-134]. Among the many muscular skeleton (MSK) degenerations and disorders, Osteoarthritis (OA) is common knee degeneration and Rheumatoid arthritis (RA), which is known to initiate from thin cartilages, is common in finger joints and ankle joints [1, 2, 4, 5, 7, 19, 24, 27, 28, 32, 36, 37, 54, 107, 128-134]. The cartilage thickness at extremities does not exceed 10mm, and knee cartilages typically measure ~5-7mm at the thickest point, which is the Patella [5, 28, 129, 134]. Increases in magnetic field strength have allowed for significant advances in early detection of these degenerations as a result of the resulting high resolution MR images [5, 19, 27, 28, 129, 134]. Therefore, it is critical for MRI to provide high resolution morphologic images with high SNR.

3.0 EXPERIMENTAL AND NUMERICAL ANALYSIS OF TRANSMIT FIELD AND SAR WITH A NEW TRANSMIT ARRAY DESIGN FOR BREAST MRI

Kim, J., Krishnamurthy, N., Santini, T., Zhao, Y., Zhao, T., Bae, K. T., & Ibrahim, T. S. (2016). Experimental and numerical analysis of B1+ field and SAR with a new transmit array design for 7 T breast MRI. Journal of Magnetic Resonance, 269, 55-64.

3.1 INTRODUCTION

For high field MRI, it is critical to design RF coils that produce maximum $B1^+$ field uniformity within the ROI along with acceptable SAR levels. While taking advantage of increased SNR at 7 T, which could be 2–4 times higher than that at 3 T, multi transmit Tx arrays in conjunction with RF-shimming technique have been widely studied to improve the $B1^+$ field homogeneity and minimize the power deposition in the tissue [29, 44, 48, 51, 57, 66, 68, 71, 73, 76, 135, 136].

When the static (B0) magnetic field strength increases: reaching 7 T and beyond, its operating wavelength becomes shorter or comparable to the object being imaged and the interactions between the biological tissue and the electromagnetic fields produced by the RF coil become more complex when compared to that observed at lower magnetic field strengths. At

higher fields, constructive/destructive interference can create signal void regions [49-51] and potential higher local SARs.

Studies have reported that these variations can yield undesired signal changes in breast MRI which can lead to misinterpretation, less reproducibility, inaccuracy of assessing the changes in the ROI and increased SAR [3, 26, 113, 135, 137, 138]. It has also been recognized that $B1^+$ field inhomogeneity can be improved through a careful increase of the volume of the RF coil [48, 139].

RF-shimming can be performed and evaluated in vivo; however, in vivo SAR measurements are not usually considered feasible. Temperature rises due to the RF heating have been studied with phantoms and/or animal models; such studies are however rare in humans due to complexities and safety concerns [42, 48, 66, 112, 140, 141]. This has led to extensive use of numerical modeling to predict SAR distributions with anatomically detailed human models for safety evaluations in high field MRI [39, 42, 48, 51, 57, 66, 68, 76, 112, 116, 117].

In this work, a new RF array system that has multiple excitation sources (8) which can be independently driven (with different magnitude and/or phase) was developed and mathematically analyzed for breast imaging at 7 T. Numerical and experimental studies were performed and quantitatively analyzed to evaluate the RF breast coil. Specifically, we have developed an eight-channel, two sided 2-by-2 cross-pole [18, 142, 143] or TTT 7 T RF array for the breast region.

The developed RF array inherently shows high couplings (S13 = -3 dB and S12 = -9 dB) between the excitation elements thus the $B1^+$ field intensity per supplied (by the system) power is typically lower than the traditional breast RF coils, however, the array exhibits more homogeneous $B1^+$ field distributions in the breast tissue. Also, due to high coupling between the coil elements, our design shows less loading dependency than traditional coil designs and

therefore does not require tuning, matching or RF shimming from subject to subject. Additionally, while many high field breast MRI studies published promising results [3, 26, 53, 84, 108, 135, 137, 138, 144-146]; to our knowledge, so far, only one study has evaluated $B1^+$ field and peak/average SAR variations in different breast models and compared to breast phantoms [58].

In our study, numerical analysis was performed using FDTD method in a homogeneous spherical model and in four different breast models. Mean $B1^+$ field intensity (μT) achieved for 1Watt of supplied power and CoV (standard deviation/mean) were calculated. Peak and average SAR (W/kg) were calculated in order to achieve a $B1^+$ field intensity of 2 μT in different regions of the breast models. In addition to the different breast model comparisons, $B1^+$ field and peak/average SAR were calculated in two additional settings: (1) breast model merged with 3D human female torso, ‘‘full body model”, to evaluate the influence of the chest regions, and (2) without the RF shield around the breast regions to evaluate the effects of the RF shield [81, 147, 148]. Furthermore, experimental $B1^+$ field maps were acquired in a homogeneous spherical phantom and in the ‘‘Bphantom” which consists of 50% glandular and 50% adipose tissue with 8–10 cystic masses typically used for biopsy training (Supertech, IN). The temperature rises due to the RF power absorption were measured using fiber optic probes (Neoptix, Canada) with the same Bphantom.

3.2 MATERIALS AND METHODS

3.2.1 RF Array Design

Transmission line elements (coaxial line with solid squared shaped inner copper rod and an outer copper strut) were adapted for our two-sided 2 x 2 TTT RF coil [148]. The inner copper rod (40 mm in length) is inserted inside a hollow squared shaped polycarbonate tube which is surrounded with a copper sheet (note, each rod is inserted up to ~40 mm such that it does not pass through other rods at cross-over joint). The inner copper rods are electrically connected to the surrounding RF copper shield and the outer copper struts are all electrically connected (Figure 3-1).

The array can be tuned and matched by pushing/pulling the inner copper rods inside the outer copper struts which effectively change the lengths of the transmission lines and therefore the associated capacitance and inductance (Figure 3-1A).

We used a total of eight squared shaped coaxial lines measured 25.4 x 25.4 mm^2 (on the outside) and 19.0 x 19.0 mm^2 (on the inside). The coaxial elements on each side of the four struts were placed in the shape of a tic-tac-toe (Figure 3-1). On four alternating channels per side, the coaxial center pin of each RF excitation port was connected to the outer strut immediately above it and the ground of the port was connected to the RF shield.

Each side was constructed on a 170 x 170 mm^2 acrylic frame (Figure 3-1A). Two sides were then assembled with a 127 x 170 x 170 mm^3 copper shield box to decrease the radiation loss and increase RF efficiency [149] (green dotted line in Figure 3-1B).

Approximate lengths of the matching and the tuning rods that need to be inserted in their respective outer struts were calculated using full wave FDTD simulations. After assembly, fine tuning/matching adjustments were then done on the bench. Each side contained four RF excitation ports and all eight excitation ports were tuned and matched to 297.2 MHz and scattering (S) matrix were measured using vector network analyzer (HP, USA). Figure 3-1C shows the MR images of the Bphantom that was used in this study. The current useable volume of the array (cavity) is 12.7 x 17.0 x 17.0 cm^3 which is marginally larger than the volume of the breast model/phantom possibly resulting in a lower $B1^+$ field intensity for a given RF power supplied by the system. Due to the structure of this design (see Figure 3-1) however, this arrangement has a negative impact on the $B1^+$ field homogeneity as the breast phantom is not positioned inside the array's central volume, ''sweet spot", which is at a deeper location toward the magnet table.

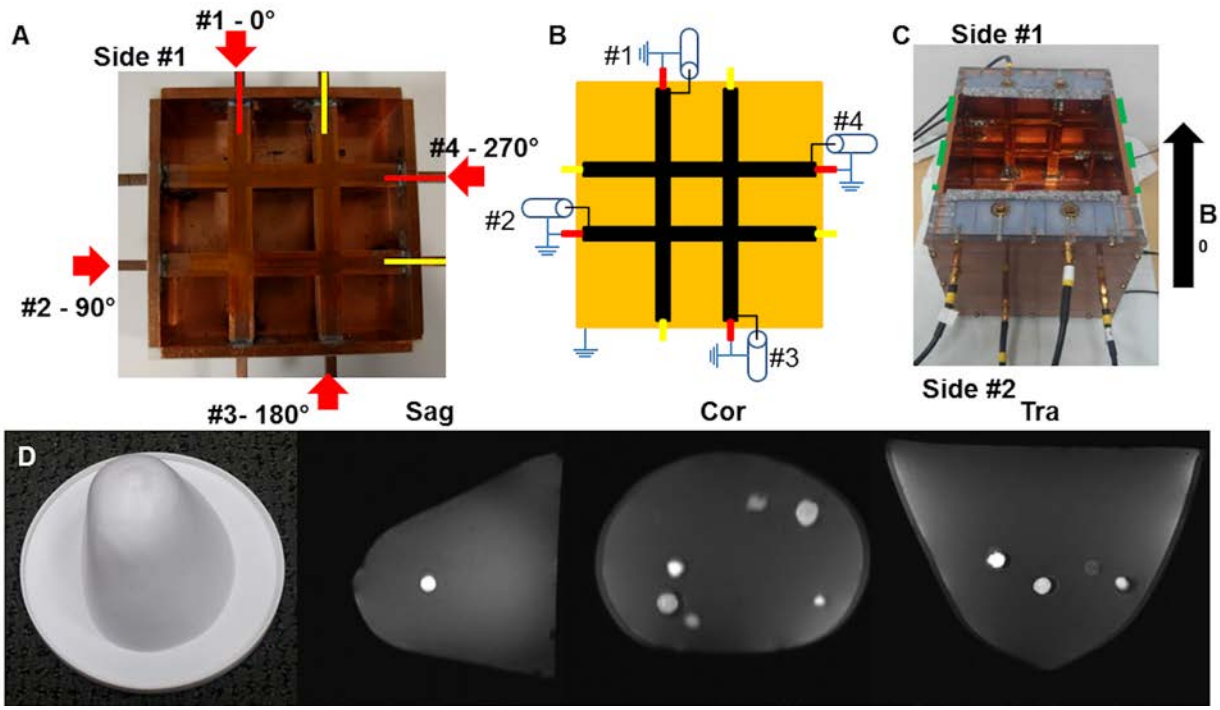

Figure 3-1 Constructed TTT Tx array, schematic diagram of one side of the array and breast phantom (A–D). (A) One side of TTT RF array showing four excitation ports. Phases (90º increment) applied in the side #1 were in a clockwise rotation whereas the same phases were applied in counterclockwise rotation in side #2. Red arrows represent four excitation ports that can be matched by pulling/pushing the solid copper rods (red bar represent matching rods and yellow bar represent tuning rods). (B) Schematic of one side of Tx coil showing electrical connection between each ports and RF shield. Red/yellow bars represent the inner matching and tuning copper rods connected to the RF ground and orange box represents RF shield. Black lines and bars represent the electrical connections to the four excitation center pins. (C) Top view of assembled RF coil. RF shield box (green dotted line) was attached to the two sides. (D) Picture and MR images of the BPhantom in three different planes. Dimensions of the BPhantom are 120 x 100 x 90 mm^3 and the volume is 500 cc.

3.2.2 FDTD Calculations and Breast Models

An in-house FDTD model of a 2-sided 2 _ 2 TTT RF array was developed (Figure 3-2A–C) where a 3-Dimentional (D) geometry of the array was created using MATLAB (Mathworks, MA). A grid matrix composed of $166 / 166 / 143$ cells with a spatial resolution of ($1.587\ mm^3$) and a temporal resolution of (3×10^{-12} sec) was used to meet the Courants stability criterion [72] [46]. The computational domain was surrounded with 32 layers of perfectly matched layer (PML) as absorbing boundary conditions [150]. Four 3D breast models developed at the University of Wisconsin Madison (http://uwcem.ece.wisc.edu/phantomRepository.html) were used for this study (Figure 3-3A-D). The breast models used in this study are (1) mostly fat breast model (mFBM, <25% glandular, 60 x 71x 50 grid cells in x, y, z-direction), (2) scattered fibroglandular (FG) breast model (sFGBM, 25–50% glandular, 57 x 70 x 61 grid cells), (3) heterogeneously dense breast model (hDBM, 50–75% glandular, 43 x 73 x 49 grid cells) and (4) very dense breast model (vDBM, >75% glandular, 40 x 65 x 42 grid cells) type defined by the American College of Radiology. Each model is comprised of a 3D grid of cubic voxels (0.5x 0.5 x 0.5 mm^3) that was later interpolated to match the spatial resolution of the coil geometry. Six different tissues were used and tissues conductivity and dielectric constant were set to that associated with the Larmor frequency of 7 T (297 MHz, see Table 3-1). In addition, a spherical model (diameter = 100 mm, Conductivity = 0.46 (S/m) and Relative Permittivity = 79) was also utilized in the FDTD calculations. To investigate the effect of full body inclusion, we merged sFGBM to virtual family ‘‘Ella” model [151]. First, Ella model (530 x 300 x 1680 grid cells, and 1 x 1 x $1mm^3$ cubic voxel) was cropped 300 mm from the top of head to 550 mm in z-direction which encompasses chest and breast area. Second, cropped model was then interpolated to the

spatial resolution of the computational domain (1.587 mm^3). Third, since the Ella was developed in supine position where breast tissues were pulled down by gravity, these breast tissues were removed and replaced with sFGBM. The same sFGBM was also used for simulation with and without RF shield. Total of 40 grid cells from the center of the RF shield (20 cells toward head and 20 cells toward foot) were removed. In the FDTD geometrical configuration, the four breast models and the spherical model were centered inside the RF array to mimic the experimental settings (see Figure 3-2A and B). The electromagnetic fields (both electric and magnetic field) and reflection (Sxx)/transmission (Sxy) coefficients from eight excitation ports/channels were calculated with the FDTD software using a true transmission line model for excitation [17,20,21,23]. Calculated electromagnetic fields from each port were linearly superimposed with different phases and $B1^+$ field distribution and SAR were obtained. The (1) mean $B1^+$ field intensity (μT) per 1W of RF power supplied by the system and the (2) CoV of the $B1^+$ field were calculated at three different planes and for entire volume for the 4 breast models and the spherical model. In addition, peak SAR (W/kg) was calculated using the following equation and was determined for 10 gram pixel average:

$$SAR_{(i,j,k)} = \frac{1}{2}\left\{\frac{\sigma_{(i,j,k)}\left(E^2_{x(i,j,k)}+E^2_{y(i,j,k)}+E^2_{z(i,j,k)}\right)}{\rho_{(i,j,k)}}\right\} \quad (3\text{-}1)$$

where sigma (r) is the conductivity and rho (q) is the density of tissues in the sample. The density of the breast is determined by the tissue composition ratio of fat to connective tissue. i, j, and k represent locations in the Cartesian coordinate system.

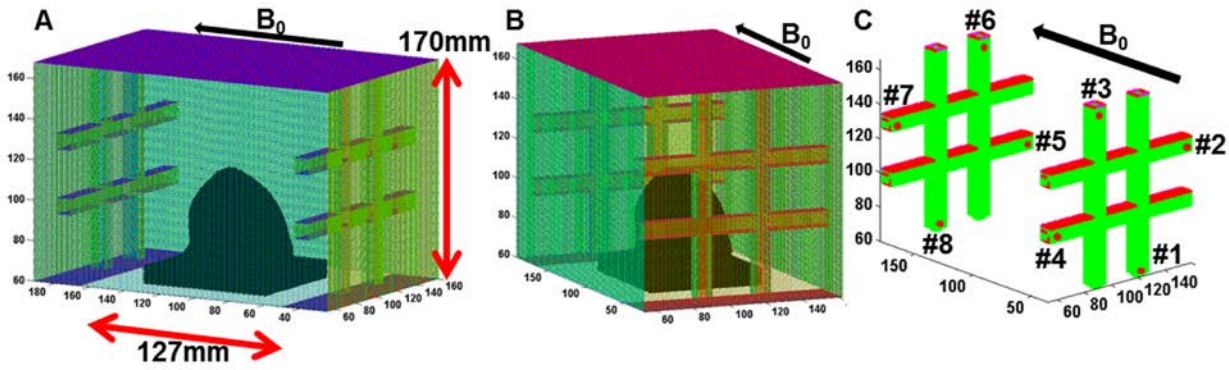

Figure 3-2 FDTD model of TTT Tx array with 3D breast model co-centered at the bottom of the coil (A and B). Total grid of 162 * 162 * 168 cells was used in the computational domain. Sagittal (A) and transverse (B) plane views of the RF coil and the breast model are shown. Two sides of 170 X 170 mm^2 RF array were 127 mm apart and RF shield box dimensions were 127 X 170 mm^2. (C) Eight excitation ports (no RF shield) are shown. Red dot represents the excitation source points at each port.

Table 3-1. Conductivity (σ), dielectric constant (ε_r), tissue density (ρ) and composition ratio of six tissues for four breast models.

Tissue type	Conductivity (σ)	Dielectric constant (ε_r)	Tissue Density (ρ)	Tissue ratio (% per Vol.)			
				mFBM	sFGBM	hDBM	vDBM
Air	0	1	0	30.7%	36.2%	35.6%	32%
Fibroglandular	0.288065	26.8181	1013	3.2%	5.3%	14.2%	17.7%
Breast	0.445135	34.0537	928	1.9%	10.6%	11%	11.3%
Fat	0.039539	5.6354	916	58.6%	42.8%	33.5%	31.7%
Muscle	0.77	58.229	1041	3.3%	3.5%	4.1%	5.1%
Skin	0.64038	49.902	1100	2.1%	1.5%	1.5%	2.4%

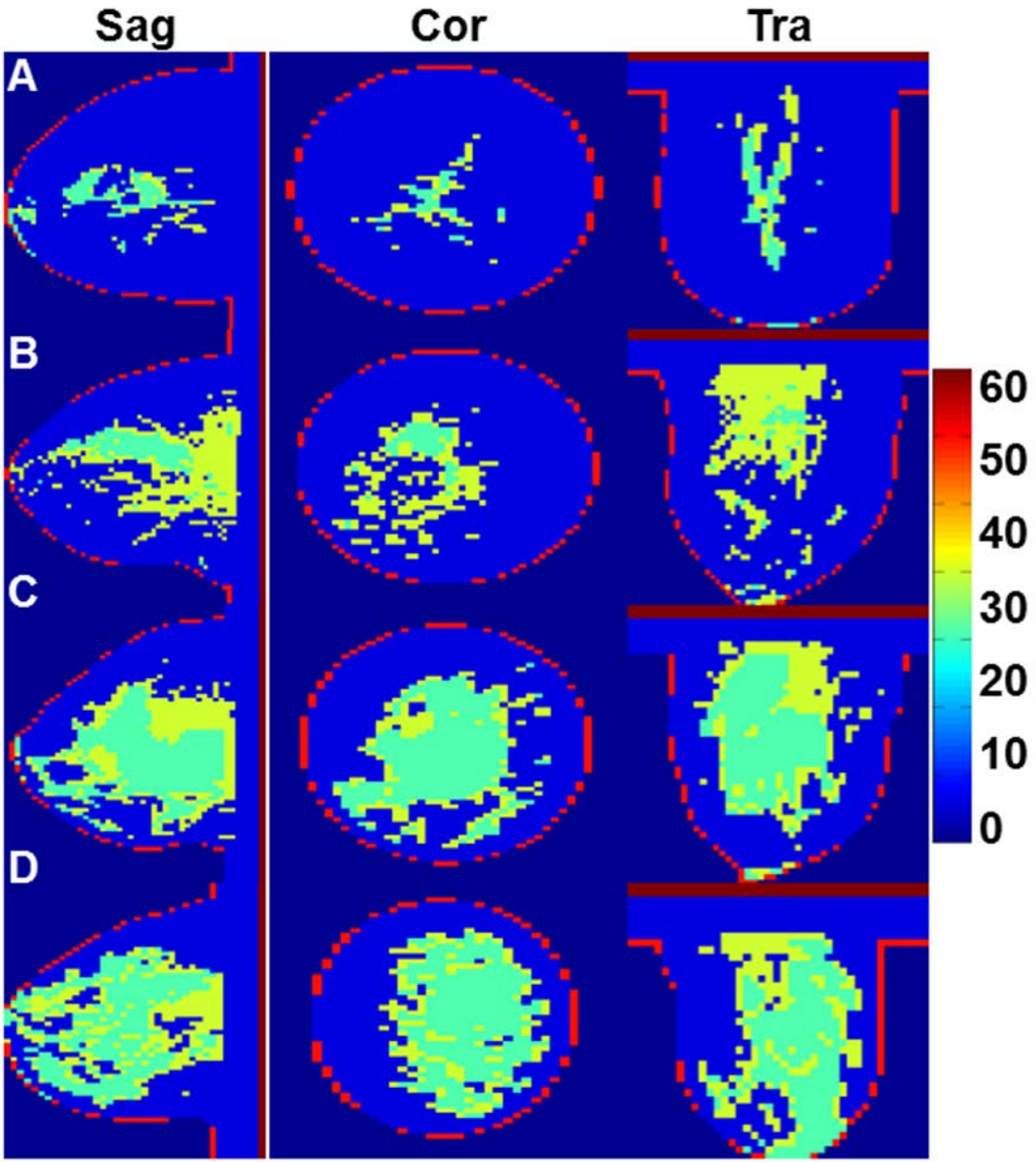

Figure 3-3 Permittivity map of four 3D anatomically detailed breast models used in FDTD calculations. (A) mFBM: <25% glandular (B) sFGBM: 25-50% glandular (C) hDBM: 50-75% glandular and (D) vDBM: >75% glandular. The phantom models consisted of six tissues with air surrounding. The colorbar represents the relative permittivity of the tissues in the model.

3.2.3 Imaging Studies and Temperature Measurements

All imaging studies were performed on a 7 T human MR scanner (Siemens Medical System, Erlangen, Germany). We used (1) 4 ports with 90^o phase increments in the clockwise direction (Figure3-1A) on one side and 4 ports with 90^o phase increment in counter clockwise direction on the opposing side and (2) equal amplitudes (on all 8 ports) in order to produce an approximate circular polarization (CP) mode. In order to transmit RF power to the eight excitation ports, we used an 8-way Wilkinson power divider and 8 T/R switches with above mentioned phase set up on the transmit chain. A 3D $B1^+$ field map was acquired with modified turbo flash (TFL) sequence [152] where a presaturation module was inserted before each partition to create varied z-magnetization. The presaturation module consists of a rectangular RF pulse (1 ms) and followed by a set of trapezoidal gradient crushers applied on all three axes simultaneously. The crusher gradients' duration is 8 ms with the peak amplitude = 13 mT/m. The design was achieved to minimize the T1 relaxation effects between the presaturation pulse and excitation pulse. The nominal flip angle (8 steps) for the presaturation pulse was varied from 0^o to 160^o. Sequence parameters were: TR/TE = 2000/1.5 ms, voxel Resolution = 3.0 x 3.0 x 3.0 mm^3, flip angle for excitation pulse = 8^o, data acquisition bandwidth is 1500 Hz per Pixel. Acquired data was then fitted to the cosine function using MATLAB (Mathworks, MA).

Four thermal fiber optic probes were inserted in the Bphantom in order to measure the temperature rise due to RF power absorption. Locations of the inserted probes were set based on the local hot spots from simulation results shown in Figure 3-7 (SAR distribution). Three probes were placed ~5–10 mm from the phantom boundary (30 mm in depth) and one probe was inserted at the center of the phantom (50 mm in depth). The RF coil and the Bphantom were

placed in the MR scanner for 20 min prior to the experiment. Baseline temperature was measured for 10 min and the RF pulse was applied with X, Y, Z- gradients turned off. 9Wcontinuous wave per channel (total of 8 Tx lines) was applied in the Bphantom to induce RF heating. Sequence parameters are; TR/TE = 50/1.5 ms and RF pulse duration = 3 ms. Each scan time was 2 min long and was sequentially repeated 5 times. Temperature measurements using Neoptix (http://www.neoptix.com/reflex.asp) were captured at the 4 probe locations with the 1 s temporal resolution for a total duration of 40 min (10 min prior to the start of the scan, 10 min scan and 20 min after the scan).

3.3 RESULTS

3.3.1 Coupling: Simulation and Measurements

S parameters of the TTT array loaded with different breast models were calculated utilizing the FDTD in-house package and compared with experimental measurements (Figure 3-4). Without retuning/re-matching (numerically as well as experimentally) between different loads, the mean numerically calculated S11 with the 4 different breast models as well as the spherical model was -20 dB whereas -24 dB was measured with the analyzer (loaded with spherical phantom, and Bphantom as shown in Figure 3-4A and B). The mean transmission coefficient S13 (two excitation ports that are parallel to each other: see Figure 3-1A) of -3 dB was calculated from the simulation which was comparable to the experimental measurements. In addition, mean S12 (two orthogonal excitation ports: see Figure 3-1A) of -9 dB was calculated and measured.

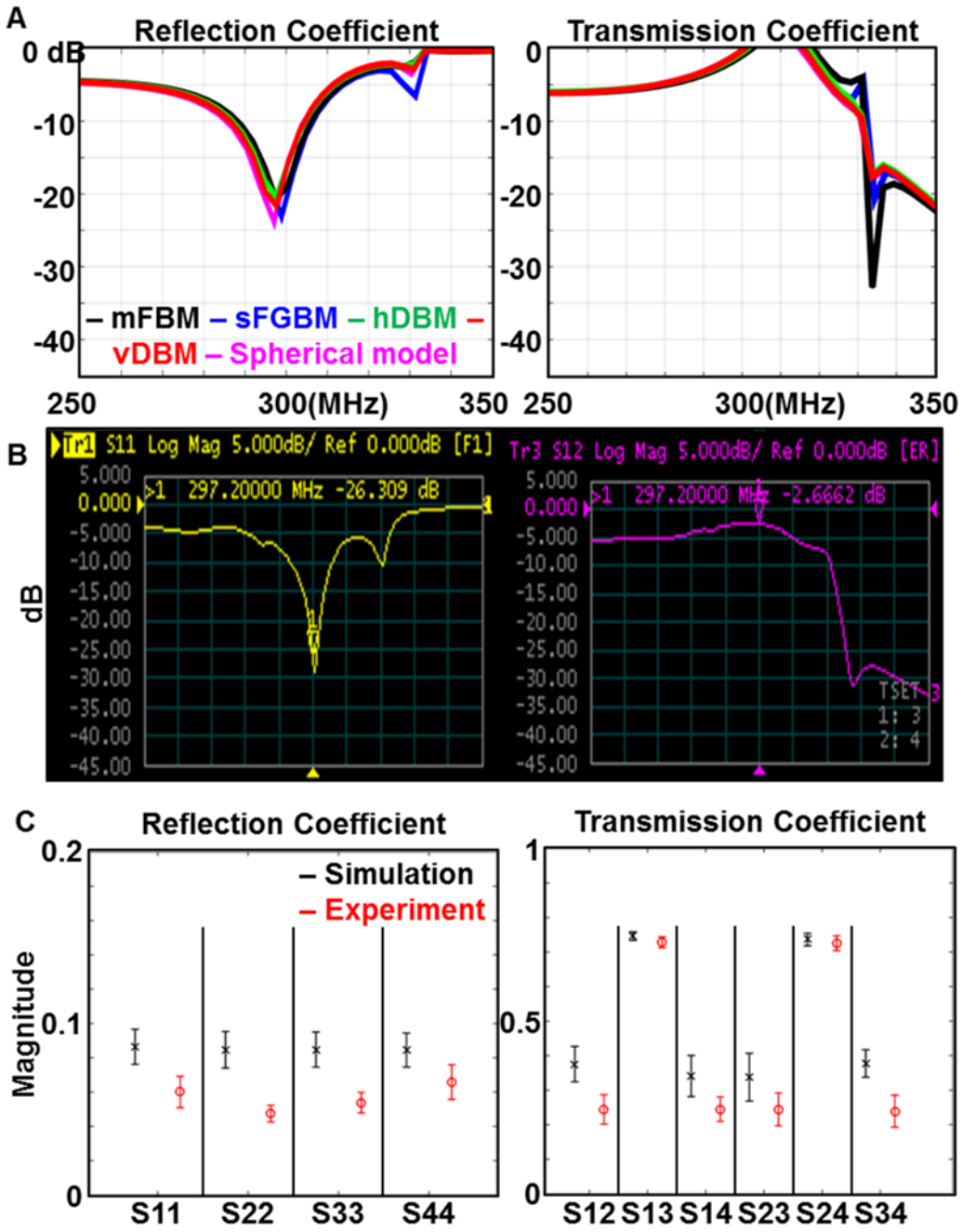

Figure 3-4 S-matrix calculated from four breast models and spherical model and measured from the Bphantom and spherical phantom. (A) FDTD calculated S11 and S13 comparison between four different breast models and the spherical model. (B) Measured S11 and S13 of the spherical phantom utilizing vector network analyzer (showing very good agreement with (A)). Note that, the high coupling (~-3 dB) at S13 is intrinsic characteristic of the TTT RF coil. (C) The mean transmission/reflection coefficient comparison

between the simulations and experiments. The simulations were obtained with the four breast models and the spherical model whereas the experiments were obtained with the spherical phantom and the Bphantom.

3.3.2 B_1^+ Field Distribution and Intensity: Simulation and Measurements

The mean $B1^+$ field intensity (per 1W of RF power supplied by the system) calculated from the homogeneous spherical model in sagittal, coronal, transverse planes and entire volume are 3.54, 3.47, 3.56, and 3.50 (μT) whereas measured (using experimentally obtained $B1^+$ field map) from the phantom are 3.41, 3.33, 3.42, and 3.39 (μT), respectively. In both the simulations and experiments, high $B1^+$ field intensity at the center of the phantom was observed with symmetric $B1^+$ field profile which is expected at the CP mode (Figure 3-5A and B). Figure 3-6 shows the $B1^+$ field map calculated/measured in the 4 breast models and the Bphantom. The mean $B1^+$ field intensity (μT) per 1W of RF power supplied by the system and CoV at sagittal, coronal, and transverse plane are summarized in Table 3-2. Highest normalized mean $B1^+$ field intensity was measured in coronal plane while the values in the sagittal and transverse planes were similar for each breast model as well as Bphantom (see Table 3-2). $B1^+$ field intensity decreases toward the chest wall was clearly visible in sagittal and transverse planes (Figure 3-6A). mFBM had highest mean $B1^+$ field intensity (μT) per 1W of RF power supplied by the system in entire volume and decreased as the ratio of FG tissue increased (mFBM – 1.61, sFGBM – 1.53, hDBM – 1.51, vDBM – 1.44, Bphantom – 1.36). The lowest CoV was calculated in vDBM and increased as fat ratio increased (Figure 3-6C and Table 3-2). In the coronal plane, the four breast models had relatively low mean $B1^+$ field intensity (μT) per 1W of RF power supplied by the system; however, the standard deviation (SD) was also low therefore high homogeneity (low CoV) was achievable, 4–7%. In the sagittal and transverse planes, larger SD

due to the $B1^+$ field decay at the chest wall resulted in lower homogeneity, CoV of ~16–26%. Due to experimental measurement errors in the BPhantom (inside the cyst masses) highest CoV was measured in the Bphantom in all three planes, especially in coronal plane (Figure 3-6B). However, the volume average measurements showed comparable results which varied between 18% and 26% (Figure 3-6C). In addition, when the chest wall was excluded in all four breast models (see white dotted line in Figure 3-6A), the CoV decreased significantly (mFBM – 13%, sFGBM – 12%, hDBM – 11% and vDBM – 9%).

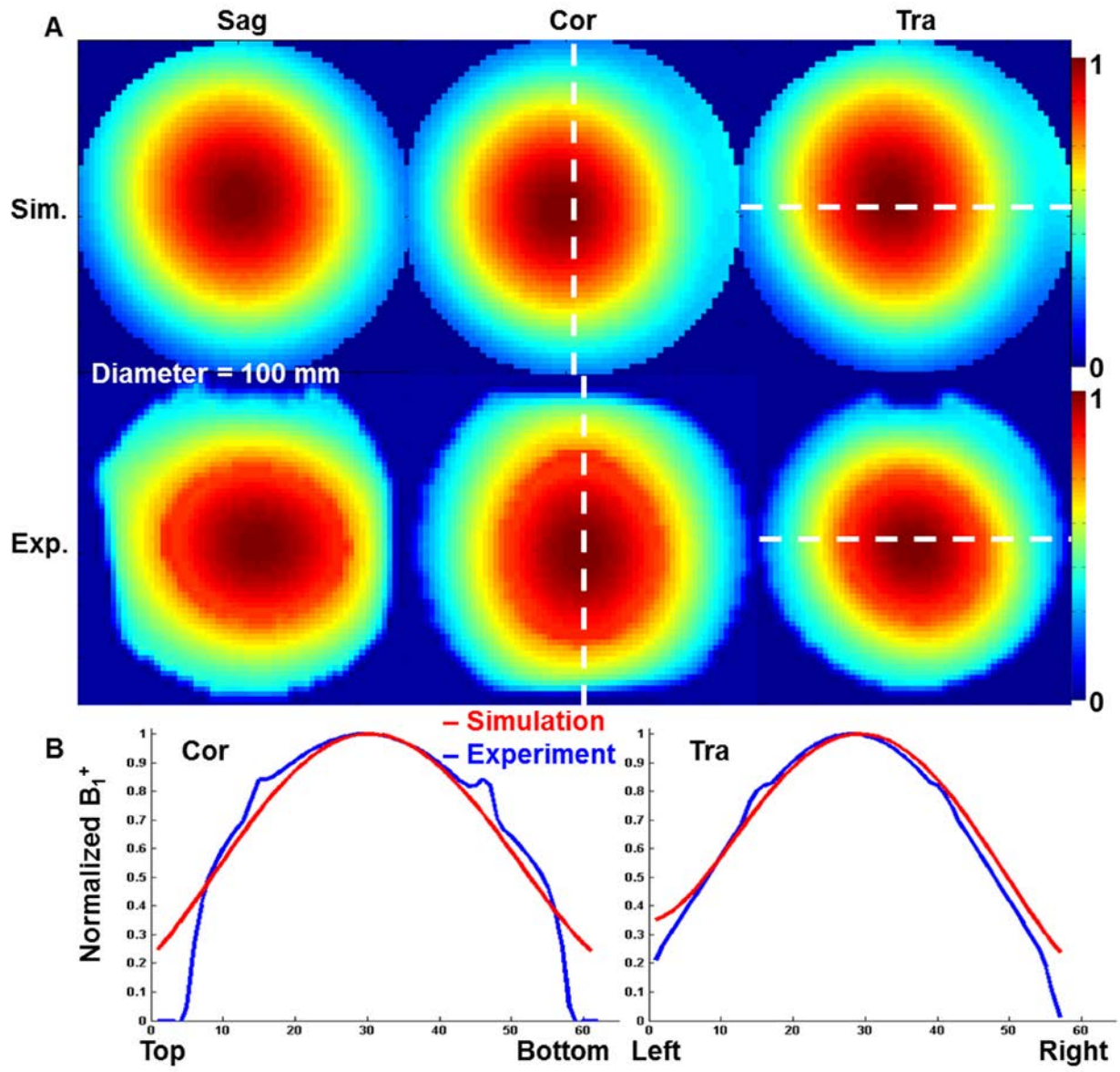

Figure 3-5 (A) Simulated/measured B_1^+ distribution from the homogeneous spherical phantom at three different planes (B_1^+ was normalized with the local maximum B_1^+ intensity). (B) Signal profile comparison (white dotted line in (A)) in the coronal and transverse planes; x axis represents pixel points. Diameter of the phantom/model is 100 mm.

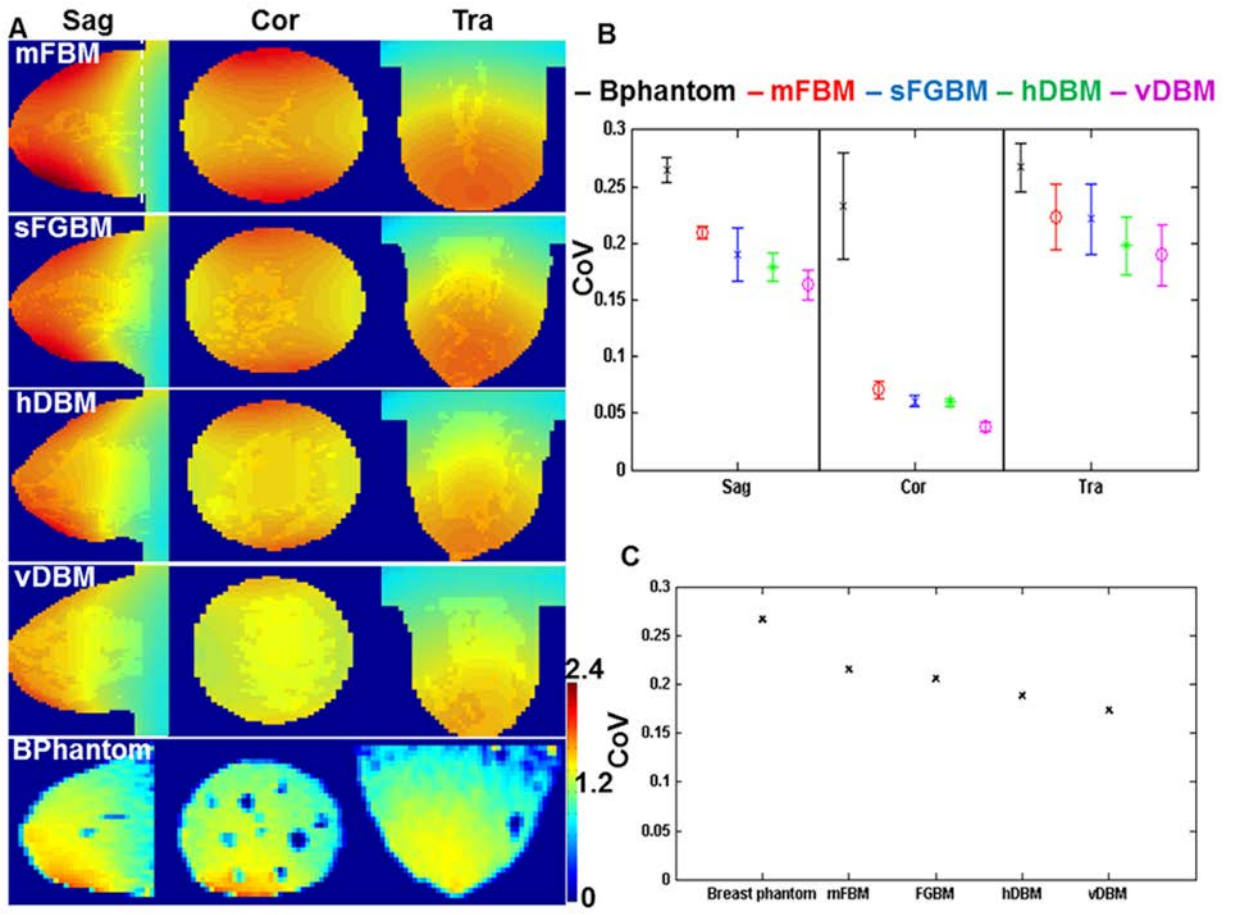

Figure 3-6 (A) B_1^+ maps (uT/W) calculated in the four breast models (simulations) and measured experimentally in the Bphantom. Note, white dotted line is the border of the chest wall used for CoV calculation labeled "without the chest wall". B_1^+ map was normalized to the maximum B_1^+ measured in the model (2.38 uT/W in mFBM). (B) Mean CoV at three different planes. (C) CoV over the entire volume.

3.3.3 SAR Simulation and Temperature Measurements

The SAR (per a mean $B1^+$ field intensity of 2 μT) distribution associated with the calculated $B1^+$ field is shown in Figure 3-7. Peak/average SAR (W/kg per 10 g of tissue) calculated for all breast models are summarized in Table 3-2. The highest peak and average SAR were calculated in sFGBM. Lowest peak SAR was calculated in vDBM whereas lowest average SAR was calculated in mFBM. The peak/average SAR ratio was 3.28 in mFBM, 2.73 in sFGBM, 2.51 in hDBM and 2.40 in vDBM; the ratio decreased as the composition of FG tissue increased. Regardless of the model, the peak SAR was observed relatively close to the skin and chest wall where the conductivity was high. The SAR maps calculated in the mFBM and vDBM model show rapid decay toward the center of the breast model whereas sFGBM and hDBM show relatively uniform distribution (Figure 3-7). The temperature rise due to RF heating was measured in the Bphantom. Figure 3-7 shows probe locations and temperature changes during the RF heating created by the RF excitation described in the Methods Section. Ch1 was placed at the center of the Bphantom. Ch2 and Ch3 were placed to validate the asymmetry of the SAR calculated in the right and left side of the models. Ch4 was placed in the region where peak SAR was calculated (Figure 3-7). The baseline temperature at the four probes was ~18.5 ^oC and during the total of five RF heating experiments (total 10 min), temperature rises were 0.31 ^oC in Ch1, 0.12 ^oC in Ch2, 0.30 ^oC in Ch3 and 0.52 ^oC in Ch4. As shown in Figure 3-7C, Ch1 temperature measurement shows a short linear increase between time = 620–650 s; steady state was then observed for 120 s between time = 650–770 s. Additional 0.2 ^oC increase was observed until the end of the measurement (~2000 s). Lowest temperature rise was measured in Ch2. Ch3

temperature rise started to occur around ~840 s and continuously increased during the experiment (Figure 3-7B). Ch4 temperature increased linearly during the first scan (600–720 s) and steady state was observed (720–840 s) during the second scan. Ch4 temperature reached steady state followed by a short increase during the third scan (Figure 3-7B). Ch4 temperature had the largest temperature rise which was 4.3 times higher than Ch2 temperature. In addition, SAR was calculated for the four breast models at Ch2 and Ch4 probe locations. The SAR calculated at Ch4 location was ~3.5–5 times higher than that calculated at Ch2 location. The measured temperature rises as well as calculated SAR values at Ch1 and Ch3 locations were comparable.

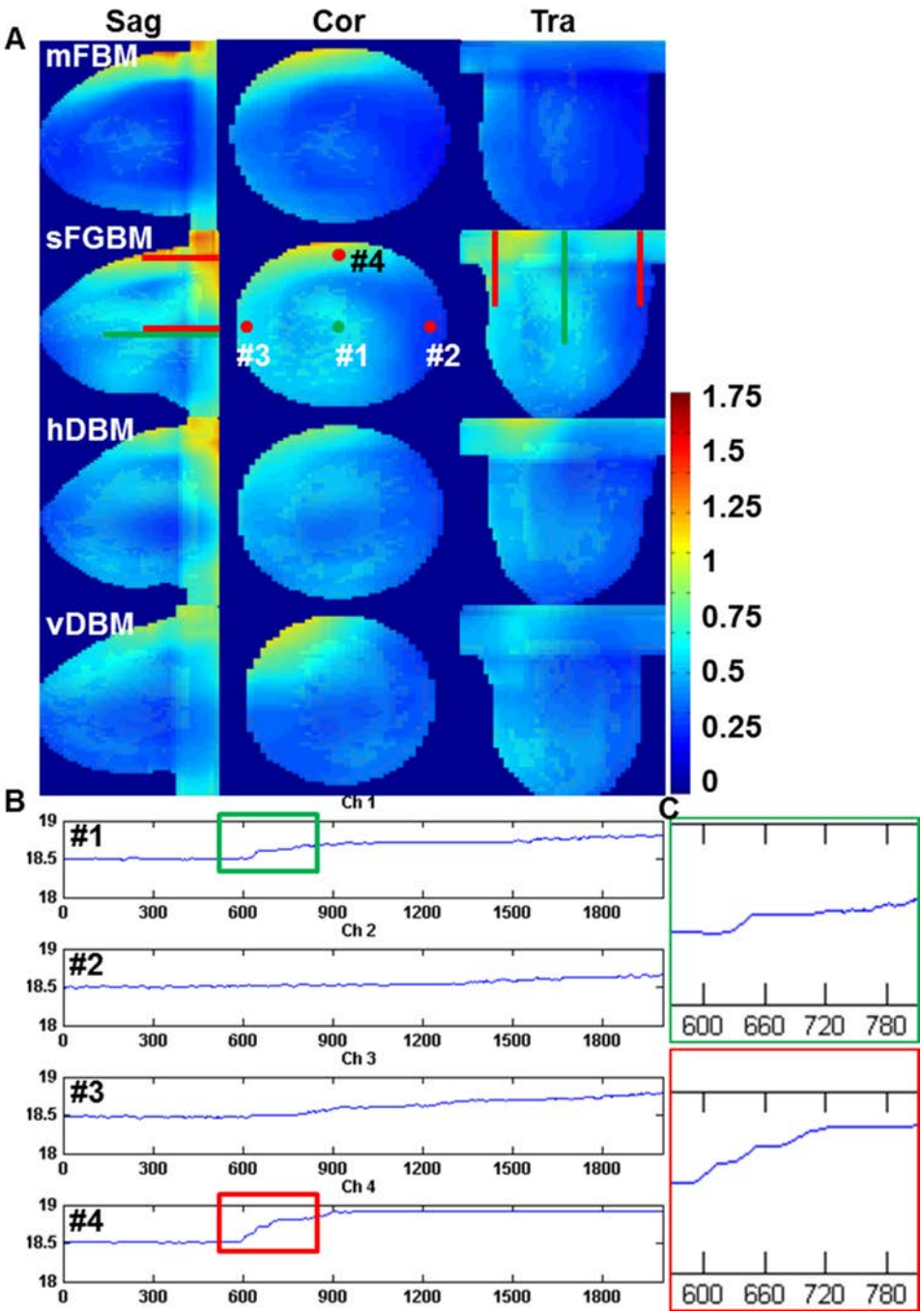

Figure 3-7 (A) SAR (W/kg) for a mean B_1^+ field of 2uT calculated in the four breast models. Peak SAR was measured close to the skin and chest wall region in all four models. The locations of the four thermal fiber optic probes used for the temperature measurements are shown as red and green bars. Three probes were inserted at the periphery of the phantom (30 mm depth, red bars) and one probe was placed at

the center of the phantom (50mm depth). Note, SAR map in four models were normalized to the highest calculated peak SAR (1.75 W/kg in sFGBM). (B) Temperature measurements at four locations in the Bphantom. (C) Zoomed-in view of the temperature rises measured from Ch1 and Ch4 during first RF heating. Note RF was applied at 600s and each scan was 2 min long and sequentially repeated for 5 times.

3.3.4 Inclusion of Torso

Mean B_1^+ (uT/W (input)) calculated in the breast tissue regions with the full body model included was 1.26 (uT/W). Although mean B_1^+ decreased by ~20% compared to sFGBM (1.56 uT/W) alone, CoV calculated in the breast regions with the full body model in Sag/Cor/Tra directions were 0.2/0.09/0.22 respectively which are comparable to that calculated in the sFGBM (see Table 3-2) without the full body model. While the average SAR with attached full body model did not change (using the same regions in both calculations), the peak SAR increased by ~30%.

Table 3-2. 1) Calculated (in the 4 breast models) and measured (in the BPhantom) mean B_1^+ intensity and CoV and 2) calculated (in the 4 breast models) peak/average SARs.

	FDTD simulations (attached with chest wall layers)				Experiment
	mFBM (Sag/Cor/Tra)	sFGBM	hDBM	vDBM	Bphantom
Mean B_1^+ (uT/W)	1.23/1.53/1.49	1.41/1.50/1.42	1.38/1.52/1.37	1.30/1.48/1.28	1.26/1.33/1.29
B_1^+ CoV (sd/mean)	0.21/0.07/0.22	0.19/0.06/0.22	0.17/0.06/0.20	0.16/0.04/0.19	0.26/0.23/0.27
Peak/Avg SAR (W/kg)	1.48/0.45	1.75/0.64	1.41/0.56	1.25/0.52	N/A

3.3.5 RF Shielding Effect

Mean B_1^+ of 0.82 (uT/W) was calculated in the identical sFGBM without RF shield which was ~45% lower than that calculated in the sFGBM with RF shield. Calculated CoV without RF shield in Sag/Cor/Tra and entire volume were 0.30/0.14/0.34 and 0.30. B_1^+ inhomogeneity increased significantly without RF shield when compared to that calculated in the sFGBM with RF shield. In addition, Peak/average SAR was ~2 times higher than that calculated in sFGBM with RF shield (3.57/1.34 VS 1.75/0.64 W/kg per 10g, see Table 3-3).

Table 3-3. Mean B_1^+ intensity, CoV and peak/average SARs comparison between sFGBM, Full body model, and without RF shield.

	sFGBM	Full body model	without RF shield
Mean B_1^+ (uT/W)	**1.53**	**1.26**	**0.82**
B_1^+ CoV (Sag/Cor/Tra)	**0.19/0.06/0.22**	**0.2/0.09/0.22**	**0.30/0.14/0.34**
Peak/Avg SAR (W/kg)	**1.75/0.64**	**2.34/0.64**	**3.57/1.34**

3.4 DISCUSSION AND CONCLUSION

The developed transmit breast array inherently exhibits high coupling (S13 = ~-3dB and S12 = -9dB) between the excitation elements thus the average B_1^+ intensity per 1 Watt input power is typically lower than traditional breast coils. Although, the average B_1^+ intensity per SAR is not lower than other traditional RF breast array designs, the proposed design exhibits more homogeneous B_1^+ distributions in the breast tissue (despite the fact that breast is not positioned at the coil's central volume or sweet spot). Also, due to high coupling between the coil elements, our design shows less load dependency and therefore tuning, matching, and RF shimming are not required per subject basis whether operating in the parallel transmission (pTx) or single transmission (sTx) modes in order to optimize the performance of the proposed array. By adjusting the rod lengths associated with the excitation elements, one can consistently achieve a matching of ~-24dB whereas changing the adjacent rods enables the tuning. This design of the RF array does not require lumped elements for tuning and/or matching. In addition, resonant frequency of the developed array is mainly determined by the geometry inductance, thus the dimension of the array should be carefully chosen based on full wave numerical simulations.

Due to the rigorous modeling of the coil including transmission line excitation, Figure 3-4A and B demonstrate very good agreement between experiment and simulations where we accurately calculate the coupling parameters which are high, and therefore well-defined in our array. Such agreement is critical in terms of assessing the electromagnetic fields during the RF coil development and evaluation. Phantom studies showed very good agreement in terms of the

B_1^+ distribution as well as intensity. Mean B_1^+ and its distributions in four breast models and Bphantom were highly consistent and were compared to that of other published high field numerical studies in the breast tissues [26, 58, 138, 146]. Brown et al. [26] showed more than 75% homogeneity within the breast tissue and McDougall et al. [53] demonstrated approximately 80% homogeneity in the breast tissues. Although B_1^+ per input power was lower than other traditional breast RF coil design by ~20-25%, B_1^+ homogeneity of ~90% (utilizing the standard quadrature set-up and without utilizing any subject specific RF shimming) in the breast tissue was achievable with our design (note that the B_1^+ distributions in our study are presented in a linear scale whereas it was noted as dB scale in Ref, #31). Note that we achieved quadrature excitation (approximate CP mode) with 90^o phase increments on each side of the array (with opposite rotation) and equal amplitudes in the sTx or combined mode. Furthermore, if needed, the developed Tx array can be used in a pTx mode where amplitudes and phases can be optimized in order to further improve the B_1^+ homogeneity and/or SAR.

Changes of the ratio (FG/fat tissue) affected the mean B_1^+ field and CoV in the breast models. Mean B_1^+ decreases as the ratio of FG tissue increase. This effect can be explained as the dielectric constant and conductivity of fat is lower than the FG tissue thus the RF penetration depth is higher in the mFBM than in vDBM. In Contrast, lowest CoV (best homogeneity) was calculated in the more conductive vDBM due to having less predominant dielectric effects. Under the influence of the torso where dielectric constant and conductivity of the tissues were relatively higher than the breast and fat tissues, mean B_1^+ per input power decreased by ~20% in the breast region with a full body model attached. On the other hand, CoV in the breast region and average SAR with a full body model attached were comparable to that measured in sFGBM alone. Consistency of the B_1^+ distributions in the breast regions in different models can be

explained by the high coupling attributes between array elements. Due to the high coupling between the excitation ports, sample placed inside the RF coil which dominates loading effect became small and B_1^+ distributions were predominated by the coil structure. In addition, when B_1^+ field and peak/average SAR were calculated without RF shield, significant decrease of B_1^+ and increase of peak/average SAR was calculated. While there was a limitation of using 4 probes to accurately represent the temperature distribution in the Bphantom, the temperature measurements near the edges and the center supported the SAR distributions calculated in the breast models. When designing new RF coil at high field MRI, accurate numerical prediction of B_1^+ and SAR is critical to ensure the safety of the patient and to protect the RF hardware. Through this study, we were able to evaluate the performance of a new 8-ch RF array developed for breast MR imaging at 7T. While less efficient in terms of mean $B1^+$ field intensity per supplied RF power due to RF coupling, this RF array shows homogeneous $B1^+$ field distributions in the breast region. Very good agreement between the simulation results and experimental measurements were observed. Future will work will include constructing an identical arrangement for bilateral imaging and combining the proposed Tx array with an Rx-only insert in order to increase SNR in the breast region.

4.0 DEVELOPMENT OF A 7T RF COIL SYSTEM (TRANSMIT AND RECEIVE) FOR BREAST IMAGING

Kim, J., Santini, T., Bae, K. T., Krishnamurthy, N., Zhao, Y., Zhao, T., & Ibrahim, T. S. (2017). Development of a 7 T RF coil system for breast imaging. NMR in biomedicine, 30(1), e3664.

4.1 INTRODUCTION

The major advantage provided by high/ultrahigh field magnetic resonance imaging (MRI) is the increase in signal-to-noise ratio (SNR) which can be used to increase the spatial resolution and/or reduce the acquisition time. However, as the static magnetic field strength increases, obstacles arise such as the B_1^+ field (transverse electromagnetic field responsible for excitation) inhomogeneity caused by the relatively large sample size compared to the short in-tissue wavelength and constructive/destructive electromagnetic (EM) field interference [49].

Overcoming these obstacles to take better advantage of the increases SNR has resulted in the development of multi-channel transmit (Tx)-only array combined with multi-channel receive (Rx)-only array systems [3, 53, 69, 73, 82]. Preliminary studies have shown that B_1^+ field inhomogeneity can be observed even at 3T and this inhomogeneity artifacts can lead to an

inaccuracy of breast evaluation [121, 123, 153]. It has been shown that the B_1^+ field inhomogeneity can be alleviated using RF-shimming techniques [23, 39, 49, 57, 70, 74].

In addition, more SNR can be attained through the use of close-fitting multi-channel Rx-only arrays [3, 55]. In 7T breast MRI [26, 154, 155], B_1^+ field inhomogeneities (typically observed in head and abdominal studies) can be relatively less apparent than due to the 1) smaller size of the breast and 2) lower dielectric constant of breast tissue. Both of these facts lead the breast to have smaller electrical size. That being said, typical 7T Tx coils used for breast MR imaging commonly utilize single or double surface coils that produce B_1^+ fields that decay toward the chest wall with potential penetration issues. This need necessitates the development of new types of Tx breast coil with detailed analysis of their B_1^+ fields and associated SAR.

Breast MRI most likely increases the chance of early detection of breast cancer when the examination is accompanied by regular mammograms [118-120]. In clinical breast MR examination, a gadolinium contrast enhancement technique is commonly used to detect abnormalities of the signal wash-in/-out pattern in the tissue [118, 121, 122]. Homogeneous excitation is required as the technique is based on spatial changes of the signal intensity over the entire breast. High-resolution imaging is also needed for accurate assessment and diagnosis of breast disease. For example, detection of a tumor before its diameter reaches 10 mm is one of the most important factors affecting treatment type and survival rate [123, 124]. T1-weighted fat-suppressed MRI is commonly acquired to differentiate the fibroglandular (FG) tissues from surrounding fat tissues in order to categorize the breast type that is defined by American College of Radiology [122, 125, 126] as patients with dense FG breast tissues result in significant diagnostic challenges using mammogram. For such cases, both high-resolution and homogeneous fat-suppression MRI are required. In addition, fast MRI is preferable as depiction

of fine morphologic details of lesions can be observed only in early post-contrast phase, 60-120 sec [118, 121-123]. Therefore, 7T imaging with its superiority in speed and/or resolution can provide significant advantages for breast applications [30, 38, 127]. All of these characteristics can be improved with a homogenous and multi-receive (enhances speed and SNR) RF breast coil system.

In this study, we have developed an eight channel Tx-only array [35, 71, 111] based on Tic Tac Toe (TTT) design**,** and combined it with an eight channel Rx-only array insert for breast MRI at 7T for higher signal detectability. In order to predict the B_1^+ field distribution and associated specific absorption rate (SAR) in the breast tissues, RF numerical simulations were carried out using finite-difference time-domain (FDTD) method [73]. The generated B_1^+ field by the developed RF coil system was also measured utilizing a breast phantom and in-vivo. SNR and CNR was investigated with and without the Rx array insert at 7T as well as at 3T under similar imaging conditions and utilizing commercial array coil. Finally, the developed RF coil system was applied for in-vivo three-dimensional (3D) high-resolution MRI of human breast.

4.2 MATERIALS AND METHODS

4.2.1 TTT Tx-Only Array and FDTD Modeling

Transmission line elements (16 coaxial solid squared-shaped inner copper rods inserted in 16 outer copper struts) were adapted for an RF transmit coil composed of two planar sides of 2 x 2 TTT elements. An outer copper strut is constructed on a 170 × 170 mm^2 polycarbonate tube and inner copper rod is then inserted inside a hollow squared shaped outer copper strut (Figure 4-1) and then assembled with RF shield box dimensions of 127 × 170 × 170 mm^3 (red dotted lines in Figure 4-1A). Outer copper strut is then connected to the RF excitation center pin and inner rod is electrically connected to the surrounding RF shield (Figure 4-1C). Detuning of the Tx-only array was accomplished by applying voltage through the PIN diode that electrically connects the outer copper strut to inner copper rod during the MR signal reception (Figure 4-1C). Each side has four excitation ports which allow for a total of eight independent RF excitations and each port can be tuned and matched by pushing/pulling the copper rod inserted into the cavity of the copper strut (Figures 4-1A and C). This effectively changes the lengths of the associated transmission lines and therefore the resonant frequency of the RF coil. Scattering (i.e. S11, S12 and S13) matrix was measured using vector network analyzer (HP, USA) at all eight excitation ports. Considering the sample size (relatively small 100 – 130 mm) and lack of real-time specific absorption rate (SAR) monitoring, this study was carried out in a single transmit system utilizing 8-way Wilkinson power divider and constant phase shifters in order to produce a pseudo

circularly polarized (CP) mode. Through different cable lengths, 4-port quadrature excitation on both sides of the transmit array was utilized. Looking into the B_0 direction, the phases of the voltages were rotating clockwise with increments of 90° for one TTT side and counter clockwise for the other TTT side. Although our experiment was performed in a single transmit mode, Tx-only array can be interchangeably used in parallel transmit system (pTx) for RF-shimming purposes.

For the numerical calculations of B_1^+ field and SAR in the breast tissue, an in-house C++ FDTD package that incorporates true transmission line modeling for excitation and reception [47, 49, 62] was utilized. The mesh of a Tx-only array was developed using MATLAB (Mathwork, MA). Identical dimensions of the RF coil was created in the computational domain (grid matrix of 162 × 162 × 168 cells where each cell represents $(1.58\ mm)^3$ of volume). Temporal resolution of $3*10^{-12}$ sec was used to satisfy Courants stability boundary condition and 32 layers of perfectly matched layer were added on each side to prevent the artificial electromagnetic field reflections at the boundaries [46, 72].

A 3D 6-tissue breast model (50 – 75% FG tissue) developed from University of Wisconsin Madison (http://uwcem.ece.wisc.edu/phantomRepository.html) was centered in the coronal plane with respect to the RF coil, and chest wall area was located outside of the RF coil to resemble the experimental environment in-vivo. Electric and B_1^+ fields calculated from exciting each of the 8 Tx elements were linearly superimposed in phase and amplitude. B_1^+ inhomogeneity index (= standard deviation/mean) was calculated in two ROIs; 1st ROI (ROI1) is a tissue volume within the RF coil, and 2nd ROI (ROI2) is entire tissue volume including the chest wall region located outside of the RF coil boundaries. SAR over the entire tissue volume was calculated.

Peak SAR (W/kg) was calculated using the following equation and was determined for 10 gram pixel average:

$$SAR_{(x,y,z)} = \frac{1}{2}\left\{\frac{\sigma_{(x,y,z)}\left(E^2_{x(x,y,z)} + E^2_{y(x,y,z)} + E^2_{z(x,y,z)}\right)}{\rho_{(x,y,z)}}\right\} \quad (4\text{-}1)$$

Where sigma (σ) is the conductivity and rho (ρ) is the density of tissues in the sample. The density of the breast is determined by the tissue composition ratio of fat to connective tissue. x, y, and z represent locations in the Cartesian coordinate system.

4.2.2 Eight-Channel Rx-Only Array

An eight-channel close-fitted Rx-only array was constructed on an acrylic frame that was customized for breast MRI (Figure 4-1B). Four loops were tapered (first panel in Figure 4-1C, blue squares) in an orthogonal direction to B0 (green dotted lines in Figure 4-1B, only two channels are shown), while the other four loops were tapered in a parallel direction to B0 (blue and yellow dotted lines in Figure 4-1B). Four loops were rectangular in shape and measured 80 mm in height and 80–85 mm in width (green dotted lines in Figure 4-1B). Another three loops were set about 30 mm apart to minimize the mutual coupling and the eighth element was a saddle coil tapered at the bottom of the frame in order to increase the signal reception depth (yellow dotted line in Figure 4-1B).

We manually adjusted the overlapping distance (~10mm) to minimize the coupling of the neighboring loops, and additional preamp decoupling was applied to reduce the mutual

inductance of the next neighboring and non-overlapping loops. Each loop used seven capacitors (8–12 pF, Ct in Figure 4-1C) to tune the resonant frequency to 297.2 MHz, and matching capacitors were 64 pF in Cm1 and 12–18 pF in Cm2, respectively (see Figure 4-1C). Each loop consists of two passive detuning circuits and one active detuning circuit that allows the Rx-only array to appear as an open circuit during the transmission period (see blue dotted circle and PIN diode in Figure 4-1C). Reflection and transmission coefficients (S11, S12) were measured using a vector network analyzer (HP).

To accurately evaluate the decoupling between the Rx elements during the MRI experiment, the noise correlation matrix was measured with the RF amplifier disabled [38, 83, 156]. In addition, we used the sum-of-squares method to combine individual Rx channel signal information.

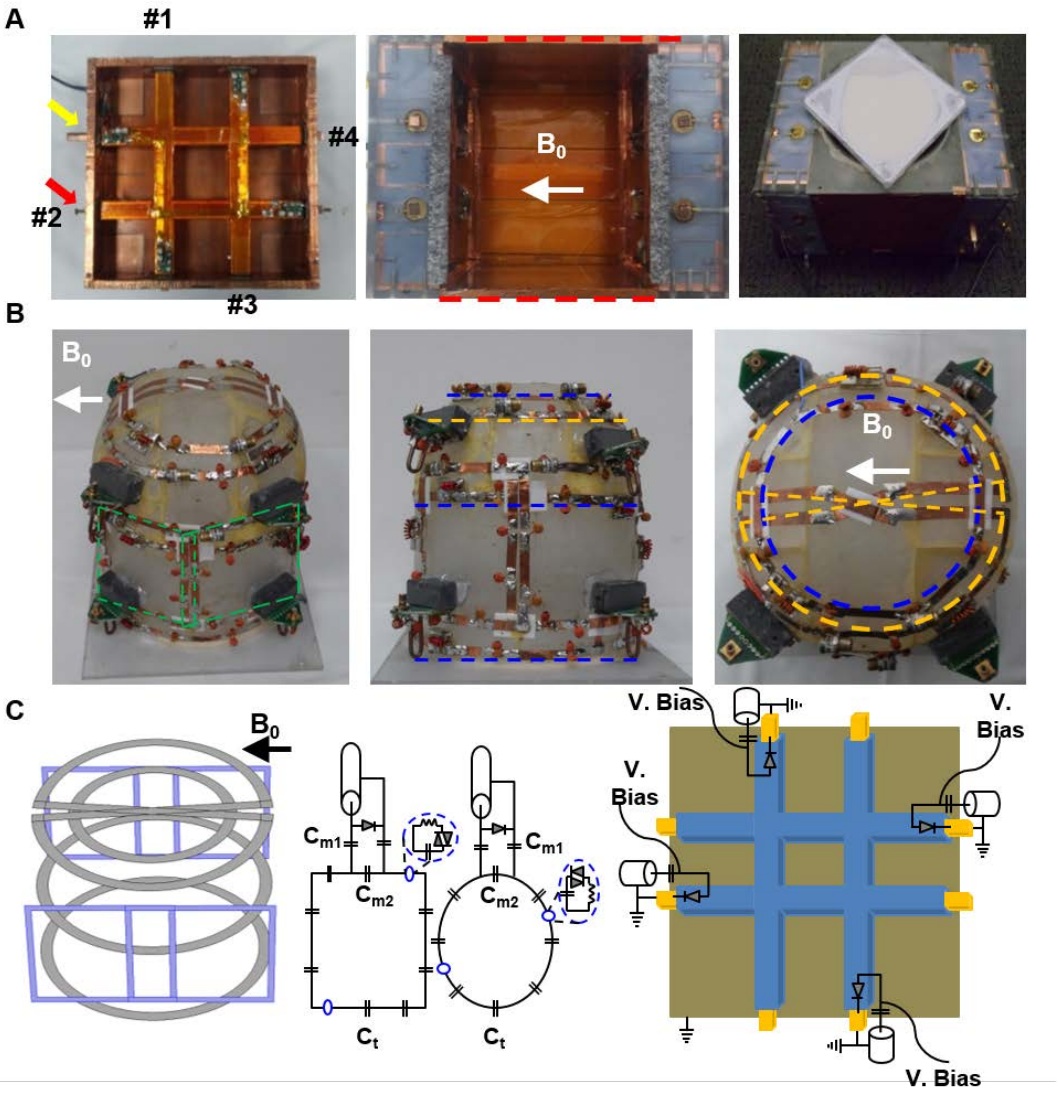

Figure 4-1 8-ch Tx-only array, 8-ch Rx-only array and breast phantom. (A) One side of 2-by-2 TTT array showing four excitation ports (red arrow and numbered) with tuning rod (yellow arrow) and assembled Tx-only array with RF shield box (red dotted lines). Tuning and matching can be achieved by pushing/pulling the inner copper rods; it is done once on the phantom and applied for all the human studies. (Panel A, right) Complete assembly of the 8-ch Tx-only and 8-ch Rx-only array and breast phantom located at the top of the RF coil. (B) Picture of 8-ch Rx-only array in three planes. Four loops were tapered orthogonal to B_0, two are showing (green dotted box) and two are tapered on the opposite side of the frame. Additional four loops were tapered in coronal plane, three loops (blue dotted lines) are located 35mm apart and a saddle loop (yellow dotted line) was located at the bottom. (C) Schematic diagram of Rx-only and Tx-only arrays. First panel shows 3D layout of the 8 Rx-only array that tapered in the acrylic frame (first panel in B). Second and third panels show circuit diagram of Rx-only array. Capacitors used in the coil loop for resonance frequency tuning (C_t) varied between 8-12pF, whereas capacitors used for 50 ohm matching was 64 pF at C_{m1} and 12-18 pF at C_{m2}. Fourth panel shows Tx-only pin connections and the detuning circuits used for active detuning during signal reception.

4.2.3 Imaging Studies

The study followed our institutional Internal Review Board. Five normal female healthy volunteers (33 – 40 years old) were recruited and scanned. All MR imaging studies were performed on a 7T human scanner (Magnetom: Siemens Medical Systems, Erlangen, Germany), and one of the subjects underwent 3T (Trio2: Siemens Medical Systems, Erlangen, Germany) imaging for SNR comparison using body coil as a Tx and vendor 2-ch array breast coil as Rx.

7T Gradient recalled echo (GRE) sequence with fat suppression at varying flip angles (FA) (10^o – 90^o with 8 steps) was used to measure the B_1^+ field in MRI using the breast phantom (i.e., 50% glandular and 50% adipose tissue along with 8 – 10 cystic masses, volume of 500 cc with dimension of 120 × 100 × 90 mm^3) and in vivo. In the breast phantom, chest wall was not present thus the B_1^+ field distribution was measured in entire phantom volume. For the in vivo study, B_1^+ field was measured at 2 ROIs; 1^{st} ROI is tissue region within the RF coil, and 2^{nd} ROI is entire volume including the chest wall area located outside of the RF coil enclosure. We applied fat-suppression RF pulse during B_1^+ mapping acquisition since homogeneity in the FG tissue region is our primary target. Mean intensity in the fat tissue as a threshold value was measured, and the mean B_1^+ field distribution was measured only in the threshold non-fat tissue region.

To evaluate the feasibility of parallel MR imaging, geometry (G) factor maps were acquired in the spherical phantom. Acceleration factor (R) from 1-4 was applied with 3D gradient echo in anterior-posterior (AP) direction in the sagittal and transverse planes and in the head-feet (HF) direction in the coronal plane. Imaging parameters are: TR/TE = 4/2 msec, FA = 10^o, in-plane resolution = 1.25 × 1.25 mm^2 and slice thickness = 1.25 mm. Relatively small in-

plane FOV (160mm*160mm) was used for G-map acquisition due to the high background noise. We purposely did not mask background of the G-maps to show relative noise increase in the background. G-map was calculated using the following equation:

$$G - Map_{(x,y,z)} = \frac{SNR_{(x,y,z)R=1}}{\sqrt{R}*SNR_{(x,y,z)(R=1,2,3,4)}} \quad (4\text{-}2)$$

Where $SNR_{(x,y,z)}$ is the SNR map of the MR images; and x, y, and z represent locations in the Cartesian coordinate system.

7T 3D dual echo steady state (DESS) sequence was used to compare SNR with and without the Rx-only array in the breast phantom; TR/TE = 30/5 msec, FA = 25°, in-plane resolution = 0.8 × 0.8 mm^2 and slice thickness = 0.8 mm.

For the SNR calculation, four squared regions in the coronal plane were selected to calculate the standard deviation of the noise (white dotted boxes in Figure 4-5A) and SNR was then calculated by dividing the image intensity, pixel by pixel, to the noise. In addition, contrast-noise-ratio (CNR) was calculated between the fibroglandular and fat tissues in order to measure the image quality. Equations used for the SNR and CNR calculation are:

$$SNR = \frac{SI_{(x,y,z)}}{Noise} \quad (4\text{-}3)$$

$$CNR = \frac{SNR_{(FG)} - SNR_{(f)}}{SNR_{(FG)} + SNR_{(f)}} \quad (4\text{-}4)$$

where SI is the signal intensity, noise is standard deviation calculated from four corner ROIs, FG is fibroglandular and f is fat tissue in the breast. x, y, and z are the pixel locations in the MR images.

In-vivo 3D T1-weighted breast images were acquired at isotropic resolution (0.6 mm) using GRE sequence with fat-saturation at 7T (with and without Rx-only array) and at 3T. SNRs

were then compared; TR/TE = 21/2.8 msec, FA = 25^{o}, field of view (FOV) = 150 × 150 mm^{2}, matrix = 256 × 256, slice thickness = 0.6 mm and total scan time = 7:40 min.

4.3 RESULTS

4.3.1 B_1^+ Field Distribution and SAR

About 20% B_1^+ field inhomogeneity was calculated using the FDTD numerical simulations in the breast model in ROI1, whereas inhomogeneity increased to 28% in ROI2 (Figure 4-2B). B_1^+ field inhomogeneity experimentally measured in the entire volume of the breast phantom was ~27% (Figure 4-2C). Note that B_1^+ inhomogeneity measured in the breast phantom was relatively higher than that compared to the FDTD numerical model, mainly because of the artificially void/inflated B_1^+ field values in the solid masses (see red arrow heads in Figure 4-2C). In-vivo B_1^+ field inhomogeneity in the ROI1 was ~22% and increased to ~31% when the chest wall was included (Figure 4-2D). Mean FA FDTD-calculated in the breast model was ~75^o (degree/ total input of 100 V) and ~70^o was measured in the breast phantom whereas ~60^o was measured in vivo.

Breast model peak/average SAR calculated per a continuous mean B_1^+ field of 2uT within ROI1 was 2.61/0.39 Watt/Kg/10g tissue whereas 3.64/0.57 was calculated per a continuous mean B_1^+ field of 2uT within ROI2 (Figure 4-2A). Peak SAR at ROI1 and ROI2 was calculated at the periphery of the breast model where skin and chest wall were located. Volume of the breast model that was located outside of the RF coil (included in ROI2) was mostly composed of muscle tissues, thus the average/peak SAR at ROI2 increased.

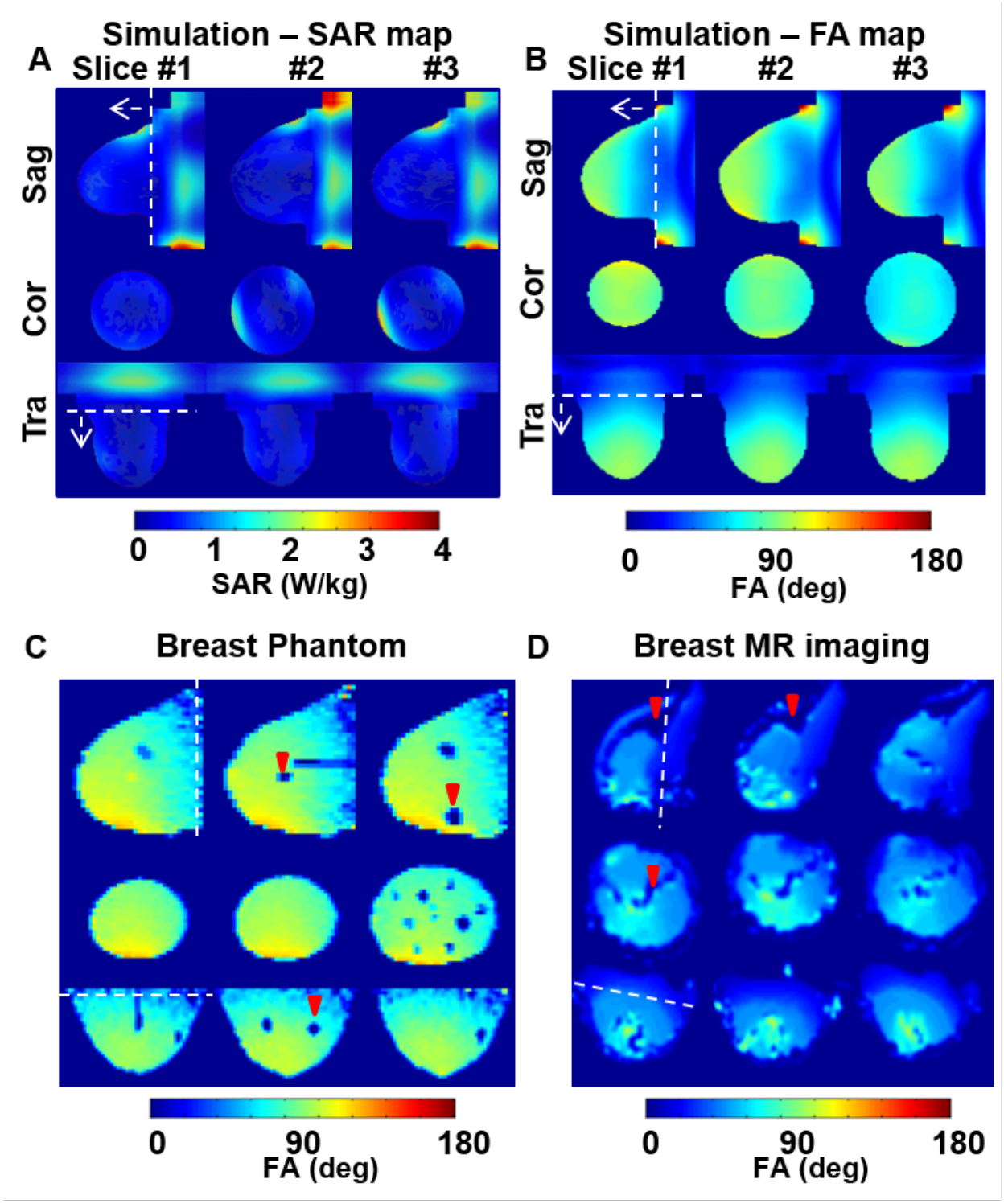
A
Simulation – SAR map
Slice #1
#2
#3
Sag
Cor
Tra
0
1
2
3
4
SAR (W/kg)
B
Simulation – FA map
Slice #1
#2
#3
Sag
Cor
Tra
0
90
180
FA (deg)
C
Breast Phantom
0
90
180
FA (deg)
D
Breast MR imaging
0
90
180
FA (deg)

Figure 4-2 FDTD-Calculations of SAR and B_1^+ field distributions in the breast model and MRI measurements of B_1^+ field distributions in breast phantom and in vivo. (A) SAR map calculated in the breast model shows peak SAR near the periphery of the breast where high conductivity tissues (muscle and skin) are located and relatively high SAR was observed in the chest wall area where the muscle is primary tissue. (B) 3D anatomically detailed breast model shows ~20% inhomogeneity within in the RF coil volume where ROI1 was from the white dotted line and arrow direction. ROI2 was set for the entire volume and inhomogeneity of ~28% was calculated. (C) B_1^+ field distribution experimentally-measured for breast phantom at 7T; cyst-like solid masses (red arrow heads) present artificial voids. (D) In vivo B_1^+ map. Fat tissues were excluded (red arrow heads) and B_1^+ field inhomogeneity was measured at same ROIs that were set for the simulations. ~22% was measured at ROI1 and ~31% was measured at ROI2. Note that white dotted line represents the coil end.

4.3.2 Coupling Matrix and Noise Correlation

In the 8-ch Tx-only array, mean S11 (reflection coefficient) of ~-24 dB was measured whereas S12, S13 (transmission coefficient) of -8dB, -3dB were measured. Design of the Tx-only array necessitates high coupling between opposite elements (i.e. S13) as can be seen in the S matrix shown in first column of Figure 4-3.

Noise correlation matrix measured in the 8-ch Rx-only array shows minimal interaction (3%) between the Rx elements implying that good decoupling (overlapping and preamplifier) was achieved (second column in Figure 4-3). In addition, the measured mean S11 and S12 in all eight Rx loops were ~-20dB and ~-15dB, respectively.

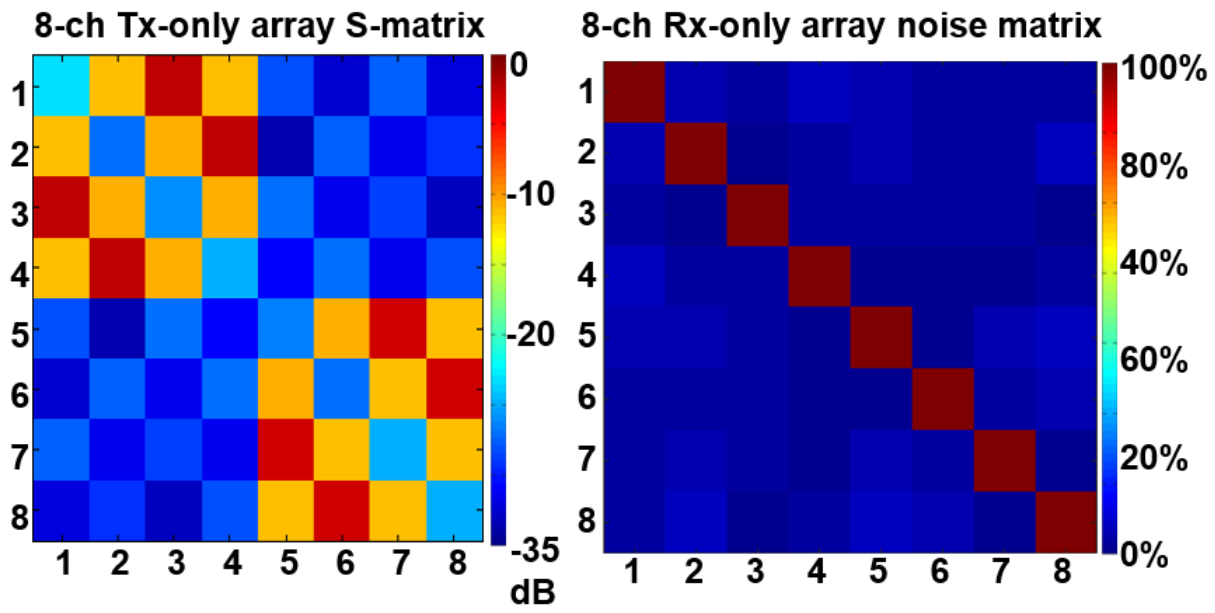

Figure 4-3 Tx-only array scattering (S) matrix and Rx-only array noise correlation matrix. (Left) Mean reflection coefficient (S11) of ~-24dB was measured for 8 excitation ports and transmission coefficients (S12, S13) of ~-8 and ~-3 dB were measured using vector network analyzer. (Right) The mean noise correlation between the Rx channels were ~4±3% was measured in all Rx elements.

4.3.3 G-Factor Map Acquisition

The mean G factor increased in all three planes as R increased, and the mean G factor calculated at R = 2, 3, and 4 in sagittal/coronal/transverse planes was 1.06/1.03/1.01, 1.21/1.17/1.13, and 1.52/1.55/1.36, respectively. The peak G factor was measured at R = 4 in each plane (sagittal/coronal/transverse) and was 2.8/2.3/2.7 (Figure 4-4).

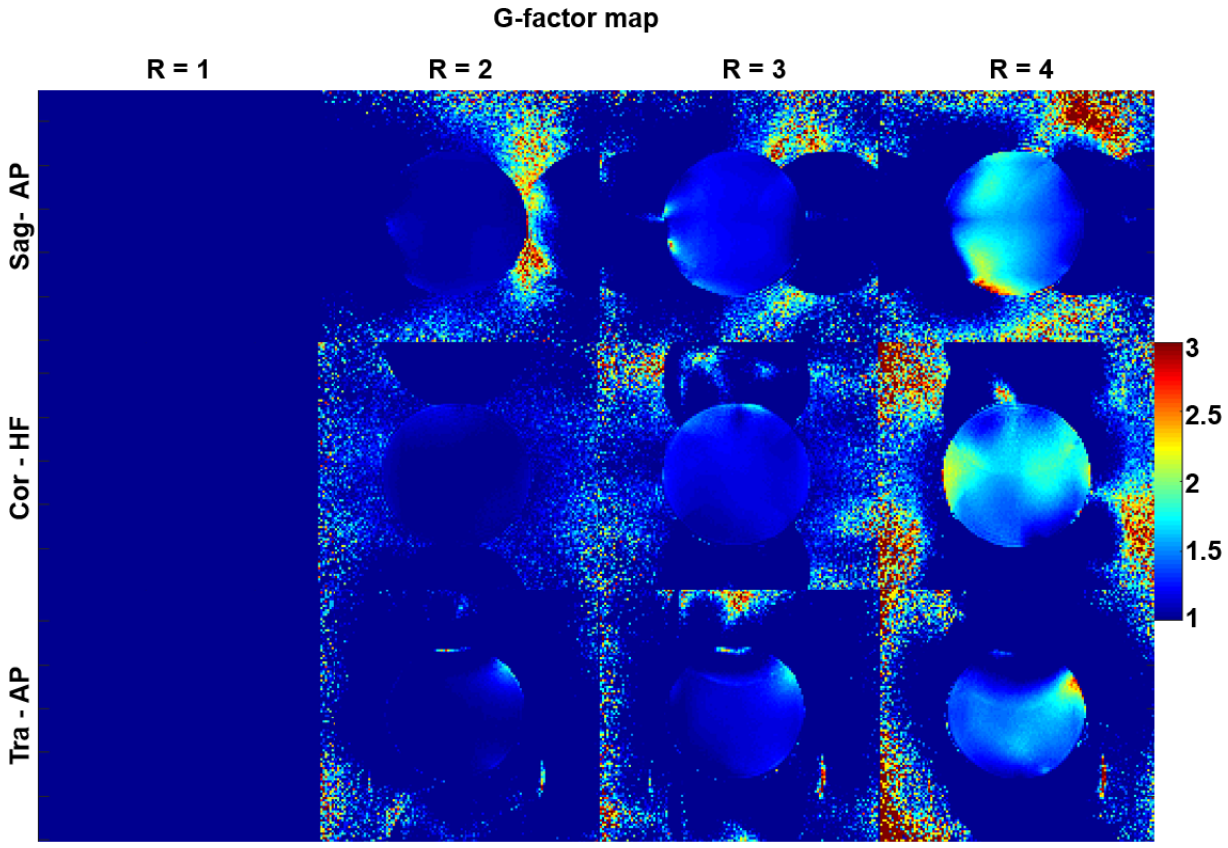

Figure 4-4 Measured G-factor map in three planes. The maps were calculated using 3D gradient echo sequence with varying acceleration (R) factor from R=1-4 in AP direction for sagittal and transverse plane and HF direction in coronal plane.

4.3.4 SNR/CNR Comparison: 3T Versus 7T MRI

Figure 4-5A and B shows SNR maps of in vivo breast MR images at 0.6 mm isotropic resolution at 3 T and 7 T, respectively. The SNR measured in the FG tissue region was about four times higher at 7 T (~50 versus ~200, as shown in Figure 4-5C). CNR measured with fat and FG tissues increased about twofold at 7 T (~0.35 versus 0.63, as shown in Figure 4-5C). The increased SNR at 7 T in conjunction with the developed RF breast coil system provides clear differentiation of the FG from fat (see Figure 4-5B).

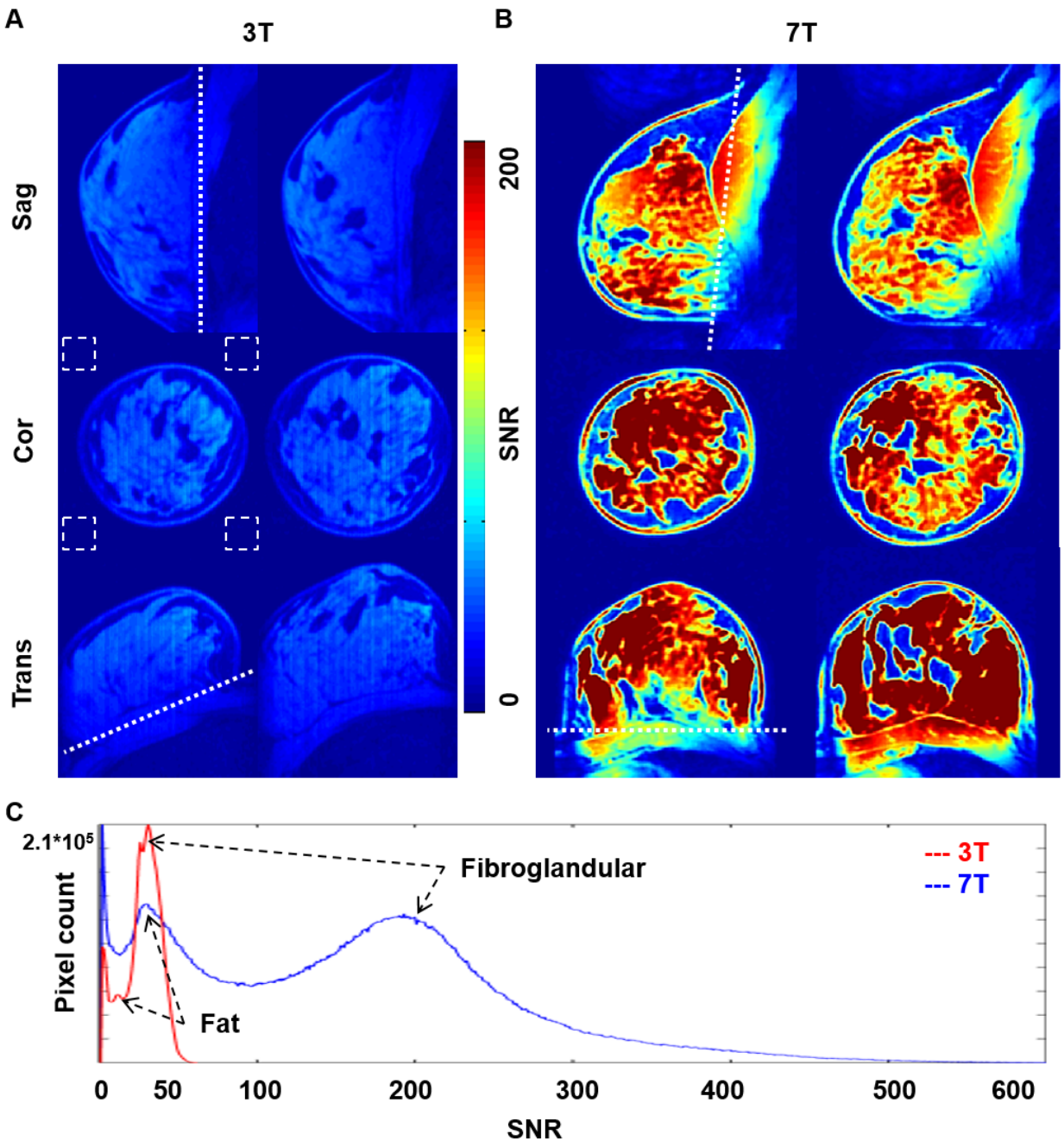

Figure 4-5 SNR comparison at 3T (A) vs. 7T (B) in vivo breast MRI. (A) ~ 50 SNR was measured in the FG tissue regions. (B) Mean of ~4 fold of SNR increase was measured with clear delineation of FG tissues from fat. (C) Quantitative SNR distribution at 3T and 7T. Two peaks indicate FG and fat tissues and SNR contrast of ~4 was measured at 7T whereas ~2 was measured at 3T, respectively. Note, the background noise was calculated in the four corners of the coronal images (white dotted boxes) due to the respiratory motion artifact in the sagittal planes.

4.3.5 SNR Comparison: With Versus Without Rx-Only Array

When the Tx-only array was used for Tx/Rx (i.e. transceiver array without Rx-only set-up), SNR decay toward the chest wall was observed, as shown in Figure 4-6A. With the Rx-only array set-up, an SNR increase of about threefold was measured (Figure 4-6C). Significant increase of SNR was measured at the phantom periphery and toward the chest wall area due to the increased Rx sensitivity (white dotted contours in Figure 4-6A and B). As a result of combining the eight-channel Rx-only array with the Tx-only array, significant improvement in the SNR was achieved (Figure 4-6).

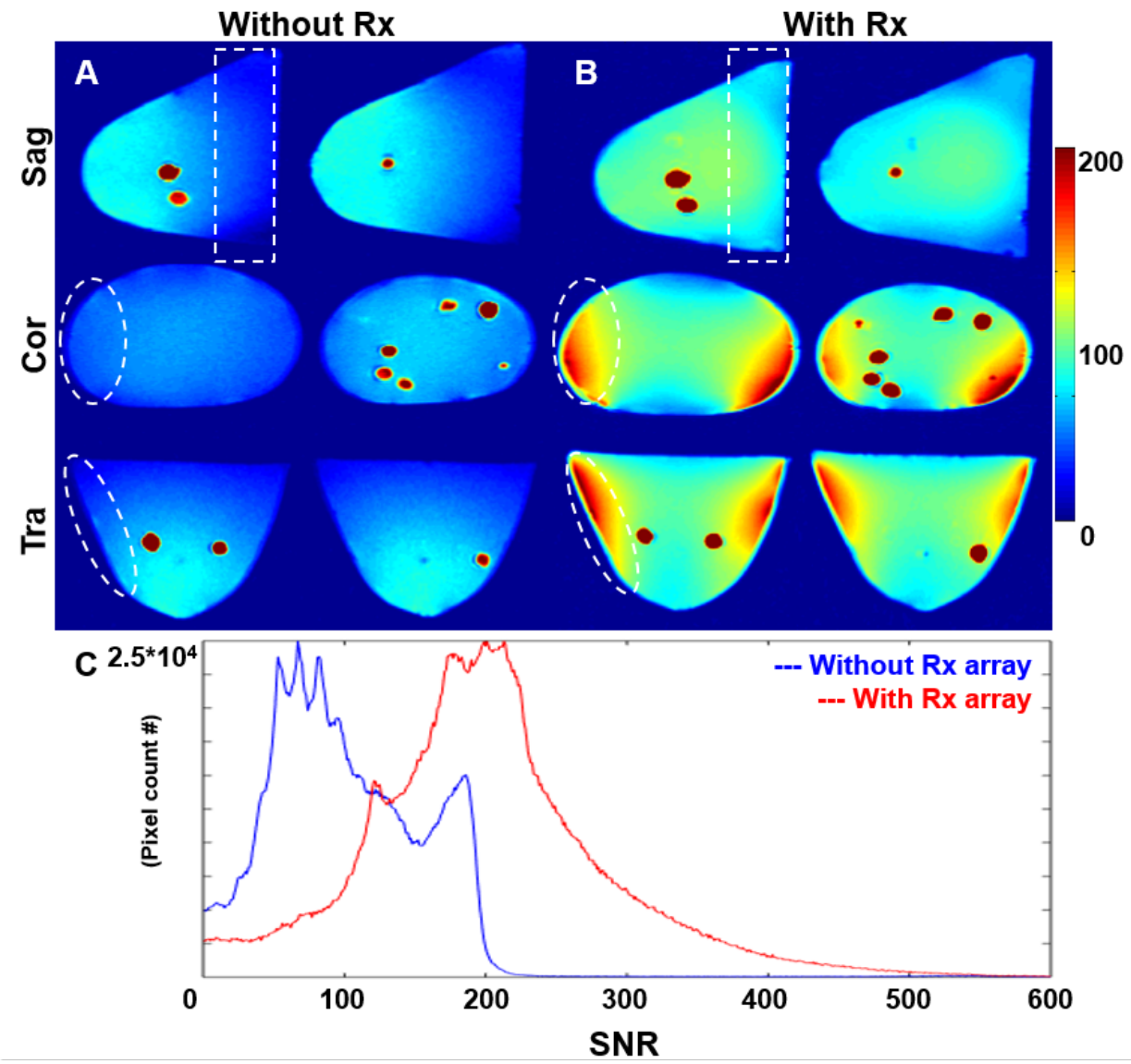

Figure 4-6 SNR evaluation with and without Rx-only array at 7T using breast phantom. (A) SNR map of breast phantom without Rx-only array. Noise voltage was high due to the increased volume of reception and SNR was ~80 (Tx-only array was used as Tx/Rx). (B) Tx-only array combined with Rx-only array shows significant increase of SNR at the phantom periphery and toward the coil end successfully reducing the noise voltage (white dotted circle and box). (C) SNR distribution measured in the breast phantom. Without Rx-only array, mean SNR of ~80 was measured, however, when Tx-only array was combined with Rx-only array set-up, SNR of the phantom increased to ~200. Breast phantom does not have different tissues thus differentiating fat and FG was not feasible.

4.3.6 In-Vivo MRI

High-resolution breast MR images with 3D T1-weighted fat-suppression at 0.6 mm isotropic resolution were acquired, with clear demarcation of the FG tissues from surrounding fat tissues and chest wall (see white arrows in Figure 4-7) when the Tx-only array and Rx-only array were combined (Figure 4-7B). The breast RF coil system composed of the eight-channel Tx-only TTT array combined with the close-fitted eight-channel Rx-only array demonstrates homogenous and high-SNR breast MRI at 7 T. Figure 4-8 shows high-resolution (0.6 mm^3) in vivo breast MRI of four subjects (one subject was involved during the sequence parameter optimization and the image quality was not appropriate to evaluate.) Fat suppression was homogeneously applied and an SNR difference of about fourfold was measured between FG tissues and fat tissues (Figure 4-8C). Subject 1 had the smallest breast size and the pixel count in the entire breast volume was the smallest. SNR distributions in all four subjects were similar, with the background peak observed at about 10–15. The mean SNR for FG tissue was about 220, whereas that of suppressed fat tissue was about 50.

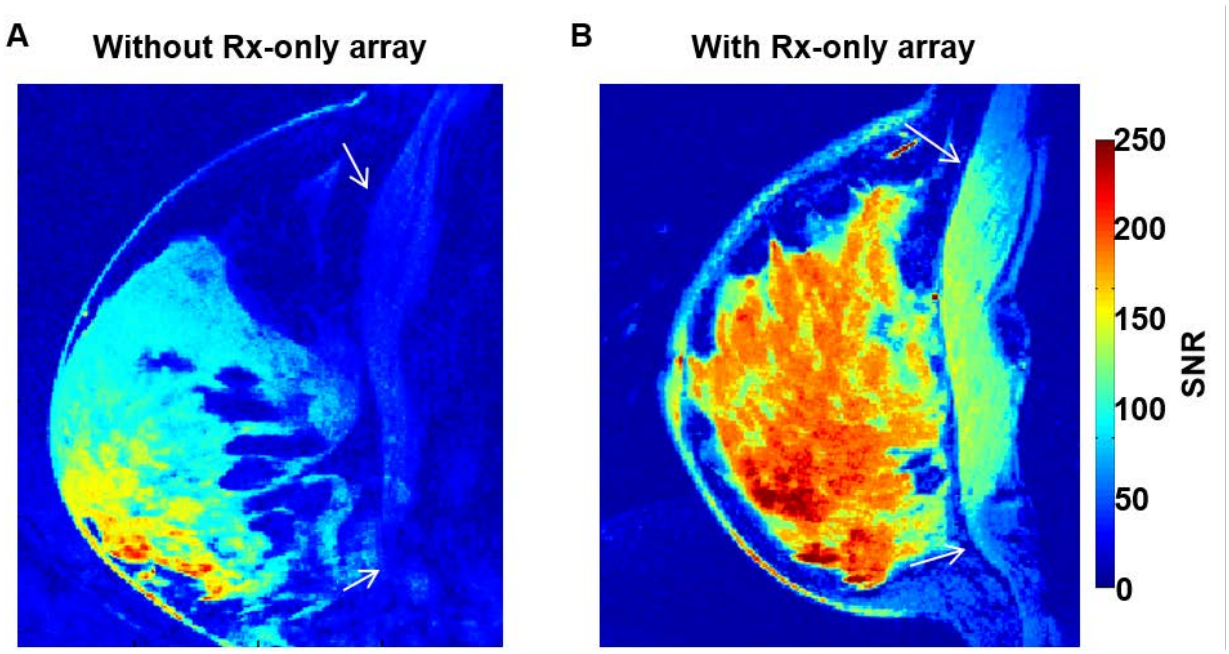

Figure 4-7 In vivo 7T SNR comparison of with/without Rx-only array. With Rx-only array set-up (right) shows SNR increase of ~2.5 and homogeneous receive sensitivity in the breast region. Clear differentiation of breast tissues from the chest wall (white arrows) was achievable with Rx-only array

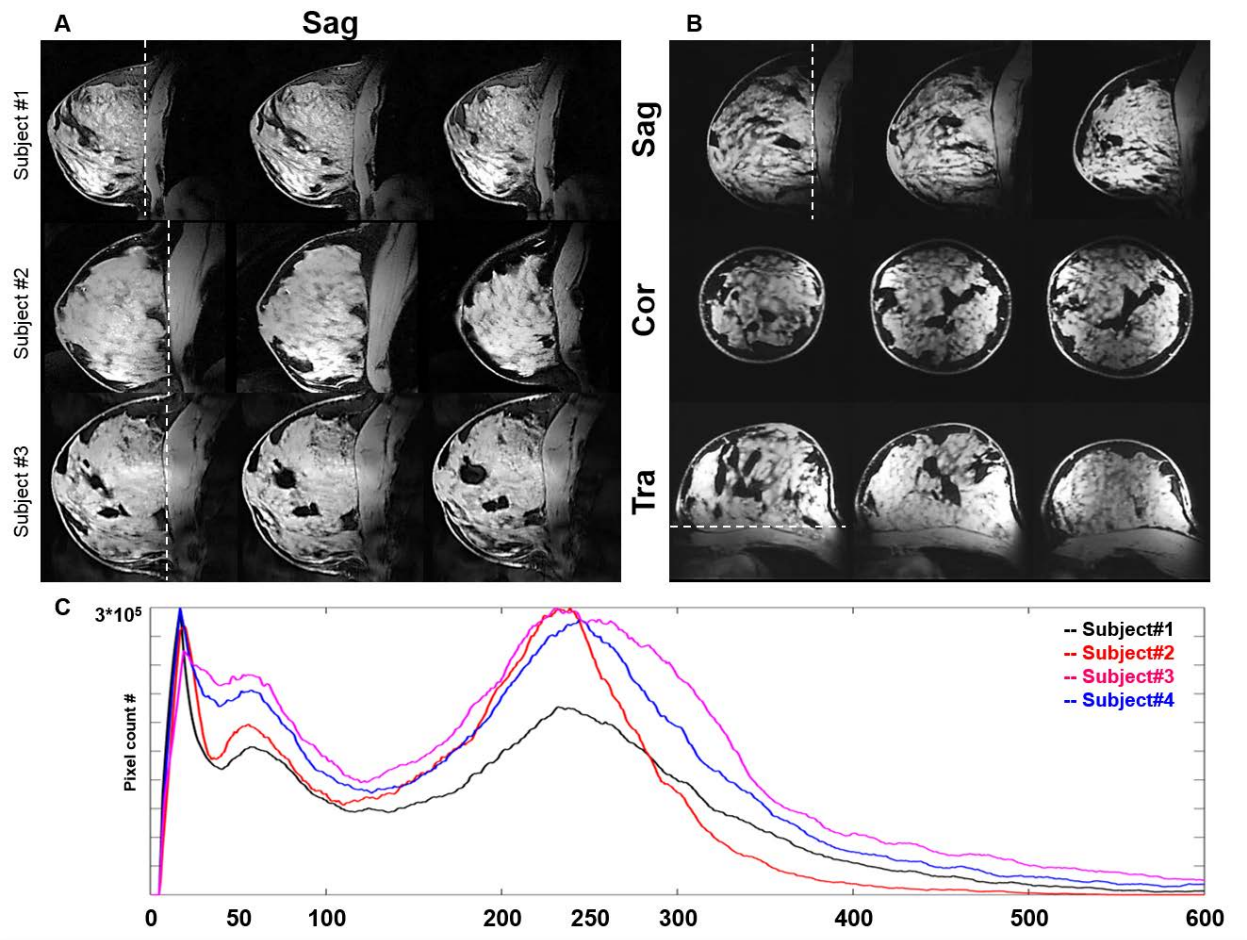

Figure 4-8 In vivo 7T 0.6 mm^3 isotropic T1W with fat-suppression MR images. (A) Sagittal view of breast MRI for three different subjects showing high SNR/contrast between the FG and fat tissues. (B) Breast MR images of one subject showing in three different planes: sagittal, coronal and transverse. (C) SNR distribution from four subjects showing good inter-subject reproducibility with ~4 fold of SNR difference between FG tissues and fat tissues.

4.4 DISCUSSIONS AND CONCLUSION

A new Tx-only and Rx-only array RF coil system for breast MRI at 7T was developed. Although breast model, experimental phantom, and in-vivo were not identical in terms of tissue composition, dimensions and geometry, B_1^+ field variation and distribution were relatively at a good agreement and showed reasonable B_1^+ homogeneity in the breast and improved SNR compared to 3T. Due to the unique experimental setting for the breast MRI where the breast tissues are pulled by gravity for separation of breast tissues from the chest wall, chest wall is located outside of the Tx-only array sweet spot and decay of the B_1^+ field is expected. Combination of the Tx-only array with close-fitting Rx-only array successfully gains receive sensitivity (although with some decrease in the B_1^- homogeneity) in the low B_1^+ area. Peak SAR was calculated in the periphery of the breast tissues due to the presence of high conductivity tissues (skin and muscle) (Figure 4-2A) and relatively high SAR was calculated in the chest wall region where muscle tissues are located.

In-vivo breast MR imaging acquired at 3T and 7T were qualitatively compared by an experienced breast radiologist with over 20 years of experience and confirmed that compared to 3T, 7T showed 1) still homogeneous fat-suppression, 2) higher SNR, and 3) clearer differentiation of the chest wall from the breast tissues with sufficient SNR. While SNR increased ~4 times at 7T, CNR (contrast to noise ratio) also increased. Figure 4-5C shows that CNR (FG/fat) of ~2 (~46/22) was measured at 3T whereas ~4 (~200/44) was measured at 7T, respectively. Moreover, SNR distribution between the subjects shown in Figure 4-8C demonstrated reproducibility of the developed RF array coil. In addition to SNR, quantitative CNR measurements demonstrate that breast MRI at 7T provides high contrast between two

major tissues in the breast. Measured noise matrix showed good isolations between the Rx-only array channels and acquired G-factor map showed feasibility of parallel imaging with the developed RF array system. However, with the limited number of Rx-only array channels, acceleration (R)-factor higher than R=3 is not desired with our RF array. High-resolution 3D MRI of breast in vivo using the developed RF array system at 7T detailed the anatomical structures in the breast.

Our study shows SNR of ~220 in FG tissues and ~50 for the fat tissues with fat-suppression applied in T1 weighted MR images whereas, Korteweg et al show relatively mean SNR of ~150 in the center of breast at 7T [20]. Total acquisition time and sequence parameters are different and it is not directly comparable since the SNR measurement was performed in the proton density map. Brown et al demonstrated advantage of the breast MRI in 7T compare to 3T and claimed that 5 fold SNR increase [26] was observed while our study shows ~4 folds of SNR increase. Also that same study [26] reports that ~27% of inhomogeneity is measured in the fibroglandular tissue regions only whereas our study show ~22% of inhomogeneity within the entire breast tissues and ~30% when chest wall is included. That being said, it is quite intricate most especially for breast imaging to directly compare SNR increase and homogeneity variation between different studies.

In this study, we have developed an RF array system with an eight channel Tx-only TTT array combined with an eight-channel Rx-only array for breast MRI at 7T. B_1^+ field distributions (FDTD calculated from anatomically detailed human breast model and measured in a breast phantom and in vivo) were in reasonable agreement. While the RF coils utilized were different at 3 T and 7 T, in vivo measured SNR of breast MRI at 7 T increases by about fourfold compared with 3 T and by about threefold with the Rx-only array utilized compared with the Tx-only coil

utilized as a transceiver. 3D T1-weighted fat suppression in in vivo breast MRI was successfully acquired with high isotropic spatial resolution of 0.6 mm.

5.0 RF ARRAY DEVELOPMENT FOR EXTREMITY (KNEE AND FOOT) MR IMAGING AT 7T; PART 1. TWO WAY–SPLIT RF ARRAY DEVELOPMENT FOR KNEE MAGNETIC RESONANCE IMAGING AT 7T

5.1 INTRODUCTION

Four to Eight receive (Rx) -only arrays combined with a body transmit (Tx) or volume Tx coil are commonly used for knee and extremity imaging in clinically available MRI (1.5T or 3T) nowadays [157-161]. A birdcage Tx/Rx volume coil is not recommended because the coil receives the NMR signal from the entire volume and, therefore, the MR image suffers from low Signal-to-Noise ratio (SNR) [101, 162-165].

In Ultra-High Field (UHF) MRI (≥7T) systems, because the body Tx/Rx coil is not available for most of these systems, it is essential to develop a Radiofrequency (RF) coil that is responsible for spin excitation, that is, a Tx coil with a uniform transmit field (B_1^+) and reception of the MR signal and an Rx coil with a high SNR [45, 78]. It is generally accepted that B_1^+ homogeneity increases as the RF Tx coil volume/size becomes larger [78]. However, the SNR decreases as the size of the coil becomes larger since the noise collected is proportional to the size of the surface coil or the coil volume. Conversely, the SNR improves as the size of the coil becomes smaller and the coil and object become closer in proximity [78]. Consequently, nowadays, it is perceived as a best choice in UHF MRI studies to build a volume or transmit

array coil for excitation and multiple surface Rx coils for MR signal detection [6, 21, 40, 83, 106]. The increased SNR can be used to acquire high spatial resolution knee MR imaging since measuring the thickness of the cartilage, typically 1-4mm, is one of the most powerful diagnostic criteria for osteoarthritis (OA) assessment [5, 27, 128, 129, 131]. In RF developments relating to 7T knee MRI, the issue of B_1^+ inhomogeneity caused by the wavelength of the RF (~13cm) being comparable to or shorter than the size of the object (as in the brain and torso) is often less apparent due to the knee's smaller volume. When designing an RF coil for knee imaging, an RF coil that can be split for patient accessibility is preferred. This is done in most of the commercially available RF coil products and in some of those at research institutions; however, it requires additional time consuming works in terms of the framing construction, creating a highly stable electromagnetic connection between the joint of the split, and enabling distance-controlled inductive decoupling for RF coil tuning. Previous work by Hetherington et al. [166] and Vaughan et al. [59, 96] demonstrates split TEM Tx/Rx coils and provides a more detailed analysis. While many split coils do exist, to the best of our knowledge, the construction of a TEM 2 way-split Tx-only coil combined with a 2 way-split eight-channel Rx-only array has not been reported.

In this study, we developed a 2 way-split RF system for knee MR imaging at 7T, including a TEM Tx-only volume coil that allows quadrature RF excitation and a close-fitting eight-channel Rx-only array. We first measured the reflection/transmission coefficients (S11/S12) of the developed RF array using a network analyzer. B_1^+distribution was numerically calculated using the FDTD method and then compared with experimental results from knee in vivo MR imaging previously acquired from 3 subjects. SAR was calculated in the numerical knee model and was monitored during the scan by a built-in vendor SAR monitoring system. The

SNR increase due to the insertion of the eight channel Rx-only array was quantitatively analyzed by comparing phantom MR images with and without the Rx-only configuration. Also, to provide a reference to clinically acceptable image quality, an SNR map of the knee was measured at 7T and compared to that at 3T using a clinical sequence (using a commercial vendor built 8-channel receive only knee coil) and the body coil as a transmitter. Finally, a high spatial resolution of in-vivo knee MR imaging was acquired.

5.2 MATERIALS AND METHODS

5.2.1 TEM Tx-Only Array Design and Performance Evaluation

A TEM Tx-only array was built on a cylindrical former that could be divided into two pieces (Figure 5-1A and B). A copper sheet (thickness of 8μm) was tapered on the inside of the outer diameter of the cylindrical former as an RF shield and 16-coaxial transmission line elements that had a copper layer were tapered to the outer diameter of a hollow Teflon insert (Figure 5-1D) as described in Vaughan et al [94]. The measured dimensions of each element were length = 200mm, outer diameter = 15mm, inner diameter = 5mm. Each TEM element was radially and evenly located at $\pi/8$ (rads) apart (Figure 5-1C and D). To ensure the stable connection of the RF shielding, two mesh coppers were put in the split-joint of the coil (see yellow dotted box in Figure 5-1A and B) that could be pressed by clips located at each side of the split, thereby providing stable connection. The length of the coil was 210mm, the diameter of the RF shield was 270mm, and the diameter of the element center-to-center was 210mm (Figure

5-1D). To enable the TEM RF coil to be utilized as a Tx-only array, active detuning circuits were inserted between the outer copper layer of the Teflon strut and the RF shield (see the single element in Figure 5-1D). During the RF transmission, reverse bias was applied to the PIN diodes such that each element was operating to produce CP mode excitation; forward bias applied during the Rx period made the elements short-circuit to the RF shield. Coil performance was first measured using a network analyzer (Hewlett-Packard, Palo Alto, CA, USA) to ensure 1) the resonant frequency of the coil circuit matched the center frequency of the 7T, ~ 300MHz, and 2) the isolation of each excitation port was sufficient (better than -10dB).

5.2.2 Eight-Channel Rx-Only Array Design and Tuning Evaluation

An eight-channel Rx-only array was constructed on an acrylic frame. Four loops were tapered onto the one side of the split and the rest were tapered on the other side of the split (Figure 5-1A, B and E). Each of the surface loop coils has a total of 10 capacitor insert sites: 4 used for passive trap circuits (hand wound inductor and 5.6 pF connected in parallel with switch PIN diode inserted between these components, blue circle in Figure 5-1E); 4 provided fixed capacitance (6.8 pF); 1 used for tuning, using a variable capacitor, and 1 for impedance matching (varied between 33 – 68 pF) at the 7T resonance frequency. A schematic diagram of the coil loop array is shown in Figure 5-1E. Each of the loop coils were overlapped at certain distances (varied ~8mm-14mm) to effectively cancel the mutual inductance, thereby providing one single reflection peak at 300 MHz For the one side of 4 coil loops that were tapered at the split joints, an inductive decoupling method (see yellow dotted circles in Figure 5-1 A and B) was applied instead of the overlap distance controlled decoupling method. The pre-amp decoupling method

was applied to effectively eliminate the coupling between non-neighboring loops. The Reflection/Transmission coefficient (S11/S12) was measured between neighboring loops to evaluate coil tuning and matching as well as isolations between the Rx array elements. The dimensions of each surface coil loop are shown in Figure 5-1E.

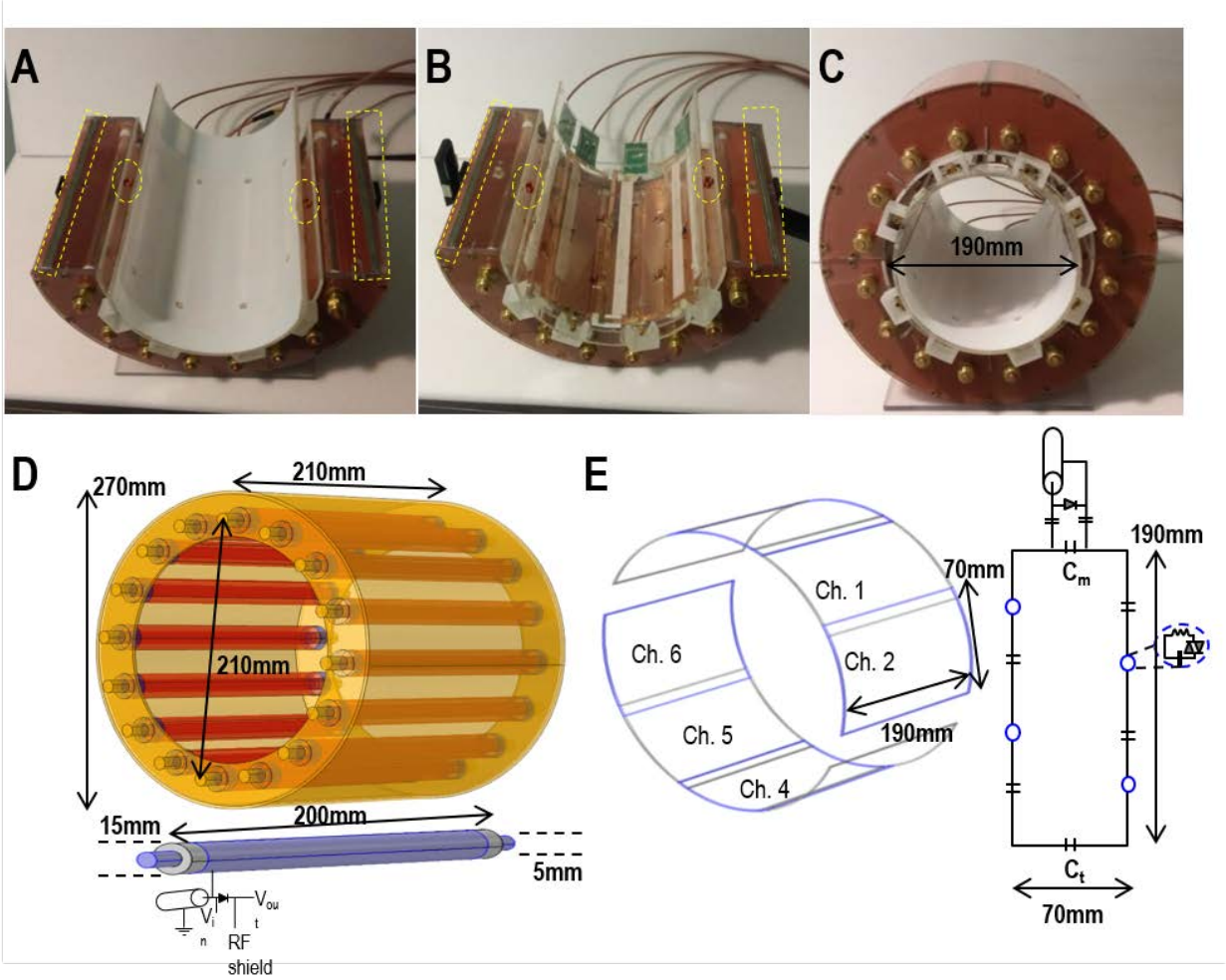

Figure 5-1 Picture of 2-way split TEM Tx-only array and 8-channel Rx-only array and schematic diagram. (A) and (B) Picture of two-way split TEM Tx-only and Rx-only array. Yellow dotted box show copper mesh used at split joints for RF shield connection and yellow dotted circle show inductive decoupling used for four Rx-only array at the split joints. (C) complete assembly of knee RF coil with 190mm inner clearance. (D) schematic diagram of TEM coil and one excitation element with detailed dimensions. Red color represents copper tapered in outer diameter of Teflon strut and orange color represents the RF shield and copper rod inserted in the hollow cavity of the Teflon whereas dark blue color between the RF shield and excitation (between red and orange color) indicate Teflon used for dielectric substance. For the individual excitation element, blue color

indicates the copper layer and rod. Rod can be pushed-in/pulled-out for tuning and matching. (E) Eight Rx-only array loop dimensions and circuit layout. Each Rx array was tuned using variable capacitor at (C_t) and impedance matching was achieved by changing capacitance at (C_m). Blue circles show location of passive detuning circuits and components.

5.2.3 FDTD Simulation and Knee Model

For the numerical analysis involving the B_1^+ evaluation and SAR calculation, a three-dimensional (3D) 16-element TEM geometry was created in a computation domain using MATLAB (Mathworks, MA) and associated conductivity and dielectric constants were assigned (Figure 5-2 and Table 5-1). To meet the Courants stability condition, a grid matrix of 251*251*291 cells (voxel resolution = 1.1x1.1x1.1mm^3) and temporal resolution of $3*10^{-12}$ s was used. To eliminate the EM field reflection at the boundary of the outer grid domain to accurately reflect the experimental condition, 32 Perfectly Matched Layer (PML) was used[150]. The knee model (144*139*191, voxel resolution = 1.1x1.1x1.1mm^3) was segmented from the "Duke" model [151] and located at the iso-center of the TEM (Figure 5-2A). The EM field and reflection (S11)/transmission (S12) coefficients from the 2 excitation ports (responsible for quadrature excitation) were calculated with our in-house FDTD software using a true transmission line model for excitation [51, 66, 68, 76]. Calculated EM fields from each port were linearly superimposed with 90-degree different phases and B_1^+ field distribution (B_1^+ inhomogeneity = standard deviation/mean) and SAR were obtained. The mean B_1^+ field intensity (degree per input of 100V) was calculated to compare to the in-vivo B_1^+ measured in the knee region. Peak SAR (W/kg) was calculated using the following equation and was determined for a 10gram pixel average:

$$SAR_{(x,y,z)} = \frac{1}{2}\left(\frac{\sigma_{(x,y,z)}\left(E^2_{x(x,y,z)}+E^2_{y(x,y,z)}+E^2_{z(x,y,z)}\right)}{\rho_{(x,y,z)}}\right) \quad (5–1)$$

where σ is the conductivity, ρ is the density of tissue in the knee, and *x*, *y*, and *z* represent coordinates in the Cartesian system.

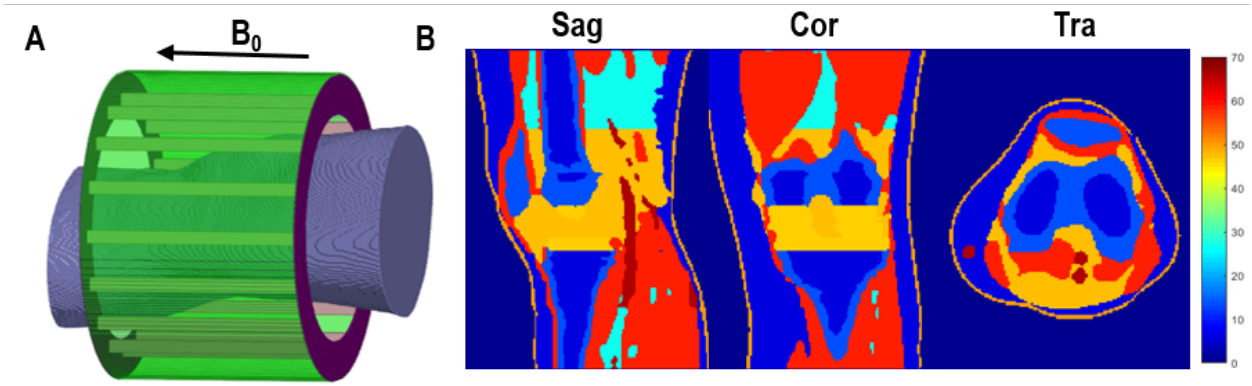

Figure 5-2 FDTD model of TEM coil with 3D knee model co-centered at the iso-center of the coil. A total grid of 251*251*291 cells was assigned for simulation of B_1^+ and SAR calculations. (A) Complete set-up for the FDTD calculation. (B) Anatomy of 3D knee model used for FDTD simulation. The color bar represents the relative permittivity of the tissues in the numerical model.

Table 5-1. Electromagnetic properties used for FDTD calculation

	Tissue/material	Conductivity (σ) [S/m]	Relative permittivity (ε_r) [F/m]	Density (ρ) [kg/m^3]
3D knee model	Air	0	1	0
	Bone Marrow	0.2730	5.7608	1027
	Bone	0.0825	13.446	1990
	Blood	1.3154	65.689	1060
	Connective Tissue	0.2881	26.818	1013
	Cartilage	0.5518	46.808	1098
	Fat	0.0395	5.6354	916
	Muscle	0.77	58.229	1041
	Skin	0.6404	49.9020	1110
	Tendon/Ligament	0.5366	48.001	1110
TEM	Copper	PEC (58.5×10^6)	PEC (~0)	N/A
	Acrylic	0	3	N/A
	Teflon	10^{-23}-10^{-25}	2.1	N/A

5.2.4 Imaging Studies

The study was approved by the University of Pittsburgh's Institutional Review Board (IRB), and a total of four volunteers were recruited and scanned with consent. All of the MR studies were performed on a 7T human scanner (Magnetom®, Siemens Medical System, Erlangen, Germany), and one of the subjects underwent 3T (Trio2; Siemens Medical System, Erlangen, Germany) imaging for SNR evaluation. We used a body coil as the Tx and a vendor 8-channel knee coil as the Rx for the 3T MR imaging. A 3D B_1^+ field map was acquired with a modified saturated turbo flash (SaT TFL) sequence. A presaturation pulse was applied prior to each partition to create z-magnetization. The presaturation consisted of a rectangular RF pulse (1 ms) followed by a set of trapezoidal gradient crushers applied on all three axes simultaneously. The duration of the crusher gradient = 8 ms, and the peak amplitude = 13 mT/m. The nominal flip angle (8 steps) for the presaturation pulse was varied from 0 to 160 degrees. The sequence parameters were: TR/TE = 2000/1.5 ms, voxel resolution = 3.0 x 3.0 x 3.0 mm^3; flip angle for excitation pulse = 8 degrees; and a total scan time = 2 min. Acquired data was then fit to the cosine function using MATLAB (Mathworks, MA). Afterwards, B_1^+ inhomogeneity (standard deviation/mean) was calculated in both the phantom and knee volumes.

A 3D dual echo steady state (DESS) T2-weighted sequence was used to measure increases in SNR with and without the Rx-only array at 7T and 3T vs 7T. Without the Rx-only setup, the TEM Tx-only coil was used as a Tx/Rx to acquire the SNR map in the phantom (diameter x length = 115mm x 210mm). Imaging parameters were: TR/TE = 15/5 ms; FA = 17 degrees; in-plane resolution = 0.6 x0.6 mm^2; slice thickness = 0.6mm; and a total scan time = 8.5

min. In addition, a Gradient Recalled Echo (GRE) with water excitation was acquired for SNR and CNR calculation in the cartilage at 3T and 7T; the signal from the bone was suppressed; therefore, clear delineation of the cartilage from the surrounding bone was achievable. Imaging parameters for the 3D GRE water excitation sequence were: TR/TE = 12/5 ms; FA = 10 degrees; in-plane resolution = 0.4 x 0.4 mm^2; slice thickness = 0.4mm; and a total scan time = 21 min.

SNR and contrast to noise ratio (CNR) calculation for the cartilage was done using the equation:

$$SNR = \frac{SI_{(x,yz)}}{Noise} \tag{5-2}$$

$$CNR = \frac{SI_{(cartilage)} - SI_{(bone)}}{Noise} \tag{5-3}$$

where SI is the signal intensity of the knee, and noise is the standard deviation calculated from the four corners of the image (see white dotted boxes in Figure 5-7 and 5-8); *x*, *y*, and *z* are pixel locations in the MR images. Signal intensity in the Patella and bone was measured in transverse and the sagittal plane was used to measure the Femur cartilage (signal intensity was not measured where cartilage thickness <1mm due to decreased signal as a result of the partial volume effect). Measurements were executed by a radiologist with more than 15yrs of experience. Finally, a 3D-DESS T2-weighted high spatial resolution (0.4 mm^3) of the in-vivo knee MR imaging was acquired at 7T.

5.3 RESULTS

5.3.1 Reflection and Transmission Coefficient (S11/S12) in the Knee; FDTD Simulation VS Bench Measurement

For the quadrature excitation, one port was connected to the constant phase shifter having a 90degree phase delay, and S11/S12 of the TEM Tx-only was measured. An S11/S12 of ~-25/-15dB was measured whereas -22/-12dB was calculated in the FDTD software. For the 8ch. Rx-only array, a mean S11/S12 of -21.5/-20dB was measured. Figure 5-3 shows the S11/S12 of the TEM Tx-only and Rx-only measured from one subject.

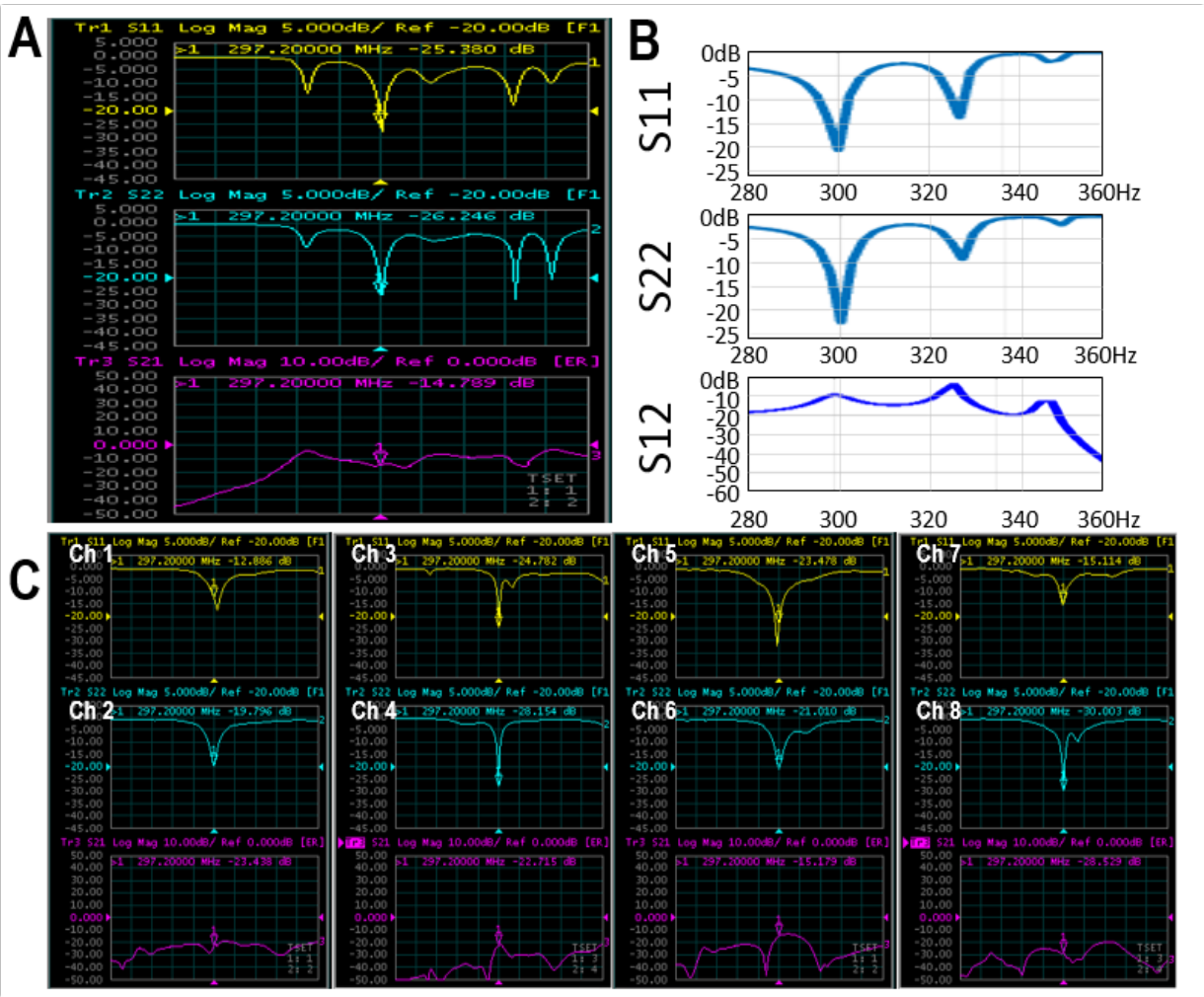

Figure 5-3 Reflection/transmission coefficients (S11/S12) measurement in TEM Tx-only and 8 Rx-only array and FDTD calculations in TEM. (A) and (B) S11 and S12 measured using network analyzer, showing ~-25~26 dB reflection and isolation of ~-15dB and FDTD calculations showing ~-22dB in reflection and ~-12dB in transmission, which are comparable. (C) S11 and S12 measured from all 8-channel Rx arrays. A mean S11 of -21±6 dB and S12 of ~22±5 dB was measured. Note that all measurements were done for the in vivo knee; thus the position could have deviated from the iso-center and resulted in the large standard deviation.

5.3.2 B_1^+ Evaluation and SAR

The B_1^+ inhomogeneity measured in the three subjects varied between 24%-27%, whereas that of the phantom measured 28%. In the FDTD calculations, the 3D knee model calculated 22% B_1^+ inhomogeneity whereas the phantom calculated 32%. The mean B_1^+ measured in the phantom was ~71 degrees per total input of 100V (Figure 5-4B) whereas the FDTD calculation results show ~77 degrees per same input voltage (Figure 5-4C). Utilizing a TEM Tx-only as Tx/Rx, a typical center bright and axis symmetry [22] (typically observed in volume coils due to the B_1 standing wave effect) was observed in the localizer and B_1^+ map (Figure 5-4A and B). In the FDTD calculations, a similar trend in the B_1^+ distribution (Figure 5-4C) was observed. Discrepancies in the field distribution/intensity between the experimental measurements and FDTD calculations resulted from an offset of the phantom position, associated coil tuning changes, and power loss from the electronics. For the 3D in vivo knee B_1^+ measurements, an ROI of 150mm in the sagittal plane was first selected to sufficiently cover the entire knee (white dotted line in Figure 5-5) and then a mean B_1^+ was measured in the transverse plane. The same ROI was selected for the FDTD calculations and the mean B_1^+ was calculated. The mean B_1^+ measured from all three subjects was ~53 degrees per input of 100V whereas the calculated B_1^+ was ~61 degrees (Figure 5-5).

The SAR (same ROI used for B_1^+ calculation) per 1W of input power in the 3D knee model is shown in Figure 5-6. Peak/average SAR (W/kg per 10g of tissue) was 0.34/0.076. Peak SAR was observed in the periphery of the knee, where the muscle tissue was dominant.

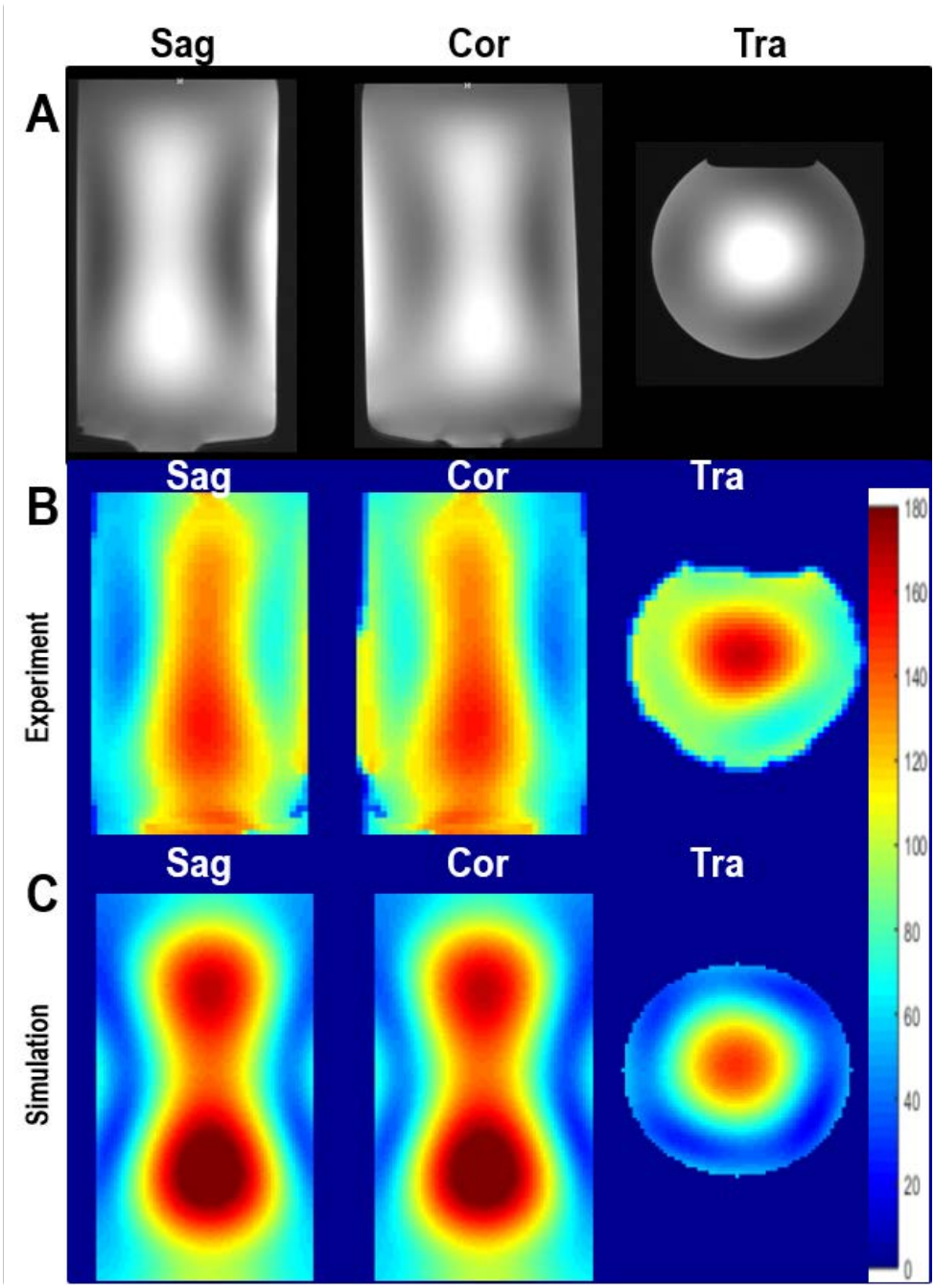

Figure 5-4 Localizer MR images and measured/calculated B_1^+ map of cylindrical phantom. (A) Three plane view of phantom localizer showing typical standing wave effect (center bright) observed in volume coil. (B) and (C) Axis symmetry B_1^+ was observed in three planes and experimental measurements were comparable to simulation results.

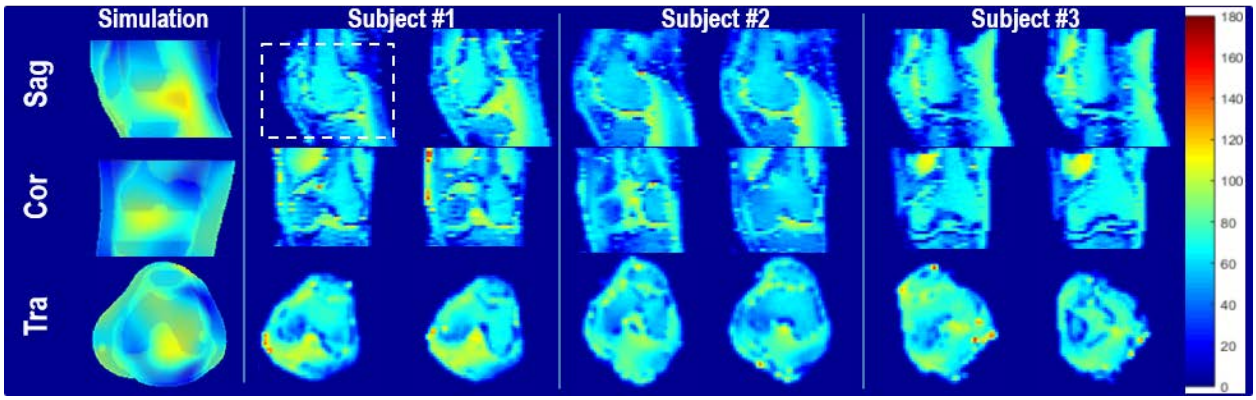

Figure 5-5 Calculated and measured B_1^+ map in 3D knee model and three subjects.

Unit is degree/100V with RF duration of 1ms.

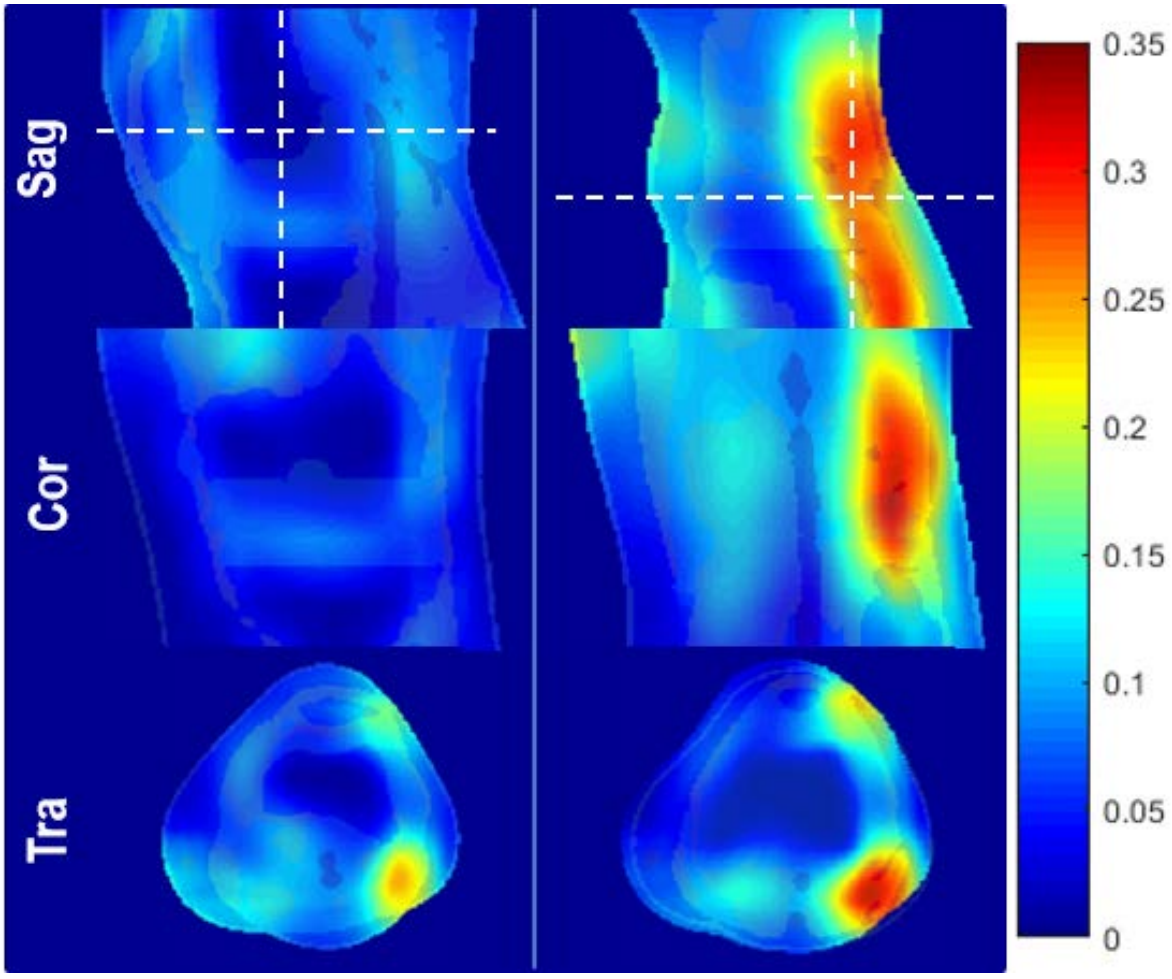

Figure 5-6 SAR map calculated in the 3D knee model. Unit is W/kg per 10g of tissue. The white dotted lines show the location of the coronal and transverse planes. RF power deposition in the center of the knee was negligible and peak SAR was calculated at the periphery of the knee, where the muscle was dominant.

5.3.3 SNR Comparison

5.3.3.1 With / Without Rx-Only Array at 7T

Figure 5-7 shows the SNR map acquired in the cylindrical phantom with/without an 8ch. Rx-only array at 7T. The SNR measured with the Rx-only array showed a 2-fold increase (mean SNR with/without Rx-only array: 430 vs 220) compared to the without Rx-only array set up. SNR significantly increased at the periphery of the phantom due to the high sensitivity of the surface coil (Figure 5-7 top panels). In addition, due to the lengthy Rx array along the coil axis (z-direction, 190mm), sensitivity along the axis also showed an increase (see black dotted box in Figure 5-7).

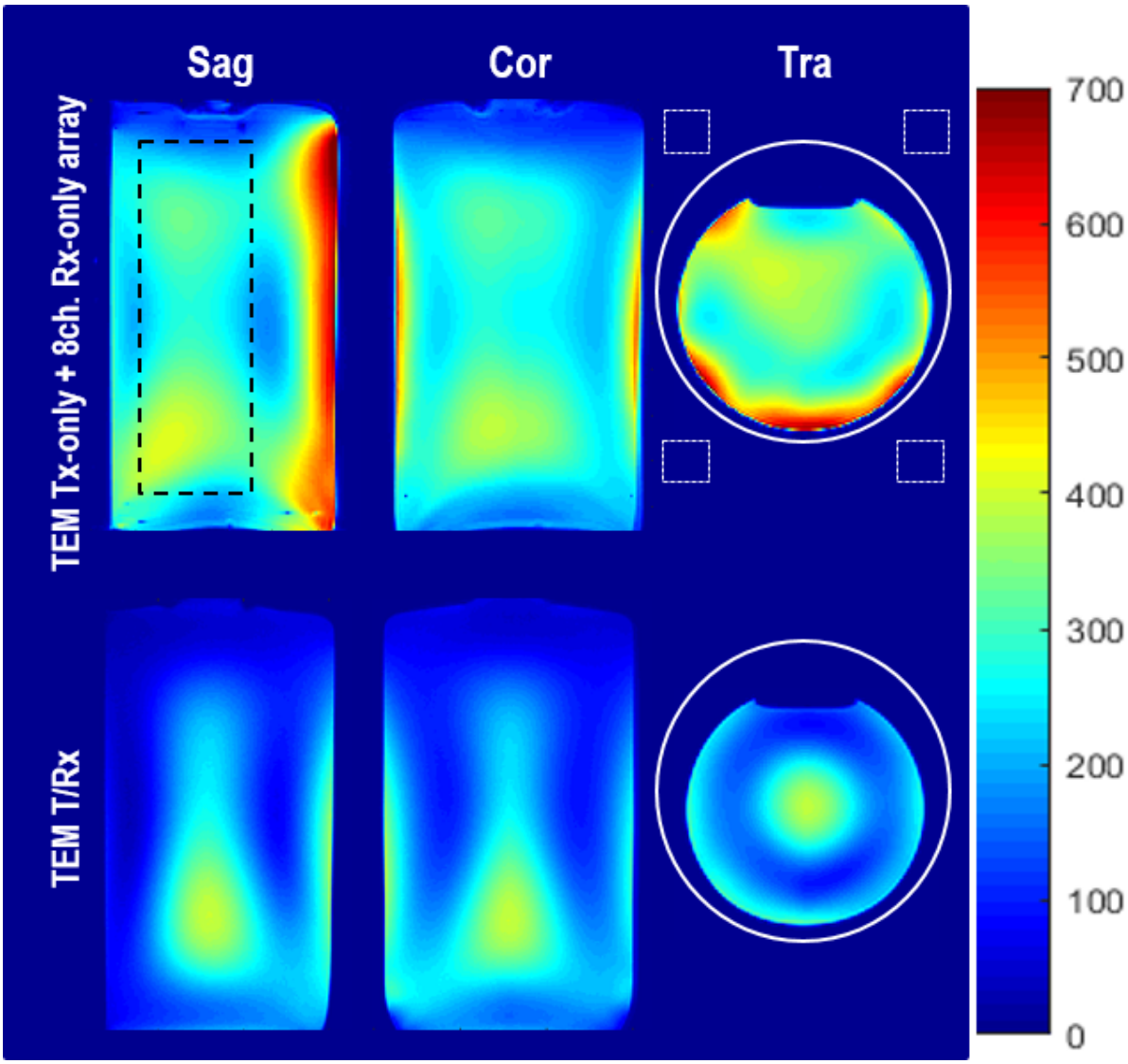

Figure 5-7 SNR map compared with/without Rx-only array at 7T showing more than 3-fold SNR increase at the periphery and 2-fold increase in entire volume. Sensitivity along the coil axis also increased (black dotted box). Background noise was calculated in the four corners of the transverse plane (white dotted box) and the white circles represent coil location.

5.3.3.2 3T VS 7T

Figure 5-8 shows a comparison of the SNR of 3T vs 7T using two different sequences. At two different static magnetic field strengths, we used an 8ch. Rx-only array and body coil/TEM at 3T/7T as a Tx-only coil. The SNR measured in the entire knee was ~15/~38, with the 3D DESS T2-weighted at 3T and 7T (Figure 5-8A).

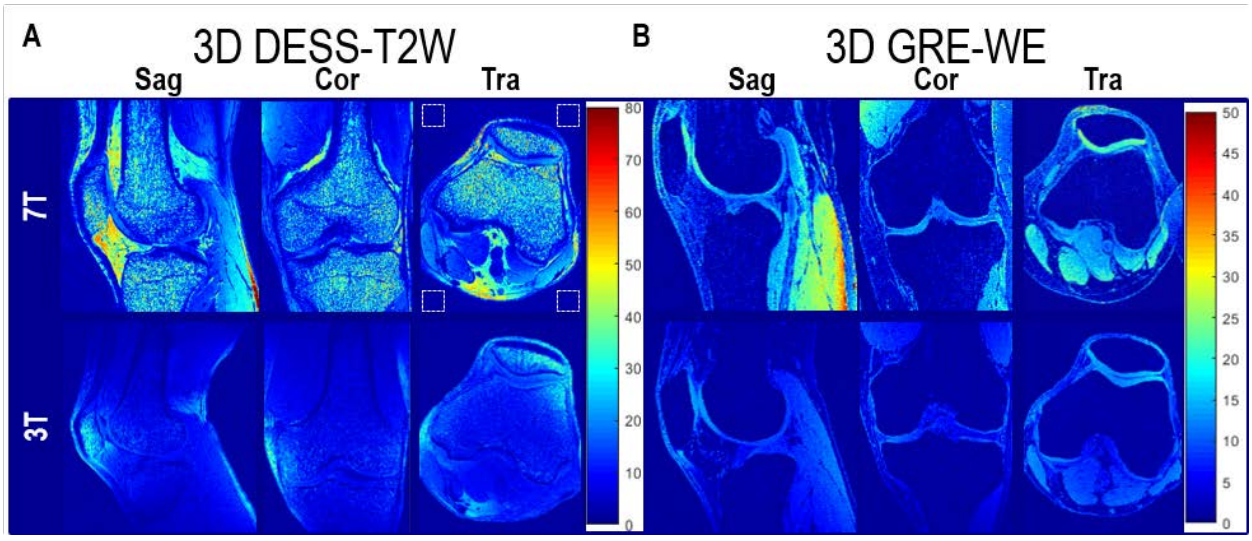

Figure 5-8 SNR map of in-vivo knee MR imaging at 3T and 7T. (A) 3D-DESS T2-weighted knee imaging. Note that the white dotted boxes represent the ROIs used for background noise calculation. (B) 3D GRE, with water excitation clearly delineating the cartilage and muscles. Signals from the bone region were successfully suppressed and used for SNR and CNR calculation of the cartilage.

5.3.4 SNR and CNR of the Cartilage

When the water excitation presaturation pulse was applied to suppress the magnetization from the bone, overall SNR decreased. The mean SNR in the entire volume of the knee was as a result of almost no SNR from the bone; however, a clear delineation of cartilage from the bone was achievable and the SNR/CNR of the cartilage and surrounding bone was measured. A mean SNR (cartilage) of ~13/25 was measured in 3T and 7T whereas a CNR of ~12/21 was measured (Figure 5-8B). Figure 5-9 shows an example of ROI drawing in the cartilage and bone.

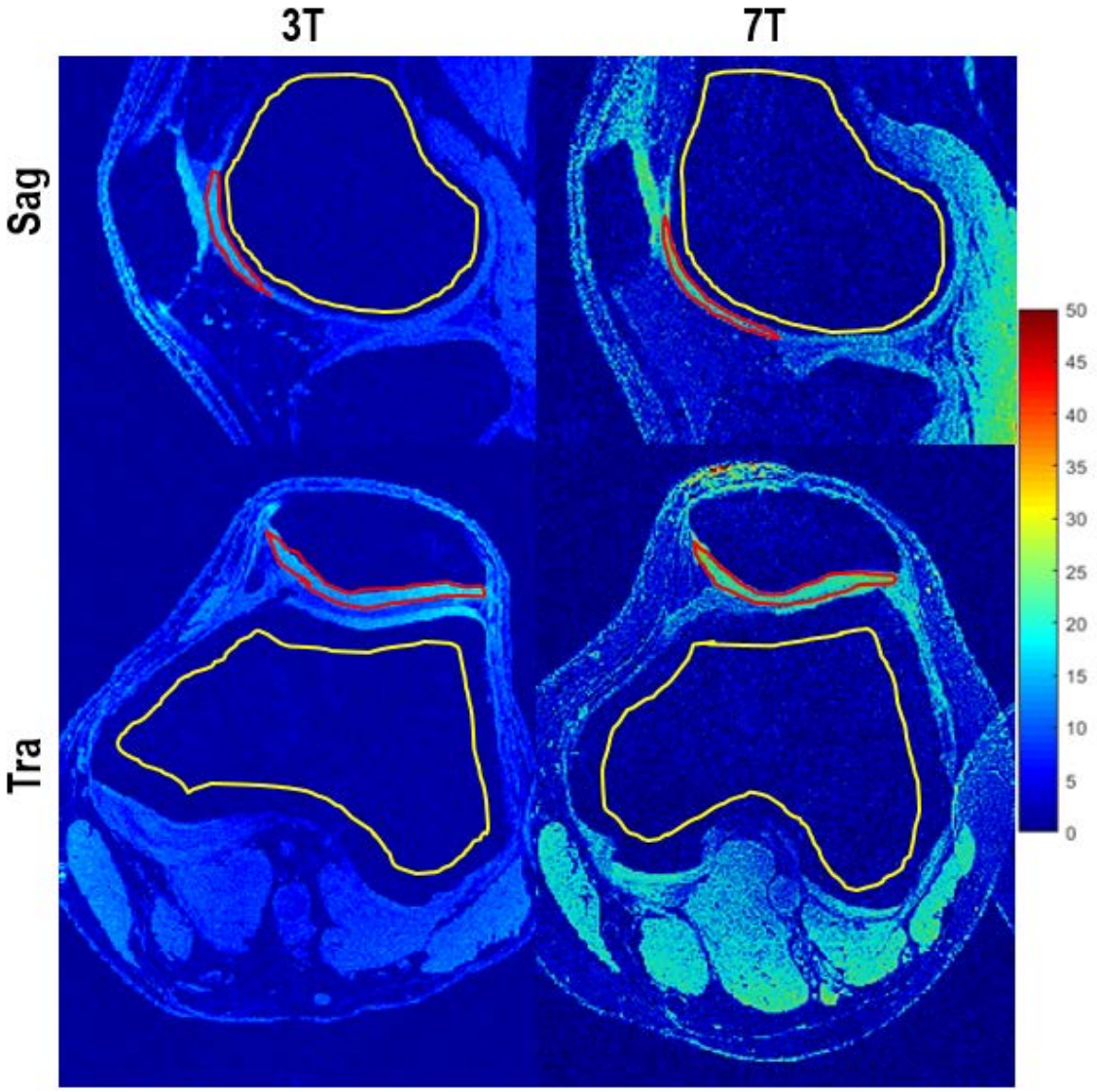

Figure 5-9 Manual ROI used for SNR and CNR calculations in the femur (sagittal) and patella (transverse) cartilage. The bone ROI is shown inside the yellow contour lines whereas the femur and patella are shown inside the red contour lines. The SNR and CNR were calculated slice by slice until the cartilage thickness was <1mm.

5.3.5 In-Vivo High Spatial Resolution Knee MR Imaging

Figure 5-10 show high spatial resolution (0.4 iso-mm^3) in vivo knee MR imaging acquired at 7T using the developed RF array.

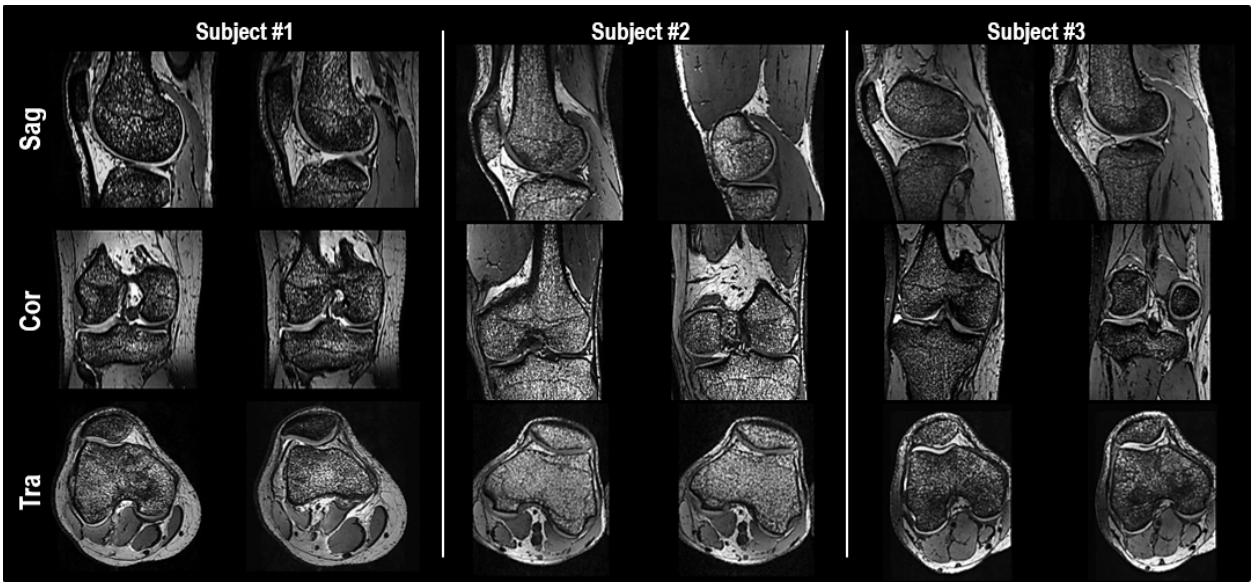

Figure 5-10 High spatial resolution (iso-0.4mm^3) of in-vivo knee MR imaging acquired from 3 subjects using a 3D DESS T2-Weighted sequence at 7T.

5.4 DISCUSSION AND CONCLUSION

In this study, we developed a 2 way-split RF array system for knee MR imaging at 7T. When developing an RF array with a split former, tuning and matching may be a challenge for the volume coil if the continuity of the circuit is not guaranteed. A split resonant peak is typically observed if the RF coil experiences an additional resonance mode near the center frequency.

Our FDTD model of a TEM was designed with a continuous RF shield so that it could be considered a TEM coil built on a fixed former. By comparing the experimental measurements of S11/S12 to the FDTD calculations shown in Figure 5-3A and B, we successfully demonstrated that our 2-way split TEM Tx-only array matches well with the FDTD model that mimics a TEM constructed on a fixed former. The S11 measured with the 8ch. Rx-only in the knee showed large variation depending on the location of the coil position respect to the knee. This variation is to be expected since knee tissue composition is not symmetric and an Rx-only array is located very close to the knee; the surface loop array has high sensitivity. We purposely did not re-tune the coil to each subject because the knee position inside the magnet for each subject was different from the position when the coil was tuned in the bench; therefore, when the coil S12 was >-15dB, we proceeded to imaging. FDTD calculations in the 3D knee model showed results comparable to our experimental results.

It is important to utilize EM simulations when developing an RF coil to ensure the safety of the subject as well as the protection of the RF hardware, especially in the calculation of RF power absorption. Our calculated Peak/Avg. SAR was well below the SAR limit set by the

International Electrotechnical Commission (IEC) and Food and Drug Administration (FDA); average SAR < 4W/kg, peak SAR < 20W/kg/10gram tissue [112, 167, 168]. Temperature measurements with an RF pulse induced heat in the sample has been investigated in couple of studies [43, 52, 112]; however, temperature measurements are not feasible in humans; thus the real-time SAR monitoring system was used during the entire scan time. In the knee model, Peak SAR was calculated in the region where the muscle tissue is mostly concentrated. The magnitude of the electric field generated by the Tx-array decays as the distance from the coil increases and the SAR is proportional to the conductivity and inversely proportional to the density of the tissue within the ROI. Thus, with the muscle's high conductivity and proximity to the transmit coil, the peak SAR measured in the muscle can be explained.

For knee MR imaging in practice, identifying the knee cartilage and measuring its thickness is very important because a degenerative knee disease such as osteoarthritis (OA) results in cartilage loss. To provide an accurate measurement, it is important to acquire MR imaging at high spatial resolution because the thickness of the cartilage is in the order of mm. Also, it is important to provide a clear delineation of the cartilage from the surrounding tissues.
We were able to acquire high spatial resolution knee MR imaging while successfully suppressing the signals from the bone. Figure 5-8A and B demonstrated that the MR signal from the bone, bone marrow, and capillaries was high and that it can be suppressed by applying a presaturation RF pulse. Figure 5-9 shows the MR signal from the bone was successfully suppressed at 3T, making the signal from the bone is similar to background noise; however, 7T imaging showed that the signal from the bone was relatively higher than that of 3T. We believe that the CNR measured for cartilage can be further improved by optimizing the pre-saturation time for water suppression. Figure 5-11 shows the signal profile across the cutline direction. SNR from the bone

at 3T and 7T is fairly homogeneous and shows clear delineation to cartilage; however, the bone SNR measured at 7T was generally higher than that at 3T, which implies that the homogeneous suppression of the signal within the bone was achieved but that the time interval between the pre-saturation RF pulse and excitation pulse needs further optimization.

High spatial resolution ($0.4mm^3$-iso) in vivo knee MR imaging in the three subjects (Figure 5-10) was acquired with a scan time of 8.5 min, which is typical duration of knee MR imaging at 3T. The in vivo knee MR imaging showed good soft tissue contrast, with clear delineation of cartilage and soft tissue with a high SNR.

In conclusion, we demonstrated the performance of the developed 2-way split RF array using specific measurements: 1) comparing the S11/S12 of the Tx-only and Rx-only with FDTD calculations, 2) comparing the SNR with/without Rx-only array at 7T as well as 3T vs 7T, and 3) measuring the SNR and CNR in the cartilage and as a feasibility test, acquiring high spatial resolution of in-vivo knee MR imaging at 7T.

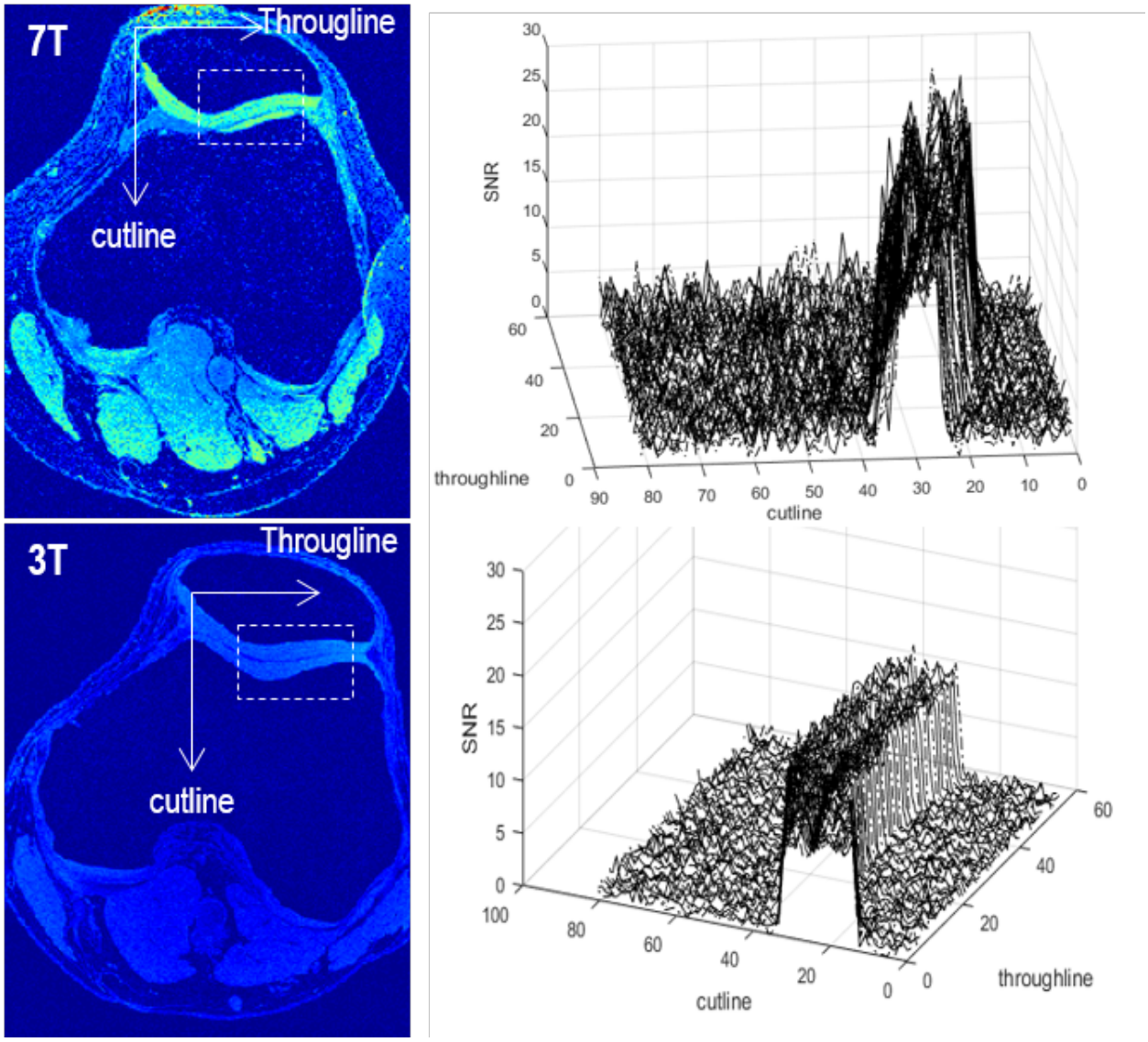

Figure 5-11 SNR profile measured along the cutline, stacked through the throughline, showing homogeneous signal suppression in the bone. The 7T knee image shows a more than 2-fold increase in SNR in the cartilage compared to that measured at 3T.

6.0 RF ARRAY DEVELOPMENT FOR EXTREMITY (KNEE AND FOOT) MR IMAGING AT 7T: PART 2. EXPLORATORY INVESTIGATION OF LOWER EXTREMITY IMAGING AT 7T MRI WITH TIC-TAC-TOE RF TRANSMIT DESIGN

Santini, T., Kim, J., Wood, S., Krishnamurthy, N., Farhat, N., Maciel, C., ... & Ibrahim, T. S. (2018). A new RF transmit coil for foot and ankle imaging at 7T MRI. *Magnetic resonance imaging*, *45*, 1-6.

6.1 INTRODUCTION

MRI has been used to investigate a wide range of abnormalities, injuries and diseases in the musculoskeletal system, such as cartilage degeneration [36, 134], bone marrow edemas [132], osteoarthritis [1, 36, 132, 169], osteoporosis [36, 133], and ligament/tendon insures [32, 169]. While most clinical diagnoses have been based on MR images acquired at 1.5 or 3T, the enhanced contrast and SNR provided by 7T MRI can be highly useful [2]. Intrinsically increased SNR at 7T MRI can be used to acquire 1) high spatial resolution images for a detailed structural or morphological investigation and/or 2) high temporal resolution images for the sake of patient comfort. However, despite the aforementioned advantages at 7T, several challenges exist, including: 1) the increased B_1^+ (circularly polarized magnetic field responsible for excitation) inhomogeneities, 2) increased chemical shift, and 3) increased peak and average specific

absorption ratio (SAR) [8]. To mitigate the B_1^+ inhomogeneity and high SAR, multi-channel Transceiver (T/Rx) RF coils capable of outputting a variable RF amplitude/phase at each channel have been developed for various parts of the body [6, 9, 23, 31, 39, 47, 49-51, 66, 70, 75, 135, 140]. As another challenge, a body coil in UHF scanners is usually unavailable (available at 1.5T and 3T scanners); thus the RF coil either must work as a transceiver or transmit (Tx)-only/receive (Rx)-only pairs must be built.

To the best of our knowledge, there are few research groups that have developed RF coils specifically for 7T imaging of the foot/ankle [37, 60], as most of studies have used commercial knee coils [4, 19, 28, 32, 33, 54] or head coils [7, 24, 107, 130] for imaging these parts of the body. This is not optimal because the subject may be asked to stay in an uncomfortable position (e.g., foot held at a high angle) and the coil may not be suitable and/or optimal for all foot sizes.

In this exploratory study, we used a Tic-Tac-Toe RF array design concept that has been used for brain, breast, and abdominal MR imaging at 7T [34, 35, 52, 61, 63, 65, 67, 71, 73, 75, 77, 170]. The B_1^+ maps and scattering parameters (S11/S12) of the constructed RF coil were experimentally measured in a cylindrical phantom.

6.2 MATERIALS AND METHODS

6.2.1 Tic-Tac-Toe (TTT) Tx/Rx Array Design and Evaluation

A Tic-Tac-Toe (TTT) coil (a Tx RF coil design inspired by the cross-pole antenna [34, 61, 63, 65, 75, 77, 170]) composed of eight squared-shape transmission lines electrically

connected to each other in a 2x2 format (Figure 6-1A and 1B) was built. The dimensions of the coil were 228.6 x 228.6 mm^2 in the *X* and *Y* directions and 16.8mm in the *Z* direction, which is the direction of the static magnetic field (B_0) (see Figure 6-1A). The inner rods of the transmission lines were made of solid squared-shape copper (McMaster-Carr, USA), with cross-section dimensions of 6.35x6.35mm^2 (see Figure 6-1B). The outer strut was built from an 8um thick single-layered copper sheet (Polyflon, Germany). The 4-channel T/Rx array assembly is shown in Figure 6-1A without an extended RF shield. The center pin of the excitation transmission lines was connected to the outer strut of the coil while the inner rod was connected to the shield/ground (Figure 6-1B). Matching and tuning rods were placed in an alternating fashion so that the coil had 4 excitation ports with matching rods and 4 tuning rods (Figure 6-1B). The Tx RF coil was tuned and matched to 50 Ohms at 297.2 MHz (Larmor frequency for ^1H at 7T) by changing the rods' length -- this affected the coil reactance and allowed the resonant frequency of the circuit to be adjusted to the scanner Larmor frequency. The complete assembly with an extended RF shield is shown in Figure 6-1C and the phantom used for the RF array evaluation is shown in Figure 6-1D.

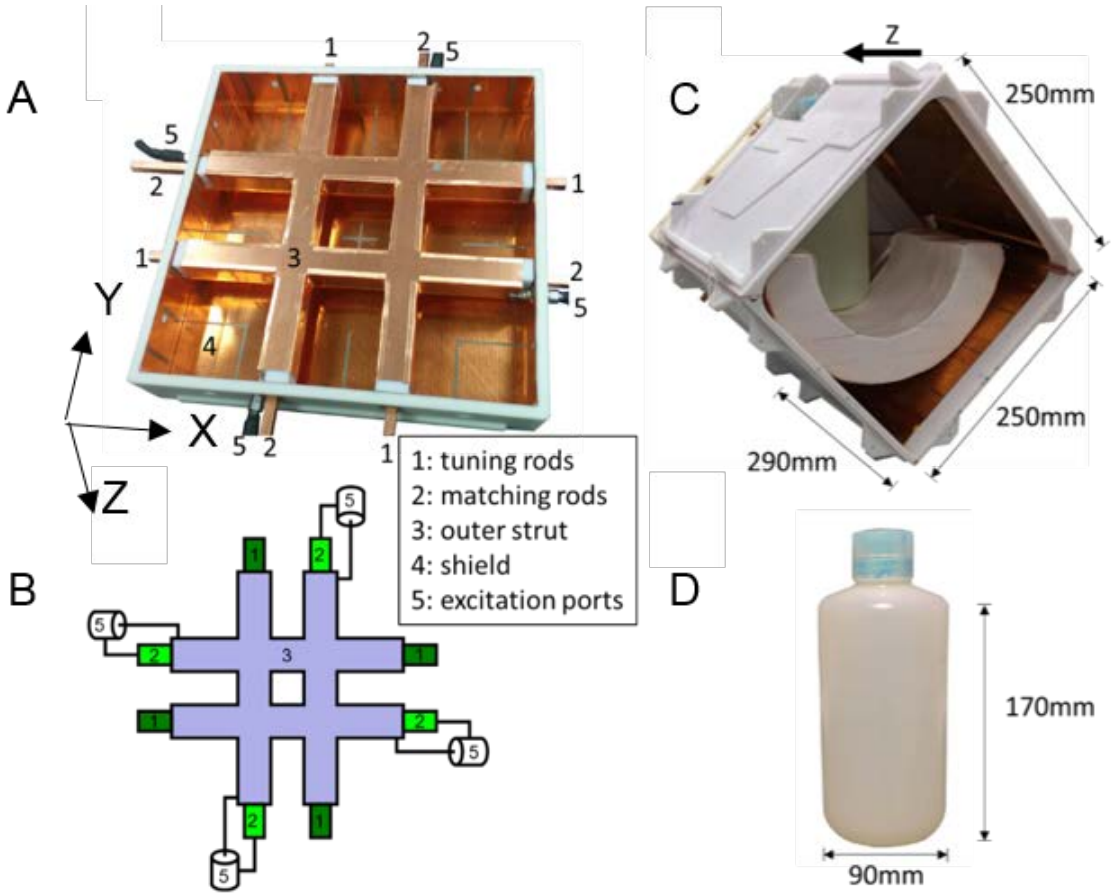

Figure 6-1 Design of the TTT foot and ankle Tx/Rx RF coil. (A) the assembled 4-channel Tx/Rx RF coil without the extended shielding frame. (B) the schematic of the RF coil. (C) complete assembly of the RF coil with RF shield. (D) homogeneous cylindrical phantom used for imaging studies, permittivity = 39 and conductivity = 0.49 S/m.

6.2.2 RF Shield Design

An RF shielding composed of double-layered copper sheets that were 4um thick at each layer (or approximately half of skin depth for copper at 7T), with a 0.254mm-thick dielectric in between (Polyflon, Germany) was placed to cover the transmitting elements described in Figure 6-1B. Split cuts were made in the copper sheets to effectively open the low-frequency eddy current pathways (the gradient coil's operational frequency is <1kHz and due to the fast switches in readout gradient direction, eddy currents are induced in the continuous copper sheet with an order of hundreds of Hz), thus avoiding potential fast gradient switching artifacts while maintaining the RF characteristics associated with the Tx coil as described in [65]. The shields were extended to enclose the entire lower leg, except for a cavity on the top to accommodate the toes, thus allowing all sizes of feet and placement positions (see the opening in Figures 6-1C). The overall size of the coil is 250*250*290mm^3 (Figure 6-1C).

6.2.3 Workbench Test

The lengths of the inner rods for tuning/matching of the RF coil were estimated using finite-difference time-domain (FDTD) simulations and then fined-tuned in the bench while the coil was loaded with a homogenous phantom that corresponded to the averaged values of permittivity and conductivity of the Duke virtual family model at 297MHz. The coupling of the RF coil is inherently high due to its design [34, 52, 77, 170]; therefore, changing one rod can affect all the channels. The s-matrix was measured using a network analyzer (Model E5062A, manufactured by Agilent Technologies).

6.2.4 MRI Test

The developed RF array was tested in the 7T Human Scanner Magnetom (Siemens, Germany). A transmit/receive (T/R) switch box was installed with the RF coil. The system can operate either in the single-channel mode, using a 4-way Wilkinson power splitter, or it can use the pTx mode available in the scanner to operate as a 4-channel transmit array if needed. Constant phase shifters (with 90-degree increments) were added in the transmission lines to produce 4-port pseudo-quadrature excitation.

B_1^+ maps were acquired in a homogeneous cylindrical phantom (Figure 6-1D). The sequence used was a saturated turbo FLASH sequence with the following parameters: TE/TR = 1.09/3000ms, resolution 3.1x3.1x3.1mm^3, FOV 112x200, a 36x64 acquisition matrix, six flip-angles for pre-saturation varying from 0 to 90 degrees, and total time of scan of 6 minutes. The data was then fitted to a cosine function using MATLAB and a $\mathbb{B}_1^+$ map was calculated.

6.3 RESULTS

6.3.1 Transmission and Reflection Coefficient Measurement

Using a homogeneous cylindrical phantom as a load, a reflection coefficient (Sxx) was measured better than -20dB for all 4 channels. One representative channel is shown in Figure 6-2A. Figure 6-2B shows the measured S-matrix for all four channels of the developed RF coil. The mean measured reflection coefficient was -30.4dB, while the average coupling among opposite ports (e.g. S13 and S24) was -4.1dB and the average coupling for adjacent ports (e.g. S12 and S23, …) was -9.56dB. Note that high coupling between the opposite ports is a unique characteristic of the TTT coil family, which happens at the cost of reduced B_1^+ per input power but promotes B_1^+ homogeneity and RF field consistency with different loads, as demonstrated in prior studies [25-27, 31, 36].

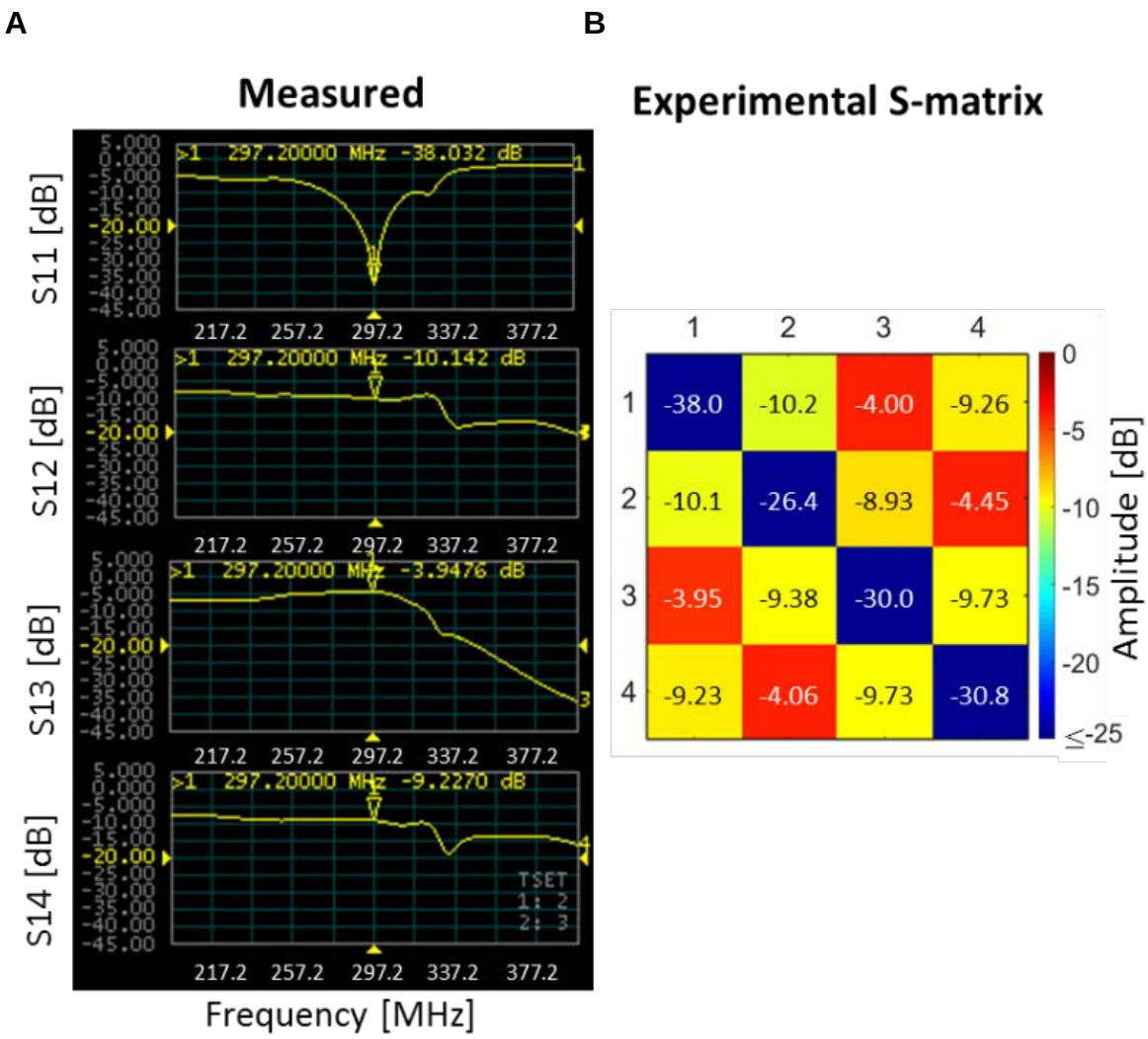

Figure 6-2 Scattering parameters of the designed TTT RF array. (A) the experimental measurement of transmit and reflection coefficients of channel 1. (B) the experimental S-matrix from all 4 channels.

6.3.2 Simulated and Measured B_1^+ Distributions in the Homogeneous Phantom

Figure 6-3A presents the measured B_1^+ field distribution, normalized for 1W input power in the sagittal, coronal, and axial plane, respectively. The B_1^+ field profile along the axis (white dotted line) at three planes is shown in Figure 6-3B. The average B_1^+ measured along the axis was (on the white dotted lines) 0.57uT, 0.58uT, and 0.61uT for the sagittal, coronal, and axial planes, respectively.

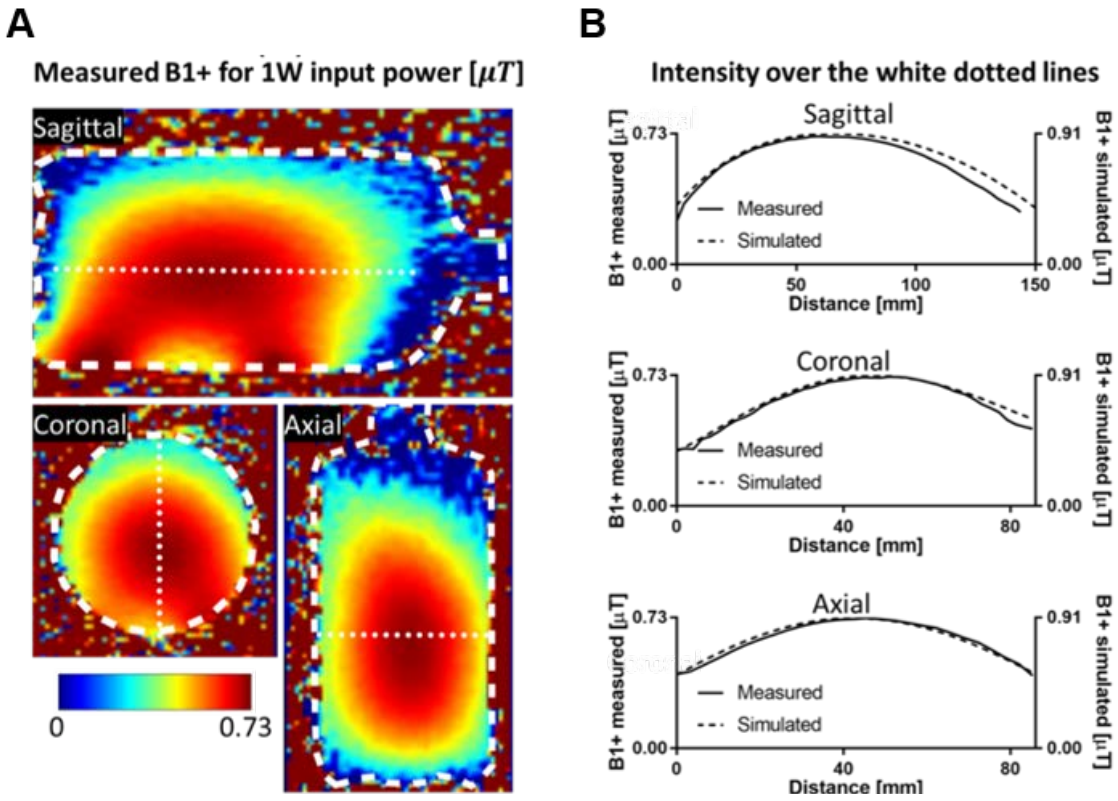

Figure 6-3 (A) Phantom B_1^+ map measurements per 1W input power. (B) B_1^+ intensity profile along the white dotted lines in three planes.

6.4 DISCUSSION AND CONCLUSION

The lack of a Tx body coil for 7T MRI has forced the development of transmit coils dedicated for certain parts of the body. Due to the absence of a commercial RF coil specific for the foot/ankle at 7T, most sites use knee coils [4, 19, 28, 32, 33, 54] or head coils [7, 24, 107, 130] for imaging the foot/ankle. This situation is not optimal for several reasons. In the case of knee coils (which usually have a cylindrical shape and were developed to closely fit a knee), the foot has to stay at a high angle position (the recommended position is less than 20 degrees of flexion [169]). This makes imaging unviable in cases like fracture or severe disease, where movement of the foot is impaired. In the case of head coils, different sizes of foot may not fit due to the limited space available. The proposed TTT T/Rx coil has its elements positioned in the XY plane of the scanner; therefore, the foot and ankle can be imaged in a relaxed position. Furthermore, the proposed TTT RF coil does not have any lumped elements as it utilizes distributed capacitances, which help in terms of robustness and manufacturing. Due to the relatively large size and the gap in the RF shielding (Figure 6-1C), any size of foot and lower leg can be scanned. Moreover, it is possible to adjust the position of the foot based on the region of interest. An accurate simulation of the coil and the transmission lines is essential to ensure performance and to predict SAR, since the local SAR cannot be accurately measured or estimated in real time by the MRI scanner. However, because it is in the early phase of design

concept evaluation and considering that the MRI experiment was planned to occur in the phantom, simulation was determined to be a good next step.

Further improvements for this exploratory study are needed, such as building an Rx-only insert with a proper decoupling system that can be integrated with the proposed Tx coil (not suitable for optimal receive operation due to its high coupling). This should not significantly affect the RF performance of the Tx coil [171] and should improve SNR for performing human imaging experiments. FDTD simulation of B_1^+ map in the phantom and in-vivo model will be performed to compare and evaluate our design to those presented in other published articles, such as Wright et al.[60] and Orzada et al.[37].

7.0 CONCLUSION

7.1 SUMMARY

7.1.1 Experimental and Numerical Analysis of Transmit Field and SAR with a New Transmit Array Design for Breast MRI

A new 8-channel Tx array design was introduced for breast MRI at 7T. For the safety of the subject during MRI with a 7T UHF scanner, accurate prediction of the B_1^+ field and SAR is critical. In the study, the developed Tx array's B_1^+ field intensity and distribution was numerically evaluated using various breast models and compared to experimentally acquired data from the breast phantom. In addition, B_1^+ field distribution and SAR were calculated with and without the RF shield to closely look at the shielding effect on the breast. The analysis demonstrated that the RF shield plays a significant role in improving the B_1^+ field homogeneity and allowing a relatively lower SAR in the breast. We also performed temperature measurements to estimate the RF heat deposition in the breast phantom during the RF coil operation. Results were comparable to the SAR distribution calculated in the breast model. Through the quantitative comparison study, consistent agreement between the simulation results and experimental measurements were demonstrated.

7.1.2 Development of a 7T RF Coil System (Transmit and Receive) for Breast Imaging

The new RF coil system, composed of an eight-channel Tx-only array based on a TTT design in conjunction with an eight-channel Rx-only insert, was developed for human breast MRI at 7T. Characterizations of the B_1^+ field and associated SAR generated by the developed RF coil system were numerically calculated and empirically measured using an anatomically detailed breast model, a phantom and a human breast. About 20% B_1^+ inhomogeneity within the breast tissue was calculated and measured for the simulation and the experiment at 7T. The breast phantom study at 7T with and without an Rx-array showed factor of three increase in SNR. An in-vivo breast MRI comparison between 3T and 7T showed a four-fold SNR increase and two-fold CNR increase, respectively – which makes higher resolution MR imaging at 7T possible but challenging at 3T. In addition, an Rx array noise matrix and g-factor map was acquired to demonstrate the signal coupling and the feasibility of parallel imaging. As a final evaluation of the developed RF coil performance, a sub-millimeter (0.6-mm isotropic) 3D in-vivo breast MRI was acquired at 7T, which showed clear delineation of fat tissues from the fibroglandular tissues in the breast.

7.1.3 RF Array Development for Extremity (Knee and Foot) MR Imaging at 7T

7.1.3.1 Part 1. Two Way – Split RF Array Development for Knee MRI at 7T

A TEM Tx-only array and eight-channel Rx-only array RF coil were designed to split into two separate parts, i.e., two half hemispheric cylindrical coils, for patient comfort and easy access. However, this requires additional mechanical input to ensure reliable connection between the joints of the two parts. The developed two-way split RF coil design was experimentally evaluated by measuring the B_1^+ field in the knee of three subjects and comparing the results to a numerically calculated B_1^+ field in a human knee model. Numerical calculation was done for a non-split TEM RF coil design as well so that comparison to the experimental results could be done to demonstrate the robustness of the mechanical design of the two-way split. Through the 1) bench test, 2) the phantom study and 3) the in-vivo knee B_1^+ field acquisition, the results for the two-way split design were comparable to those of the non-split design. The comparison of in-vivo knee MRI at 3T and 7T showed significant SNR and CNR increases at 7T. As a feasibility test for application for osteoarthritis, we acquired high resolution (0.4-mm isotropic) in-vivo knee MRI with a scan time of less than 9 min.

7.1.3.2 Part 2. Exploratory Investigation of Lower Extremity Imaging at 7T MRI with Tic-Tac-Toe RF Transmit Design

As an exploratory study, the TTT design that was used for breast imaging was applied with larger dimensions and more RF shielding in ankle and foot imaging. A human leg model was used for numerical evaluation of RF coil performance and the calculated results were compared to experimental results. The coupling matrix of the Tx array and B_1^+ field distribution in the foot and the ankle for the simulation and experiment matched well, and the SAR was kept within acceptable range over the whole lower leg. Due to the asymmetric geometry of the foot, RF coil design for the lower leg has not been well established or studied. In fact, knee or head coils are often used to study the lower extremities [19, 33, 54, 107, 130], which often causes subject discomfort. Also, numerical studies are rare. However, the proposed RF coil design has excitation ports in the XY plane that the foot can rest on in comfort.

7.2 FUTURE WORK

The innovative TTT Tx coil was designed to produce a homogeneous B_1^+ field and less SAR generation. In addition, in combination with the Rx-only array, it improved the SNR even more, making higher resolution and contrast MRI at 7T feasible. Our new RF coil design was first applied for brain applications and expanded to breast and knee/foot at 7T MRI. Currently, we are using 20 channel Tx-only array combined with 32 channel Rx-only array head coil system for major depressive disorder studies, such as, schizophrenia, Parkinson's disease, and Alzheimer's disease. We are expecting to have >2000 in-vivo patient scans through 2022. For the breast MR imaging, we hope to use our RF coil design and methodology as a secondary monitoring tool for subjects with dense FG breast tissues. Also, providing high resolution breast MR images can be beneficial for early detection of breast tissue abnormalities. For the knee and foot, we would like to use our extremity RF coil system for MSK degeneration disease investigation, such as OA and RA. By providing high resolution MR image for cartilages, ligaments, and tendons, we may find biomarker for early detection of MSK degeneration diseases.

Last but not least, this TTT Tx design is very distinctive in that 1) it does not require any lumped element, 2) it exhibits high coupling within the element, and 3) it exhibits low coupling between the elements. It can be further studied to extend to whole body imaging in UHF MRI applications.

BIBLIOGRAPHY

1. Alizai, H., G. Chang, and R.R. Regatte, *MRI of the Musculoskeletal System: Advanced Applications using High and Ultrahigh Field MRI.* Semin Musculoskelet Radiol, 2015. **19**(4): p. 363-74.

2. Bangerter, N.K., et al., *Quantitative techniques for musculoskeletal MRI at 7 Tesla.* Quant Imaging Med Surg, 2016. **6**(6): p. 715-730.

3. By, S., et al., *A 16-Channel Receive, Forced Current Excitation Dual-Transmit Coil for Breast Imaging at 7T.* PloS one, 2014. **9**(11): p. e113969.

4. Deligianni, X., et al., *High-resolution Fourier-encoded sub-millisecond echo time musculoskeletal imaging at 3 Tesla and 7 Tesla.* Magn Reson Med, 2013. **70**(5): p. 1434-9.

5. Eckstein, F., et al., *Non-invasive determination of cartilage thickness throughout joint surfaces using magnetic resonance imaging.* Journal of biomechanics, 1997. **30**(3): p. 285-289.

6. Fujita, H., *New horizons in MR technology: RF coil designs and trends.* Magnetic Resonance in Medical Sciences, 2007. **6**(1): p. 29-42.

7. Krug, R., et al., *In vivo ultra-high-field magnetic resonance imaging of trabecular bone microarchitecture at 7 T.* J Magn Reson Imaging, 2008. **27**(4): p. 854-9.

8. Moser, E., et al., *7-T MR--from research to clinical applications?* NMR Biomed, 2012. **25**(5): p. 695-716.

9. Robitaille, P.-M. and L. Berliner, *Ultra high field magnetic resonance imaging*. Vol. 26. 2007: Springer Science & Business Media.

10. Slichter, C.P., *Principles of magnetic resonance*. Vol. 1. 2013: Springer Science & Business Media.

11. Bloch, F., *Nuclear induction.* Physical review, 1946. **70**(7-8): p. 460.

12. Bloch, F. and E.M. Purcell, *Nobel Prize for Physics, 1952.* Nature, 1952. **170**: p. 911-912.

13. Morse, O. and J. Singer, *Blood velocity measurements in intact subjects.* Science, 1970. **170**(3956): p. 440-441.

14. Lauterbur, P., *Image formation by induced local interactions: examples employing nuclear magnetic resonance.* 1973.

15. Mansfield, P. and P.K. Grannell, *NMR'diffraction'in solids?* Journal of Physics C: solid state physics, 1973. **6**(22): p. L422.

16. Mansfield, P. and I. Pykett, *Biological and medical imaging by NMR.* Journal of Magnetic Resonance (1969), 1978. **29**(2): p. 355-373.

17. Wehrli, F.W., *On the 2003 Nobel Prize in medicine or physiology awarded to Paul C. Lauterbur and Sir Peter Mansfield.* Magnetic resonance in medicine, 2004. **51**(1): p. 1-3.

18. Ibrahim, T., et al. *20-to-8 channel Tx array with 32-channel adjustable receive-only insert for 7T head imaging*. in *Proceedings of the 21st Annual Meeting of ISMRM, Salt Lake City, Utah, USA*. 2013.

19. Juras, V., et al., *Comparison of 3T and 7T MRI clinical sequences for ankle imaging.* Eur J Radiol, 2012. **81**(8): p. 1846-50.

20. Korteweg, M.A., et al., *Feasibility of 7 Tesla breast magnetic resonance imaging determination of intrinsic sensitivity and high-resolution magnetic resonance imaging, diffusion-weighted imaging, and (1)H-magnetic resonance spectroscopy of breast cancer patients receiving neoadjuvant therapy.* Invest Radiol, 2011. **46**(6): p. 370-6.

21. Kozlov, M. and R. Turner. *Analysis of RF transmit performance for a 7T dual row multichannel MRI loop array*. in *Engineering in Medicine and Biology Society, EMBC, 2011 Annual International Conference of the IEEE*. 2011. IEEE.

22. Vaughan, J.T., et al., *7T vs. 4T: RF power, homogeneity, and signal-to-noise comparison in head images.* Magnetic resonance in medicine, 2001. **46**(1): p. 24-30.

23. Abraham, R. and T.S. Ibrahim, *Proposed radiofrequency phased-array excitation scheme for homogenous and localized 7-Tesla whole-body imaging based on full-wave numerical simulations.* Magnetic Resonance in Medicine, 2007. **57**(2): p. 235-242.

24. Banerjee, S., et al., *Rapid in vivo musculoskeletal MR with parallel imaging at 7T.* Magn Reson Med, 2008. **59**(3): p. 655-60.

25. Boer, V.O., et al., *Multislice 1H MRSI of the human brain at 7 T using dynamic B0 and B1 shimming.* Magnetic resonance in medicine, 2012. **68**(3): p. 662-670.

26. Brown, R., et al., *Breast MRI at 7 Tesla with a bilateral coil and robust fat suppression.* J Magn Reson Imaging, 2014. **39**(3): p. 540-9.

27. Chang, G., et al., *Adaptations in trabecular bone microarchitecture in Olympic athletes determined by 7T MRI.* Journal of Magnetic Resonance Imaging, 2008. **27**(5): p. 1089-1095.

28. Domayer, S.E., et al., *Cartilage repair of the ankle: first results of T2 mapping at 7.0 T after microfracture and matrix associated autologous cartilage transplantation.* Osteoarthritis Cartilage, 2012. **20**(8): p. 829-36.

29. Emir, U.E., et al., *Regional neurochemical profiles in the human brain measured by 1H MRS at 7 T using local B1 shimming.* NMR in Biomedicine, 2012. **25**(1): p. 152-160.

30. Gruber, S., et al., *Dynamic contrast-enhanced magnetic resonance imaging of breast tumors at 3 and 7 T: a comparison.* Invest Radiol, 2014. **49**(5): p. 354-62.

31. Ibrahim, T.S., Y.K. Hue, and L. Tang, *Understanding and manipulating the RF fields at high field MRI.* NMR in Biomedicine, 2009. **22**(9): p. 927-936.

32. Juras, V., et al., *Histological correlation of 7 T multi-parametric MRI performed in ex-vivo Achilles tendon.* Eur J Radiol, 2013. **82**(5): p. 740-4.

33. Juras, V., et al., *Regional variations of T(2)* in healthy and pathologic achilles tendon in vivo at 7 Tesla: preliminary results.* Magn Reson Med, 2012. **68**(5): p. 1607-13.

34. Kim, J., et al., *Development of a 7 T RF coil system for breast imaging.* NMR Biomed, 2016.

35. Kim, J., et al. *High temporal and spatial resolution breast MR imaging at 7T; Feasibility Study using 8-to-1 channel Tx-only Array Combined with 8 channel Rx-only Insert 2013*. in *Proc Intl Soc Mag Reson Med*. 2013.

36. Krug, R., et al., *Imaging of the musculoskeletal system in vivo using ultra-high field magnetic resonance at 7 T.* Invest Radiol, 2009. **44**(9): p. 613-8.

37. Orzada, S., et al., *Open design eight-channel transmit/receive coil for high-resolution and real-time ankle imaging at 7 T.* Med Phys, 2011. **38**(3): p. 1162-7.

38. van de Bank, B.L., et al., *Ultra high spatial and temporal resolution breast imaging at 7T.* NMR Biomed, 2013. **26**(4): p. 367-75.

39. van den Bergen, B., et al., *SAR and power implications of different RF shimming strategies in the pelvis for 7T MRI.* Journal of Magnetic Resonance Imaging, 2009. **30**(1): p. 194-202.

40. Vaughan, J.T., et al., *Whole-body imaging at 7T: preliminary results.* Magnetic resonance in Medicine, 2009. **61**(1): p. 244-248.

41. Cha, S. and J. Gore, *Clinical applications of ultra-high field 7T MRI–moving to FDA/EU approval*, in *Proc. Intl. Soc. Mag. Reson. Med. 19*. 2011.

42. Cloos, M. and G. Bonmassar. *Towards direct B1 based local SAR estimation*. in *Proceedings of the 17th Annual Meeting of ISMRM, Honolulu, Hawaii, USA*. 2009.

43. Collins, C.M., et al., *Temperature and SAR calculations for a human head within volume and surface coils at 64 and 300 MHz.* Journal of Magnetic Resonance Imaging, 2004. **19**(5): p. 650-656.

44. de Moortele, V., et al., *B1 destructive interferences and spatial phase patterns at 7 T with a head transceiver array coil.* Magnetic resonance in medicine, 2005. **54**(6): p. 1503-1518.

45. Finnerty, M., et al. *A 7-Tesla high density transmit with 28-channel receive-only array knee coil*. in *Proceedings of the International Society for Magnetic Resonance in Medicine... Scientific Meeting and Exhibition. International Society for Magnetic Resonance in Medicine. Scientific Meeting and Exhibition*. 2010. NIH Public Access.

46. Hand, J., *Modelling the interaction of electromagnetic fields (10 MHz–10 GHz) with the human body: methods and applications.* Physics in medicine and biology, 2008. **53**(16): p. R243.

47. Hue, Y.-K., et al., *A Complete Modeling System with Experimental Validation for Calculating the Transmit and Receive Fields, Total Power Deposition, Input Impedance, and Coupling between Coil Elements.* ISMRM, 2008: p. 0438.

48. Ibrahim, T., et al., *Analysis of B1 field profiles and SAR values for multi-strut transverse electromagnetic RF coils in high field MRI applications.* Physics in medicine and biology, 2001. **46**(10): p. 2545.

49. Ibrahim, T.S., Y.-K. Hue, and L. Tang, *Understanding and manipulating the RF fields at high field MRI.* NMR in Biomedicine, 2009. **22**(9): p. 927-936.

50. Ibrahim, T.S., et al., *In-depth study of the electromagnetics of ultrahigh-field MRI.* NMR in Biomedicine, 2007. **20**(1): p. 58-68.

51. Ibrahim, T.S. and L. Tang, *Insight into RF power requirements and B1 field homogeneity for human MRI via rigorous FDTD approach.* Journal of magnetic resonance imaging, 2007. **25**(6): p. 1235-1247.

52. Kim, J., et al., *Experimental and numerical analysis of b 1+ field and SAR with a new transmit array design for 7t breast MRI.* Journal of Magnetic Resonance, 2016. **269**: p. 55-64.

53. McDougall, M.P., et al., *Quadrature transmit coil for breast imaging at 7 tesla using forced current excitation for improved homogeneity.* Journal of Magnetic Resonance Imaging, 2014. **40**(5): p. 1165-1173.

54. Trattnig, S., et al., *Advanced MR methods at ultra-high field (7 Tesla) for clinical musculoskeletal applications.* Eur Radiol, 2012. **22**(11): p. 2338-46.

55. van de Bank, B.L., et al., *Ultra high spatial and temporal resolution breast imaging at 7T.* NMR in Biomedicine, 2013. **26**(4): p. 367-375.

56. Van de Moortele, P.-F., et al., *T1 weighted brain images at 7 Tesla unbiased for Proton Density, T2 contrast and RF coil receive B1 sensitivity with simultaneous vessel visualization.* NeuroImage, 2009. **46**(2): p. 432-446.

57. van den Bergen, B., et al., *7 T body MRI: B1 shimming with simultaneous SAR reduction.* Physics in medicine and biology, 2007. **52**(17): p. 5429.

58. Van der Velden, T.A., et al., *Radiofrequency configuration to facilitate bilateral breast 31P MR spectroscopic imaging and high-resolution MRI at 7 Tesla.* Magnetic resonance in medicine, 2015. **74**(6): p. 1803-1810.

59. Vaughan, T., M. Garwood, and K. Ugurbil. *Volume coils for highest field MRI*. in *Antennas and Propagation Society International Symposium, 2001. IEEE*. 2001. IEEE.

60. Wright, A.C., et al., *Helmholtz-pair transmit coil with integrated receive array for high-resolution MRI of trabecular bone in the distal tibia at 7T.* J Magn Reson, 2011. **210**(1): p. 113-22.

61. Y. Zhao, N.K., S. Wood, T. Zhao, S. B. Raval, and T. S. Ibrahim. *3D Eigenmodes Optimizations for 3D Imaging at 7T*. in *The 23nd International Society of Magnetic Resonance in Medicine Annual Meeting*. 2015. Toronto, Canada.

62. Yujuan Zhao , T.Z., Shailesh B. Raval , Narayanan Krishnamurthy , Hai Zheng ,Chad T. Harris , William B. Handler , Blaine A. Chronik , and Tamer S. Ibrahim *Dual Optimization Method of RF and Quasi-Static Field Simulations for Reduction of Eddy Currents Generated on 7T RF Coil Shielding.* MRM, 2014: p. DOI: 10.1002/mrm.25424.

63. TS, I., et al. *20-To-8 Channel Tx Array with 32-Channel Adjustable Receive-Only Insert for 7T Head Imaging.* in *International Society of Magnetic Resonance in Medicine*. 2013. Salt Lake City, Utah.

64. Van de Moortele, P.-F., et al., *T 1 weighted brain images at 7 Tesla unbiased for Proton Density, T 2 contrast and RF coil receive B 1 sensitivity with simultaneous vessel visualization.* Neuroimage, 2009. **46**(2): p. 432-446.

65. Zhao, Y., et al., *Dual optimization method of radiofrequency and quasistatic field simulations for reduction of eddy currents generated on 7T radiofrequency coil shielding.* Magnetic Resonance in Medicine, 2014.

66. Dimbylow, P., *FDTD calculations of the whole-body averaged SAR in an anatomically realistic voxel model of the human body from 1 MHz to 1 GHz.* Physics in medicine and biology, 1997. **42**(3): p. 479.

67. Raval S, S.T., Wood S, Krishnamurthy N, Ibrahim TS. *In-vivo (8x4) 32-ch Tx-only Body Array for UHF MR*. in *In Proc. of the 25th International Society of Magnetic Resonance in Medicine Annual Meeting*. 2017. Honolulu, Hawaii, USA.

68. Wang, H., et al., *An MRI-dedicated parallel FDTD scheme.* Concepts in Magnetic Resonance Part B: Magnetic Resonance Engineering, 2007. **31**(3): p. 147-161.

69. Zhu, Y., *Parallel excitation with an array of transmit coils.* Magnetic Resonance in Medicine, 2004. **51**(4): p. 775-784.

70. Katscher, U. and P. Börnert, *Parallel RF transmission in MRI.* NMR in Biomedicine, 2006. **19**(3): p. 393-400.

71. Kim, J., et al., *B1+, SAR, and Temperature Distributions in the Breast with Different Tissue Ratio: FDTD Simulations and Experimental RF Field and Temperature Measurements at 7T.* International Society of Magnetic Resonance in Medicine, 2015: p. #1799.

72. Taflove A, H.S., *Computational Electrodynamics: The Finite-Difference Time-Domain Method.* 2005.

73. Krishnamurthy, N., T. Zhao, and T.S. Ibrahim, *Effects of receive-only inserts on specific absorption rate, B1+ field, and Tx coil performance.* Journal of Magnetic Resonance Imaging, 2014. **39**(2): p. 475-484.

74. Mao, W., M.B. Smith, and C.M. Collins, *Exploring the limits of RF shimming for high-field MRI of the human head.* Magnetic resonance in medicine, 2006. **56**(4): p. 918-922.

75. Y, Z., et al. *Simultaneous Excitation of Distinct Electromagnetic Modes Using a Tx Array.* in *ISMRM*. 2013. Salt Lake City, US.

76. Collins, C.M. and M.B. Smith, *Spatial resolution of numerical models of man and calculated specific absorption rate using the FDTD method: a study at 64 MHz in a magnetic resonance imaging coil.* Journal of Magnetic Resonance Imaging, 2003. **18**(3): p. 383-388.

77. Ibrahim, T.S., et al. *Tic Tac Toe: Highly-Coupled, Load Insensitive Tx/Rx Array and a Quadrature Coil Without Lumped Capacitors*. in *Intl. Soc. Mag. Reson. Med.* 2008.

78. Jin, J., *Electromagnetic analysis and design in magnetic resonance imaging*. Vol. 1. 1998: CRC press.

79. Vaughan, J.T. and J.R. Griffiths, *RF coils for MRI*. 2012: John Wiley & Sons.

80. Barberi, E.A., et al., *A transmit-only/receive-only (TORO) RF system for high-field MRI/MRS applications.* Magnetic resonance in medicine, 2000. **43**(2): p. 284-289.

81. Ibrahim, T.S., et al., *Effect of RF coil excitation on field inhomogeneity at ultra high fields: a field optimized TEM resonator.* Magnetic resonance imaging, 2001. **19**(10): p. 1339-1347.

82. Zhu, Y., et al., *Highly parallel volumetric imaging with a 32-element RF coil array.* Magnetic Resonance in Medicine, 2004. **52**(4): p. 869-877.

83. Adriany, G., et al., *A geometrically adjustable 16-channel transmit/receive transmission line array for improved RF efficiency and parallel imaging performance at 7 Tesla.* Magnetic resonance in medicine, 2008. **59**(3): p. 590-597.

84. Klomp, D., et al. *High resolution MR imaging and spectroscopy of the human breast at 7T using a focused field RF coil setup*. in *Proc. Intl. Soc. Mag. Reson. Med*. 2010.

85. Kraff, O., et al., *An eight-channel phased array RF coil for spine MR imaging at 7 T.* Investigative radiology, 2009. **44**(11): p. 734-740.

86. Zhang, X., K. Ugurbil, and W. Chen, *Microstrip RF surface coil design for extremely high-field MRI and spectroscopy.* Magnetic resonance in medicine, 2001. **46**(3): p. 443-450.

87. Dieringer, M.A., et al., *Design and application of a four-channel transmit/receive surface coil for functional cardiac imaging at 7T.* Journal of Magnetic Resonance Imaging, 2011. **33**(3): p. 736-741.

88. Raaijmakers, A., et al., *Design of a radiative surface coil array element at 7 T: the single-side adapted dipole antenna.* Magnetic resonance in medicine, 2011. **66**(5): p. 1488-1497.

89. Vaughan, J., et al., *Detunable transverse electromagnetic (TEM) volume coil for high-field NMR.* Magnetic Resonance in Medicine, 2002. **47**(5): p. 990-1000.

90. Wiggins, G., et al., *Eight-channel phased array coil and detunable TEM volume coil for 7 T brain imaging.* Magnetic resonance in medicine, 2005. **54**(1): p. 235-240.

91. Wang, C. and G.X. Shen, *B1 field, SAR, and SNR comparisons for birdcage, TEM, and microstrip coils at 7T.* Journal of magnetic resonance imaging, 2006. **24**(2): p. 439-443.

92. Wright, S.M. and L.L. Wald, *Theory and application of array coils in MR spectroscopy*. NMR in Biomedicine, 1997. **10**(8): p. 394-410.

93. Setsompop, K., et al., *Magnitude least squares optimization for parallel radio frequency excitation design demonstrated at 7 Tesla with eight channels.* Magnetic resonance in medicine, 2008. **59**(4): p. 908-915.

94. Vaughan, J.T., et al., *High frequency volume coils for clinical NMR imaging and spectroscopy.* Magnetic Resonance in Medicine, 1994. **32**(2): p. 206-218.

95. Yang, Q.X., et al., *Analysis of wave behavior in lossy dielectric samples at high field.* Magnetic resonance in medicine, 2002. **47**(5): p. 982-989.

96. Vaughan, J., et al. *A patient friendly head coil for high field MRI*. in *Proceedings of the 11th annual meeting of the ISMRM*. 2003.

97. Setsompop, K., et al., *Slice-selective RF pulses for in vivo B 1+ inhomogeneity mitigation at 7 tesla using parallel RF excitation with a 16-element coil.* Magnetic resonance in medicine, 2008. **60**(6): p. 1422-1432.

98. Setsompop, K., et al., *High-flip-angle slice-selective parallel RF transmission with 8 channels at 7 T.* Journal of magnetic resonance, 2008. **195**(1): p. 76-84.

99. Zelinski, A.C., et al., *Specific absorption rate studies of the parallel transmission of inner-volume excitations at 7T.* Journal of magnetic resonance imaging, 2008. **28**(4): p. 1005-1018.

100. Zhao, W., et al., *Nineteen-channel receive array and four-channel transmit array coil for cervical spinal cord imaging at 7T.* Magnetic resonance in medicine, 2014. **72**(1): p. 291-300.

101. Alecci, M., et al., *Radio frequency magnetic field mapping of a 3 Tesla birdcage coil: experimental and theoretical dependence on sample properties.* Magnetic Resonance in Medicine, 2001. **46**(2): p. 379-385.

102. Angelone, L.M., et al., *Analysis of the role of lead resistivity in specific absorption rate for deep brain stimulator leads at 3T MRI.* IEEE transactions on medical imaging, 2010. **29**(4): p. 1029-1038.

103. Matson, G.B., P. Vermathen, and T.C. Hill, *A practical double-tuned 1H/31P quadrature birdcage headcoil optimized for 31P operation.* Magnetic resonance in medicine, 1999. **42**(1): p. 173-182.

104. Ordidge, R.J., et al., *Assessment of relative brain iron concentrations using T2-weighted and T2*-weighted MRI at 3 Tesla.* Magnetic resonance in medicine, 1994. **32**(3): p. 335-341.

105. Tian, J., et al. *Searching for the optimal body coil design for 3T MRI*. in *Proceedings of the 21st Annual Meeting, International Society for Magnetic Resonance in Medicine, Salt Lake City, Utah, USA*. 2013.

106. Kim, J., et al., *Development of a 7 T RF coil system for breast imaging.* NMR in Biomedicine, 2017. **30**(1).

107. Han, M., et al., *Depiction of achilles tendon microstructure in vivo using high-resolution 3-dimensional ultrashort echo-time magnetic resonance imaging at 7 T.* Invest Radiol, 2014. **49**(5): p. 339-45.

108. Zheng, T., et al. *A 7-Tesla high density Tx/Rx mammography coil*. in *Proc Intl Soc Mag Reson Med*. 2011.

109. Orzada, S., et al. *16-channel Tx/Rx body coil for RF shimming with selected Cp modes at 7T*. in *Proceedings of the 18th Annual Meeting of ISMRM*. 2010.

110. Metzger, G.J., et al., *Local B1+ shimming for prostate imaging with transceiver arrays at 7T based on subject-dependent transmit phase measurements.* Magnetic resonance in medicine, 2008. **59**(2): p. 396-409.

111. Zhao, Y., et al., *Dual optimization method of radiofrequency and quasistatic field simulations for reduction of eddy currents generated on 7T radiofrequency coil shielding.* Magnetic Resonance in Medicine, 2015. **74**(5): p. 1461-1469.

112. Wang, Z., et al., *SAR and temperature: simulations and comparison to regulatory limits for MRI.* Journal of Magnetic Resonance Imaging, 2007. **26**(2): p. 437-441.

113. Zastrow, E., et al., *Database of 3D grid-based numerical breast phantoms for use in computational electromagnetics simulations.* Department of Electrical and Computer Engineering University of Wisconsin-Madison, 2008.

114. Yee, K.S., J.S. Chen, and A.H. Chang, *Conformal finite-different time-domain (FDTD) with overlapping grids.* IEEE Transactions on Antennas and Propagation, 1992. **40**(9): p. 1068-1075.

115. Chen, Y., R. Mittra, and P. Harms, *Finite-difference time-domain algorithm for solving Maxwell's equations in rotationally symmetric geometries.* IEEE Transactions on Microwave Theory and Techniques, 1996. **44**(6): p. 832-839.

116. Liu, F., et al., *Numerical modeling of 11.1 T MRI of a human head using a MoM/FDTD method.* Concepts in Magnetic Resonance Part B: Magnetic Resonance Engineering, 2005. **24**(1): p. 28-38.

117. Zhao, H., S. Crozier, and F. Liu, *Finite difference time domain (FDTD) method for modeling the effect of switched gradients on the human body in MRI.* Magnetic resonance in medicine, 2002. **48**(6): p. 1037-1042.

118. Bazzocchi, M., et al., *Contrast-enhanced breast MRI in patients with suspicious microcalcifications on mammography: results of a multicenter trial.* American Journal of Roentgenology, 2006. **186**(6): p. 1723-1732.

119. Kriege, M., et al., *Efficacy of MRI and mammography for breast-cancer screening in women with a familial or genetic predisposition.* New England Journal of Medicine, 2004. **351**(5): p. 427-437.

120. Saslow, D., et al., *American Cancer Society guidelines for breast screening with MRI as an adjunct to mammography.* CA: a cancer journal for clinicians, 2007. **57**(2): p. 75-89.

121. Kuhl, C.K., et al., *Dynamic breast mr imaging: Are signal intensity time course data useful for differential diagnosis of enhancing lesions? 1.* Radiology, 1999. **211**(1): p. 101-110.

122. Kuhl, C.K. and H.H. Schild, *Dynamic image interpretation of MRI of the breast.* Journal of Magnetic Resonance Imaging, 2000. **12**(6): p. 965-974.

123. Kinkel, K. and N.M. Hylton, *Challenges to interpretation of breast MRI.* Journal of Magnetic Resonance Imaging, 2001. **13**(6): p. 821-829.

124. Morris, E.A., et al., *MRI of occult breast carcinoma in a high-risk population.* American Journal of Roentgenology, 2003. **181**(3): p. 619-626.

125. Radiology, A.C.o. and B.-R. Committee, *ACR BI-RADS breast imaging and reporting data system: breast imaging atlas*. 2003: American College of Radiology.

126. Kinoshita, T., et al., *Fat necrosis of breast: a potential pitfall in breast MRI.* Clinical imaging, 2002. **26**(4): p. 250-253.

127. Pinker, K., et al., *Clinical application of bilateral high temporal and spatial resolution dynamic contrast-enhanced magnetic resonance imaging of the breast at 7 T.* Eur Radiol, 2014. **24**(4): p. 913-20.

128. Yusuf, E., et al., *Do knee abnormalities visualised on MRI explain knee pain in knee osteoarthritis? A systematic review.* Annals of the rheumatic diseases, 2011. **70**(1): p. 60-67.

129. Lindsey, C., et al., *Magnetic resonance evaluation of the interrelationship between articular cartilage and trabecular bone of the osteoarthritic knee.* Osteoarthritis and cartilage, 2004. **12**(2): p. 86-96.

130. Theysohn, J.M., et al., *MRI of the ankle joint in healthy non-athletes and in marathon runners: image quality issues at 7.0 T compared to 1.5 T.* Skeletal Radiol, 2013. **42**(2): p. 261-7.

131. Peterfy, C., E. Schneider, and M. Nevitt, *The osteoarthritis initiative: report on the design rationale for the magnetic resonance imaging protocol for the knee.* Osteoarthritis and cartilage, 2008. **16**(12): p. 1433-1441.

132. Kogan, F., A.P. Fan, and G.E. Gold, *Potential of PET-MRI for imaging of non-oncologic musculoskeletal disease.* Quant Imaging Med Surg, 2016. **6**(6): p. 756-771.

133. Oei, L., et al., *Quantitative imaging methods in osteoporosis.* Quant Imaging Med Surg, 2016. **6**(6): p. 680-698.

134. Bangerter, N.K., et al., *Quantitative sodium magnetic resonance imaging of cartilage, muscle, and tendon.* Quant Imaging Med Surg, 2016. **6**(6): p. 699-714.

135. Azlan, C.A., et al., *B1 transmission-field inhomogeneity and enhancement ratio errors in dynamic contrast-enhanced MRI (DCE-MRI) of the breast at 3T.* Journal of Magnetic Resonance Imaging, 2010. **31**(1): p. 234-239.

136. Diehl, D., et al. *B1 Homogenization at 3 T MRI using a 16 rung transmit array*. in *Proceedings of the 13th Annual Meeting of ISMRM, Miami Beach, FL, USA*. 2005.

137. Harvey, J.A., et al., *Breast MR imaging artifacts: how to recognize and fix them.* Radiographics, 2007. **27**(suppl_1): p. S131-S145.

138. Kuhl, C.K., et al., *Effect of B1 inhomogeneity on breast MR imaging at 3.0 T.* Radiology, 2007. **244**(3): p. 929-930.

139. Cui, J., et al., *A Switched-Mode Breast Coil for 7 T MRI Using Forced-Current Excitation.* IEEE Transactions on Biomedical Engineering, 2015. **62**(7): p. 1777-1783.

140. Chen, J., Z. Feng, and J.-M. Jin, *Numerical simulation of SAR and B/sub 1/-field inhomogeneity of shielded RF coils loaded with the human head.* IEEE transactions on biomedical engineering, 1998. **45**(5): p. 650-659.

141. Oh, S., et al., *Experimental and numerical assessment of MRI-induced temperature change and SAR distributions in phantoms and in vivo.* Magnetic resonance in medicine, 2010. **63**(1): p. 218-223.

142. Zhao, Y., et al. *3D eigenmodes optimizations for 3D imaging at 7T*. in *The 23nd International Society of Magnetic Resonance in Medicine Annual Meeting*. 2015.

143. Zhao, Y. and T. Ibrahim. *On the E-Field Construction/Deconstruction and B1+ Efficiency/Homogeneity with Transmit Array Eigen Modes*. in *The 22nd International Society of Magnetic Resonance in Medicine Annual Meeting*. 2014.

144. Cui, J., et al., *A switched-mode breast coil for 7 tesla MRI using forced-current excitation.* 2014.

145. Korteweg, M.A., et al., *Feasibility of 7 Tesla breast magnetic resonance imaging determination of intrinsic sensitivity and high-resolution magnetic resonance imaging, diffusion-weighted imaging, and 1H-magnetic resonance spectroscopy of breast cancer patients receiving neoadjuvant therapy.* Investigative radiology, 2011. **46**(6): p. 370-376.

146. Stehouwer, B., et al., *101 Feasibility of Contrast-enhanced and High-resolution 7 Tesla MRI in Patients with Suspicious Breast Lesions.* European Journal of Cancer, 2012. **48**: p. S70.

147. Avdievich, N.I., V.N. Krymov, and H.P. Hetherington, *Modified perturbation method for transverse electromagnetic (TEM) coil tuning and evaluation.* Magnetic resonance in medicine, 2003. **50**(1): p. 13-18.

148. Roschmann, P.K., *High-frequency coil system for a magnetic resonance imaging apparatus*. 1988, Google Patents.

149. Harpen, M.D., *Radiative losses of a birdcage resonator.* Magnetic resonance in medicine, 1993. **29**(5): p. 713-716.

150. Berenger, J.-P., *Three-dimensional perfectly matched layer for the absorption of electromagnetic waves.* Journal of computational physics, 1996. **127**(2): p. 363-379.

151. Christ, A., et al., *The Virtual Family—development of surface-based anatomical models of two adults and two children for dosimetric simulations.* Physics in medicine and biology, 2009. **55**(2): p. N23.

152. Fautz, H. *Extending the sensitivity range for transmit array B1 mapping using relative B1 maps*. in *Proc Intl Soc Mag Reson Med*. 2012.

153. Kuhl, C., *The Current Status of Breast MR Imaging Part I. Choice of Technique, Image Interpretation, Diagnostic Accuracy, and Transfer to Clinical Practice 1.* Radiology, 2007. **244**(2): p. 356-378.

154. Umutlu, L., et al., *Dynamic contrast-enhanced breast MRI at 7 Tesla utilizing a single-loop coil: a feasibility trial.* Acad Radiol, 2010. **17**(8): p. 1050-6.

155. van der Velden, T.A., et al., *Radiofrequency configuration to facilitate bilateral breast (31) P MR spectroscopic imaging and high-resolution MRI at 7 Tesla.* Magn Reson Med, 2015. **74**(6): p. 1803-10.

156. Wiggins, G., et al., *32-channel 3 tesla receive-only phased-array head coil with soccer-ball element geometry.* Magnetic resonance in medicine, 2006. **56**(1): p. 216-223.

157. Zheng, T., et al., *Phased array knee coil*. 2006, Google Patents.

158. Goto, H., et al., *A preliminary study of the T1rho values of normal knee cartilage using 3T-MRI.* European journal of radiology, 2012. **81**(7): p. e796-e803.

159. Wang, L., et al., *T1rho MRI of menisci and cartilage in patients with osteoarthritis at 3T.* European journal of radiology, 2012. **81**(9): p. 2329-2336.

160. Liebl, H., et al., *In vitro assessment of knee MRI in the presence of metal implants comparing MAVRIC-SL and conventional fast spin echo sequences at 1.5 and 3 T field strength.* Journal of Magnetic Resonance Imaging, 2015. **41**(5): p. 1291-1299.

161. Cotofana, S., et al., *In vivo measures of cartilage deformation: patterns in healthy and osteoarthritic female knees using 3T MR imaging.* European radiology, 2011. **21**(6): p. 1127-1135.

162. Smith, H.E., et al., *Spatial variation in cartilage T2 of the knee.* Journal of Magnetic Resonance Imaging, 2001. **14**(1): p. 50-55.

163. Solis, S., et al., *Transceiver 4-leg birdcage for high field MRI: knee imaging.* Revista mexicana de física, 2008. **54**(3): p. 215-220.

164. Peterson, D.M., et al., *Application of a birdcage coil at 3 Tesla to imaging of the human knee using MRI.* Magnetic resonance in medicine, 1999. **42**(2): p. 215-221.

165. Li, X., et al., *In vivo T 1ρ and T 2 mapping of articular cartilage in osteoarthritis of the knee using 3T MRI.* Osteoarthritis and cartilage, 2007. **15**(7): p. 789-797.

166. Avdievich, N.I., et al., *4T split TEM volume head and knee coils for improved sensitivity and patient accessibility.* Journal of magnetic resonance, 2007. **187**(2): p. 234-241.

167. Commission, I.E., *International standard, medical equipment-part 2: particular requirements for the safety of magnetic resonance equipment for medical diagnosis.* International Electrotechnical Commission, 2002. **2nd revision**(6012-33): p. 29-31.

168. Food and D. Administration, *Guidance for the submission of premarket notifications for magnetic resonance diagnostic devices.* US Food and Drug Administration, 1998.

169. Bright, A., *Planning and Positioning in MRI*. 2011: Elsevier Australia.

170. Kim, J., et al., *Experimental and numerical analysis of B1+ field and SAR with a new transmit array design for 7T breast MRI.* J Magn Reson, 2016. **269**: p. 55-64.

171. Krishnamurthy, N., T. Zhao, and T.S. Ibrahim, *Effects of receive-only inserts on specific absorption rate, B1 (+) field, and Tx coil performance.* J Magn Reson Imaging, 2014. **39**(2): p. 475-84.